

Vegetation dynamics in Ecuador

kumulative Dissertation
zur Erlangung der Doktorgrades
der Naturwissenschaften
(Dr. rer. nat.)

dem Fachbereich Geographie
der Philipps-Universität Marburg
vorgelegt von

Víctor Hugo González Jaramillo
aus Loja / Ecuador

Marburg / Lahn 2019

Vom Fachbereich Geographie
der Philipps-Universität Marburg als Dissertation
am 14.01.2020 angenommen

Erstgutachter: Prof. Dr. Jörg Bendix
Zweitgutachter: Prof. Dr. Maaïke Bader

Tag der mündlichen Prüfung: 22.01.2020

Preface:

After some years of study, effort and sacrifice, I have completed the present work, which without the help of some people it would not have been possible, so I want to thank all those who were part of this learning process.

To the authorities of Universidad Técnica Particular de Loja (UTPL), who gave me the opportunity to do my doctoral studies, specially to Dr. Juan Pablo Suarez Chacón, Vice Chancellor of Research at UTPL, thanks for all their support.

In addition, many thanks to my supervisor, Professor Dr. Jörg Bendix, who helped me in all instances of the investigation with his knowledge, experience, advice, and words of encouragement.

My immense gratitude to my co-supervisor, Professor Dr. Andreas Fries, a colleague and a friend, without his help, support and guidance this research would never have had great and fruitful results.

Special thanks to Dr. Rütger Rollenbeck, who guided this work in the initial years. Also thanks to my friends of Marburg University, Astrid Bendix, Sonja Haese, Birgit Kühne and Maik Dobbermann and I am so sorry if I forget someone, but right now it's hard for me to remember everyone. Also thanks to Gregory Gedeon for text revision. For all their help and support in these scientist process, all my thankfulness.

Thanks to my family, to my parents Maruja and Ruperto that always support me in all instances of my life and give me all their love. A special thanks to my wife Jhoana, who along with our children Víctor Emilio, Joaquin Alejandro, Ignacio Benjamin and Felipe Nicolas, always give me everything a man needs to be happy, while they wait in silence (although not always) and give me all their love and strength to finish this work, which is now not only mine, but also it is an achievement of my beautiful and dear family.

Finally, I can say that the way is hard but with effort and perseverance all is possible, because always a sparkle of light can show you the red line in the research way. But this way never ends for a man, because the life is short but the knowledge is huge as a river that never ends to flows to the eternity.

Víctor Hugo González Jaramillo
Loja, October 2019

For
My Family, My Wife and My Children

Contents

List of Figures	VII
List of Tables	X
List of Acronyms	XI
List of Symbols	XIV
1 Introduction	1
1.1 Motivation.....	4
1.2 Aims and outlines.....	5
1.3 Approach.....	7
1.4 References.....	10
2 Assessment of deforestation during the last decades in Ecuador using NOAA-AVHRR satellite data	17
2.1 Introduction.....	19
2.2 Study area and data.....	22
2.3 Methods.....	26
2.4 Results and discussion.....	32
2.5 Conclusions.....	38
2.6 References.....	41
2.7 Supplement 2 A.....	49
3 Estimation of Above Ground Biomass in a Tropical Mountain Forest in southern Ecuador using airborne LiDAR data	50
3.1 Introduction.....	53
3.2 Materials and Methods.....	57
3.2.1 Study Area.....	57
3.2.2 LiDAR Data and Field Measurements.....	59
3.2.3 Methods.....	60
3.3 Results.....	66
3.4 Discussion.....	75
3.5 Conclusions.....	80
3.6 References.....	82

4 AGB estimation in a Tropical Mountain Forest (TMF) by means of RGB and multispectral images using an Unmanned Aerial Vehicle (UAV)	95
4.1 Introduction	97
4.2 Materials and Methods	99
4.2.1 Study Area	99
4.2.2 Equipment	100
4.2.2.1 DJI Inspire	100
4.2.2.2 Parrot Sequoia	101
4.3 Methodology	102
4.3.1 Flight planning and data acquisition	102
4.3.2 Data processing	103
4.3.2.1 AGB estimation by means of RGB data – use of photogrammetry	104
4.3.2.2 AGB estimation using multispectral data	107
4.3.3 Validation of the RGB and multispectral AGB estimations	109
4.4 Results	110
4.4.1 AGB results by means of RGB data	110
4.4.2 AGB results by means of multispectral data	112
4.4.3 Validation	114
4.5 Discussion	118
4.6 Conclusions	120
4.7 References	122
 5 Summary, Conclusions and Outlook	 131
5.1 Summary and Conclusions	131
5.2 Outlook	135
5.3 References	136
 Abstract	 142
Zusammenfassung	143

List of Figures

1-1 Processing chain for forest monitoring at different spatial scales using remote sensing data: (A) corresponds to forest classification and deforestation rate calculation at country level, (B) to AGB estimation in complex TMF terrain at catchment level, and (C) to continuous forest monitoring of most vulnerable parts using an UAV	8
2-1 Digital Elevation Model (DEM; adapted from Farr et al., 2007) of the research area (continental Ecuador), including the tree principal regions: Coastal Lowland, Andean Highland and Amazon Basin, as well as the reference sites for validation	23
2-2 Processing scheme of the “forest” – “non-forest” classification	26
2-3 a) Annual cloud cover map of Ecuador (modified from Bendix et al., 2004); b) Example of a cloud classification map	28
2-4 MVC composite of annual NDVI (year 2001) with remaining clouds	29
2-5 Decision tree algorithm of the “forest” – “non-forest” classification.....	30
2-6 Forest classification of the year a) 1986 (with reference site), b) 2001 (with reference site) and c) 2008.....	34
2-7 Forest classification at Papallacta for 1986 a) Reference site (adapted from Bendix and Rafiqpoor 2001), b) Classified NOAA-AVHRR image.....	37
2-8 Forest Classification at ECSF for 2001 a) Reference site (adapted from Göttlicher et al. 2009), b) Classified NOAA-AVHRR image.....	37
2-A Regional forest cover of the years 1986, 2001 and 2008.....	49

3-1	Digital Elevation Model (DEM) of the study area, the San Francisco catchment, including the field plot distribution.	58
3-2	Principal vegetation units in the San Francisco catchment: (a) Tropical Mountain Forest (TMF), (b) Elfin Forest, (c) subpáramo and (d) pasture	59
3-3	Processing chain to calculate above ground biomass (AGB) and C stock based on LiDAR point cloud data (WD = Wood Density, H = Tree Height, DBH = Diameter at Breast Height, DTM = Digital Terrain Model, DSM = Digital Surface Model, CHM = Canopy Height Model, TPI= Topographic Position Index and MPI= Morphometric Protection Index).....	61
3-4	Relationship between DBH (cm) and H (m) of the field measurements	63
3-5	(a) Canopy Height Model (CHM), including field plots; (b) Example of the individual tree classification for one plot in the study area.....	66
3-6	(a) Measured H compared to estimated H, derived from the LiDAR data; (b) Measured DBH compared to estimated DBH, obtained from the local height-diameter relationship.....	67
3-7	Forest structure detected in the research catchment by means of (a) TPI; (b) MPI; (c) distribution of trees with a DBH smaller than 20 cm (red) and bigger than 20 cm (green).....	69
3-8	Calculated AGB by means of the individual tree measurements compared to estimated AGB	69
3-9	Portion of trees in the established H (above) and DBH (below) classes, divided in ravine forest: (a and c), and ridge forest (b and d).....	71
3-10	Portion of total AGB of the established H classes; (a) ravine forest, (b) ridge forest.....	72
3-11	Land cover map in the San Francisco catchment obtained from the CHM (resolution 1 ha × 1 ha).....	73
3-12	Spatial distribution of AGB in the Rio San Francisco catchment.....	74

4-1	(a) Digital elevation model (DEM) of Ecuador, and (b) DEM of the San Francisco catchment including the study area.....	100
4-2	Unmanned aerial vehicle (UAV) DJI Inspire 1, equipped with the RGB camera ZENMUSE X3 and the multi-spectral camera Parrot Sequoia.....	101
4-3	Drone-based orthophoto of the selected study area, including the starting point, ground control points (GCP), and validation transects (yellow) inside the core area (rectangle).....	103
4-4	Processing chain to estimate above-ground biomass AGB (Mg ha ⁻¹) using RGB (left) and multispectral imagery (right).....	104
4-5	Data processing of the 132 RGB images in Pix4D (SfM), where dots in blue and green represent the individual photos and their overlap. GCPs are shown below.....	105
4-6	(a) Individual AGB values of the dominant trees detected in the core area; (b) Spatial distribution of AGB obtained from the RGB data.....	111
4-7	Multispectral data obtained by the multispectral camera, (a) nonsupervised classification based on the false color composition image and (b) NDVI values.....	113
4-8	AGB estimation by means of multispectral data.....	113
4-9	Transect profiles, comparing RGB and light detection and ranging (LiDAR) models: (a) Vegetated areas, (b) less vegetated areas.....	115
4-10	Regression analysis between RGB and LiDAR data: (a) H correlation, (b) AGB correlation.....	116

List of Tables

2-1 Results of the comparison between reference sites and the new classification approach. The mean values show the percentage of forest present in class of forest/nonforest.....	36
2-2 Accuracy between “forest” and “non-forest” pixel of the reference sites (rows); a) Papallacta 1986; b) ECSF 2001) and the generated forest cover maps (columns).....	38
3-1 Leica Geosystems ALS-50 II CM specifications	60
3-2 Mean and extreme values of H, DBH and AGB for individual trees in the TMF and the Elfin Forest.1 Introduction	70
3-3 AGB and C stock in the San Francisco catchment.....	73
3-4 Portion of the individual vegetation units respective to the total catchment area, including total AGB and C stock.....	75
4-1 AGB validation comparing RGB models with the LiDAR models.....	116
4-2 Calculated H, DBH, and AGB values (RGB above and LiDAR below).	116
4-3 Calculated AGB from multispectral and LiDAR data1.1 Motivation.....	117

List of Acronyms

AGB	Above Ground Biomass
asl	Above Sea Level
AELDS	Advanced Earth Location Data Systems
ASTER	Advanced Spaceborne Thermal Emission and Reflection Radiometer
AVHRR	Advanced Very High Resolution Radiometer
ALS	Airborne Laser Scanning
CHM	Canopy Height Model
C	Carbon
CO₂	Carbon Dioxide
cm	Centimeter
CLIRESEN	Centro de Levantamientos Integrados de Recursos Naturales por Sensores Remotos
R²	Coefficient of Determination
(x, y, z)	Coordinate X, Coordinate Y, Altitude
CLASS	Comprehensive Large Array-data Stewardship System
°	Degrees
°C	Degrees Celsius
DBH	Diameter at breast height
DEM	Digital Elevation Model
DTM	Digital Terrain Model
DSM	Digital Surface Model
ENSO	El Niño - Southern Oscillation
ECSF	Estación Científica San Francisco
FAO	Food and Agriculture Organization
GOES	Geostationary Operational Environmental Satellite
DFG	German Research Foundation
fig.	Figure
GB	Gigabyte
GNSS	Global Navigation Satellite System
GPS	Global Positioning System
g	Gram

gr cm⁻³	Gram per Cubic Centimeter
GHG	Green House Gas
GCP	Ground Control Point
GSD	Ground Sample Distance
ha	Hectare
H	Height
Hz	Hertz
INAMHI	Instituto Nacional de Meteorología en Hidrología
IPCC	Intergovernmental Panel on Climate Change
kHz	Kilohertz
km	Kilometer
LANDSAT	Land Satellite
LiDAR	Light Detection and Ranging
LAC	Local Area Coverage
LMF	Lowland Mountain Forest
MVC	Maximum Value Composite
Mg	Megagram
Mg ha⁻¹	Megagram per Hectare
CH₄	Methane
m	Meter
m s⁻¹	Meter per Second
μm	Micrometer
mm	Millimeter
MAE	Ministerio del Ambiente de la Repúblicas del Ecuador
MODIS	Moderate Resolution Imaging Spectroradiometer
MPI	Morphometric Protection Index
Mt.	Mount
MrSID	Multiresolution Seamless Image Database
nm	Nanometer
NASA	National Aeronautics and Space Administration
NOAA	National Oceanic and Atmospheric Administration
NIR	Near-infrared
NDVI	Normalized Difference Vegetation Index
O₂	Oxygen

PCA	Principal Component Analysis
RGB	Red Green and Blue Color Value
REDD+	Reducing Emissions from Deforestation and Forest Degradation
RBSF	Reserva Biológica San Francisco
RMSE	Root Mean Square Error
S	South
SRTM	Shuttle Radar Topography Mission
km²	Square Kilometer
m²	Square Meter
SfM	Structure from Motion
tab.	Table
TM	Thematic Mapper
TIR	Thermal Infrared
3D	Three-dimensional
TPI	Topographic Position Index
TERRA	Total Earth Remediation and Restoration Activity
TMF	Tropical Mountain Forest
UAV	Unmanned Aerial Vehicle
UTPL	Universidad Técnica Particular de Loja
UMF	Upper Mountain Forest
VIS	Visible
W	West
WD	Wood density

List of Symbols

Symbol	Meaning	Unit
q	Annual rate of change	[%/ 100]
AGB	Above Ground Biomass	[Mg ha ⁻¹]
AGBtree	Above Groud Biomass per tree	[Mg]
D	Diameter at breast height	[cm]
H	Height	[m]
WD	Wood Density	[gr cm ⁻³]
C stocks	Carbon stocks	[Mg C ha ⁻¹]

1 Introduction

Natural forests cover about 31% of the Earth's surface (Kou et al., 2017) and play an important role in the carbon (C) cycle, including the regulation of anthropogenic greenhouse gas (GHG) emissions. These ecosystems absorb and store large amounts of atmospheric C during their lifetime by photosynthetic processes, especially in the trunks and branches (70-90% of terrestrial carbon; Saatchi et al., 2011; Häger and Schwendenmann, 2016), which not only buffer the anthropogenic GHG emissions but also produce oxygen (O₂) needed by all living creatures (Canfield, 2014). Furthermore, natural forests provide important ecosystem services (Beck et al., 2008a) like water supply for local and regional populations (e.g. Pan et al., 2011), and they are habitats for countless species of flora and fauna, which sometimes are highly adapted to these specific environmental conditions (Olander et al., 2008). Therefore, the conservation of forest ecosystems, the monitoring of deforestation rates and the estimation of existing C stocks, as well as their changes over time, is of utmost importance to evaluate possible future GHG emissions or the potential of reforested areas as C stocks and sinks (Mitchard et al., 2014).

This especially holds true for tropical forests which only cover about 10% of the Earth's surface (Spracklen and Righelato, 2016), but contain more than 50% of the total C stored in the global forest biomass (Clark et al., 2011). However, tropical forests are suffering an alarming reduction, especially in developing countries, due to population growth and local socioeconomic activities. The anthropogenic pressure on these ecosystems results in high deforestation rates, because large areas are converted into pastures and agricultural land for the livelihood of the local population (Beck et al., 2008b; Ochoa et al., 2015). These interventions provoke degradation of soils and of the ecosystem services, as well as contamination of river courses (fertilizer, sediments, etc.; Swennen and Van der Suys, 2002), besides the release of big amounts of GHG into the atmosphere, mainly consisting of CO₂ and CH₄, due to slash and burn activities (Poulter et al., 2010; Saatchi et al., 2011; IPCC, 2013). Consequently, those disturbed forests lose much of their storage capacity, particularly water and carbon storage (~40%; Céleri and Feyen, 2009; Berenguer et al., 2014), which is why the conservation and restoration of primary tropical forest ecosystems is a priority (FAO, 2015).

For monitoring purposes, field investigations are typically conducted, which implement plots of different sizes and apply direct measurements (Larjavaara and Muller-Landau, 2013; Berenguer et al., 2014; Mauya et al., 2015). These specific plot results are extrapolated for the whole ecosystem to estimate forest cover as well as carbon stocks (Werner and Homeier, 2015). However, the accuracy of extrapolation highly depends on plot distribution and the quality of measurements, especially in mountainous terrain, due to the fast-changing forest structure and climate conditions caused by the complex topography (Paulick et al., 2017). Despite the benefits of the field investigations (historical data, forest inventories, etc.), plot implementation is time consuming and expensive, especially if it is necessary to get data from wider areas and longer time periods. Furthermore, field plot installation and individual measurements might be destructive, especially if trees have to be cut to determine specific tree and wood parameters (Chave et al., 2005, Chave et al., 2006).

An alternative to obtain information about forest cover, deforestation rates and C storage, especially Above Ground Biomass (AGB), is the use of remote sensing data (satellite or aerial photograph and radars). The use of this technology also has the advantage of monitoring wider areas (Yoshikawa and Sanga-Ngoie, 2011; Eastman et al., 2013), which avoids extrapolations and facilitates data even for remote areas. Remote sensors generally measure the radiation reflected by the surface (passive) or scan the surface by means of the emission of electromagnetic waves (active), which also register the height of any object present in the area. The information is arranged and stored in digital formats in different spatial-temporal resolutions (Panda et al., 2013). Therefore, remote sensed datasets provide more complete and comprehensive information respective to the Earth's surface and land cover compared to field plot measurements (Wang et al., 2014). Furthermore, this information can help to analyze and understand the existing changes provoked by anthropogenic impacts at local, regional and country scale.

As mentioned before, remote sensing technologies can be divided into active and passive sensors (Chuvieco and Huete, 2009). On the one hand, active remote sensors (e.g. radars) have the capacity to emit radiation and receive the echo produced by the scanned objects. At the moment, the most effective active sensor is Light Detection and Ranging (LiDAR) (as e.g. Farr et al., 2007; Stephens et al., 2012; Zhang et al., 2017),

which also penetrates the vegetation cover as well as water bodies, and stores the information as a 3D point cloud (Brede et al., 2017). By means of these point clouds it is possible to obtain digital models of the surface (Digital Terrain Models [DTM]), including the vegetation or object heights (Digital Surface Models [DSM]). On the other hand, passive remote sensors receive the energy reflected by objects or the Earth's surface. Generally, the information is obtained by means of satellite and aerial photographs. At the moment some of the most popular satellite platforms are GOES, NOAA, TERRA, AQUA and LANDSAT. However, for tropical zones the acquisition of surface information for land cover classification and forest monitoring is often complicated due to the high cloud frequency during the whole year. Especially affected are the mountain chains where average annual cloudiness of up to 90% is observed (Bendix et al., 2006). Nonetheless, satellites or Unmanned Aerial Vehicle (UAV) also provide multispectral images, which can be used for land cover classification and forest monitoring, such as the estimation of deforestation rates. Satellite data supply information for wider areas in different spatial resolutions (regional or country scales), whereas UAV data is practical for smaller areas (local or ecosystem scale). From the multispectral images different vegetation indices (slope-based and distance-based) can be obtained and land cover classified as well as deforestation rates calculated (e.g. Silleos et al., 2006; Fensholt et al., 2009; Chuvieco and Huete, 2009).

A disadvantage of using passive sensors in tropical regions is the high cloud frequency (Bendix et al., 2004), because the cloud cover (contaminated pixels) does not provide useful information about the Earth's surface. Therefore, the cloud contaminated pixels must be detected and eliminated to avoid false land cover classifications, which leads to gaps in the imagery. To fill these gaps, image composites over larger time periods must be made (Chen et al., 2003; Maisongrande et al., 2004), which makes the monitoring of short-term changes complicated. Multispectral UAV data can provide this short-term information for smaller areas, but this technology is sensitive to climate conditions, because during rainy and windy days a flight execution is impeded. Nonetheless, UAV can also be used for AGB estimations at tree level if they are equipped with an RGB camera and the photographs are taken from different view angles. The obtained images must be processed by photogrammetric methods, such as the structure from motion approach (SfM; Wallace et al., 2016; Burns and Delparte, 2017; Jiang and Jiang, 2018),

which guarantees an acceptable accuracy for the final products (Weber and Lerch, 2018).

For forest classifications at tree level and at regional or local scale, LiDAR is advantageous, because this technology is not affected by clouds and it is also less sensitive to climate conditions. Furthermore, LiDAR permits the detection of the vertical and horizontal forest structure due to its very high resolution and data accuracy (Silva and Bendix, 2013; Asner et al., 2014; Li et al., 2017). Also, AGB can be estimated by applying allometric equations (e.g. Chave et al., 2005) if further tree parameters, such as wood density (WD), height (H) and tree diameter at breast height (DBH), are available (Spracklen and Righelato, 2016).

The disadvantage of LiDAR, on the other hand, is its high survey cost (Purnamasayangasukasih et al., 2016), thus restricting continuous forest monitoring. However, where LiDAR surveys were already performed, the most vulnerable parts can be monitored by UAV (Mlambo et al., 2017; Xiang et al., 2019), because this technology also permits a classification at tree level (RGB camera). This is especially important in developing countries in tropical mountain regions where the complex topography and high survey costs complicate continuous LiDAR data acquisition (Brodu and Lague, 2012).

1.1 Motivation

As explained before, forest classification and monitoring are especially challenging in remote areas in tropical mountain regions, due to the difficulties in access, the patchy forest structures and the harsh climate conditions, especially at higher elevations (e.g. Ferraz et al., 2016; Paulick et al., 2017). Therefore, remote sensing technologies must be applied to avoid extrapolation inaccuracies from field plot measurements, although sporadic field measurements are needed to validate the obtained results (Chave et al., 2019). By means of remote sensing data, land cover can be determined and deforestation rates calculated, as well as AGB and C stocks estimated. To date, land cover information is still scarce or inaccurate in developing countries, especially in tropical mountain zones, but deforestation rates are high (FAO, 2015), for which reason

monitoring of the natural forest stands as well as AGB estimations for different land cover types, including their C stocks, is necessary to identify the most vulnerable parts in order to avoid and mitigate deforestation and, subsequently, future GHG release. To accomplish these objectives, a surveillance system which integrates approaches at different spatial scales should be implemented, using different remote sensing technologies, to provide cost-effective solutions.

For the present investigation Ecuador was selected, because this country shows the highest deforestation rate in South America (FAO, 2010a,b), but is also a hotspot in biodiversity (e.g. Brehm et al., 2008; Homeier et al., 2008), especially the tropical mountain forest (TMF), which also provides important ecosystem services (e.g. water supply; carbon sequestration) not only for the local and regional population (Flores-López et al., 2016). However, the existing literature indicates different deforestation rates over the last decades (e.g. Mosandl et al., 2008; MAE, 2012, Tapia-Armijos et al., 2015), which is why a reliable determination of forest cover, deforestation rates and actual carbon stocks are necessary to analyze the alterations within these ecosystems, as well as to estimate possible GHG emissions caused by the enhanced population pressure and the resulting land use changes (IPCC, 2013; Ochoa et al., 2015).

1.2 Aims and outlines

To date, Ecuador does not possess a specific operational surveillance system which continuously monitors forest cover and deforestation rates at country level. Therefore, the present investigation wants to provide a functional tool based on satellite data to quantify the existing forest cover and to determine the deforestation rates over the last decades. This remote sensing technology takes advantage of the fact that low to moderate resolution satellite imagery is often free of charge and available online (e.g. NOAA-CLASS, 2015). To reach this goal, multispectral long-term satellite data is necessary, which is available from the satellite types “LANDSAT” (since 1972; NASA, 2019) and “NOAA” (since 1981; NOAA, 2019). Landsat provides multispectral images in a spatial resolution between 30m and 60m, however, its temporal resolution lies between 16 and 18 days, which makes continuous monitoring complicated, considering

the high cloud frequency observed over Ecuador (Bendix et al., 2006). The NOAA-AVHRR sensor has a lower spatial resolution (1km) but generates several multispectral images of the same area every day. By means of this information, image composites can be generated more easily and nearly cloud free images obtained for shorter time periods. Furthermore, NOAA-AVHRR image receivers are installed in the Universidad Técnica Particular de Loja (UTPL; operated by the author) and the Instituto Nacional de Meteorología e Hidrología (INAMHI; Ecuadorian weather service) in Quito, which facilitate image acquisition (Bendix et al., 2004). The NOAA-AVHRR data is also widely used to monitor vegetation cover and dynamics over larger areas (e.g. Latifovic et al., 2012; Eastman et al., 2013), because this satellite series provides the longest and most comprehensive source of multispectral data (Wang et al., 2014). By means of the different spectral bands different vegetation indexes can be calculated, and the vegetation cover and state classified, as well as other parameters and metrics derived (Yoshikawa and Sanga-Ngoie 2011).

Once the historical and actual forest cover is determined, deforestation rates over the last decades can be calculated, which, subsequently, leads to the estimation of C stocks within the different forest ecosystems and possible GHG emissions in the future (Mitchard et al., 2014). As mentioned before, the implementation of field plots is expensive and time-consuming and area-wide products derived from field data extrapolation are generally inaccurate. Therefore, an estimation at tree level is required, which can be obtained by means of active sensors (LiDAR). However, LiDAR surveys are expensive, which makes continuous monitoring complicated. Nonetheless, LiDAR covers larger areas (regional or catchment level), which permits the execution of forest inventories and the detection of the most vulnerable parts. By means of the generated 3D point clouds in very high-resolution individual trees can be detected and forest AGB and C stocks calculated, applying allometric equations if auxiliary tree parameters are also available (e.g. Chave et al., 2005). The results, of course, have to be validated by means of sporadic field plot measurements (Chave et al., 2019). Besides this, LiDAR data also detects the forest structure, which is especially challenging in tropical high mountains due to the fast-changing topography and climate conditions (Leuschner et al., 2013; Kim et al., 2016).

Despite the above mentioned, LiDAR surveys are too expensive for continuous forest monitoring, which is why an alternative, especially for the most vulnerable parts, must be considered. A cost-effective alternative are UAVs equipped with an RGB camera (Fritz et al., 2013), which can capture images in very high-resolution from different view angles. This allows for the generation of accurate 3D point clouds for smaller areas, which permits continuous monitoring of the most vulnerable parts and the detection of changes in forest AGB and C stocks (Swinfield et al., 2019). Furthermore, UAVs can be equipped with multispectral cameras, too, which permit the calculation of vegetation indices to evaluate the state of the forest stand (Aasen et al., 2018).

However, the application of these technologies is still scarce in Ecuador, where only isolated information about the forest stands is available. To overcome these knowledge gaps on different scales, the present thesis would like to test the described surveillance system by evaluating the following hypotheses:

- H1** Operationally available satellite data with temporally high but spatially low resolution can be used for forest inventory and deforestation rate calculation at country level.
- H2** LiDAR is capable of detecting forest structure at catchment level in complex TMF terrains and also permits AGB and C stock estimation to determine possible future GHG emissions, respectively the potential of reforested areas for carbon sequestration and storage.
- H3** For continuous forest monitoring of the most vulnerable parts, UAVs represent a cost-effective alternative to determine changes in forest structure and AGB stocks.

1.3 Approach

This section briefly describes the processing chain to verify the established hypothesis by means of information from passive and active remote sensing sensors (satellite images, LiDAR and UAV; Figure 1-1).

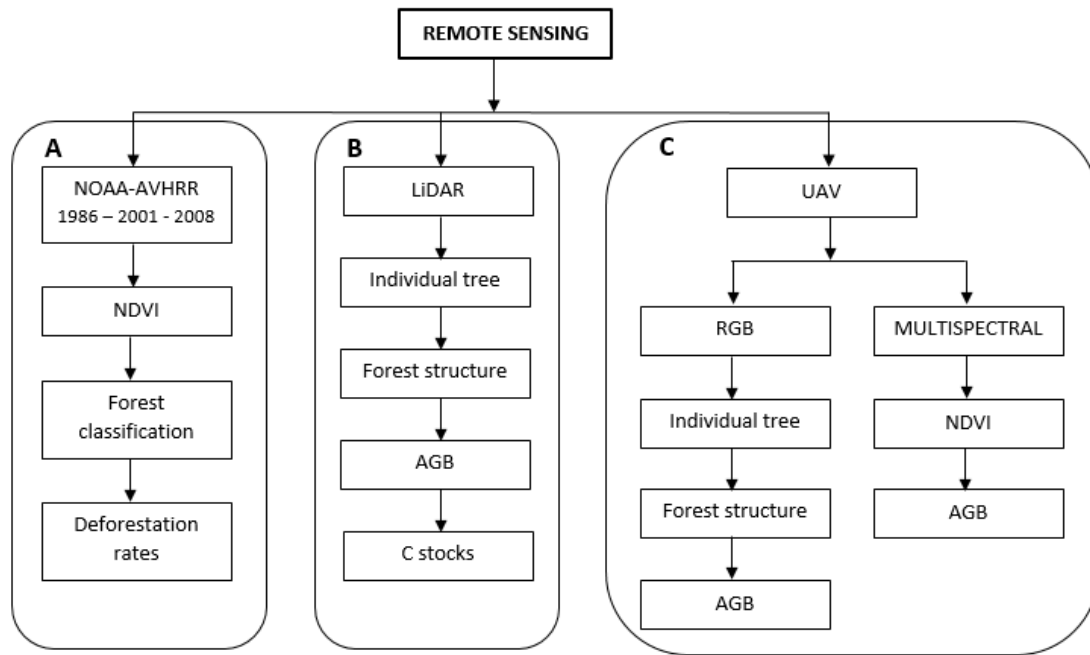


Figure 1-1: Processing chain for forest monitoring at different spatial scales using remote sensing data: (A) corresponds to forest classification and deforestation rate calculation at country level, (B) to AGB estimation in complex TMF terrain at catchment level, and (C) to continuous forest monitoring of most vulnerable parts using a UAV.

First, satellite data is consulted to provide a functional tool for forest monitoring of continental Ecuador, including its changes over time. Therefore, NOAA-AVHRR images are used and the Normalized Difference Vegetation Index (NDVI) calculated to classify the vegetation cover into “forest” – “non-forest” areas. The study period corresponds to the last decades (1986 – 2001 and 2001 – 2008), for which the respective deforestation rates are calculated. The approach is based on a decision tree algorithm (Hansen et al., 2000), which additionally includes topographic and climatic thresholds to precisely detect all forest stands. Furthermore, to avoid false classifications caused by the high cloud frequency observed over Ecuador, image composites are generated, applying the Maximum Value Composite (MVC) method (e.g. Maisongrande, 2004). The results are validated by means of two training sites located in the north and south of the country at different elevations.

Then, AGB and C stocks in a TMF are estimated, specifically in the San Francisco catchment in southern Ecuador, where the Estación Científica San Francisco (ECSF) is

located. For this area high resolution LiDAR data are available (Silva and Bendix, 2013) as well as field plot measurements to validate the results (e.g. Werner and Homeier, 2015). By means of LiDAR data, a high-resolution Digital Terrain Model (DTM) and Digital Surface Model (DSM) are generated, from which the Height (H) and location of individual trees can be determined. The individual tree detection also provides information respective to the vertical and horizontal forest structure, which allows for the detection of the fast-changing forest structure, which is caused by different topographic and environmental conditions (e.g. Cabrera et al., 2019). The TMF in the San Francisco catchment can generally be divided into ravine and ridge forest parts. The ravine forest is characterized by lower stem density, but greater basal areas (tree diameters) and higher canopies when compared to the ridge forest, where less tree species are also observed (Dieslich and Huth, 2012). To calculate the AGB (Mg ha^{-1}) the allometric equation for wet tropical forest proposed by Chave et al. (2005) is applied, combining the individual H from the LiDAR data and auxiliary tree parameters from field measurements, particularly Diameter at Breast Height (DBH) and average Wood Density (WD).

Finally, two different methods are evaluated for continuous forest monitoring of the most vulnerable parts by means of a UAV. On the one hand, an RGB camera is used to generate 3D point clouds, applying the photogrammetric technique “Structure for Motion” (SfM). This permits the detection of individual trees and the forest structure within smaller areas, as well as for the calculation of AGB values (Mg ha^{-1}). On the other hand, a multispectral camera is used to deviate the NDVI of the forest part in very high resolution. This vegetation index is the input to calculate AGB (Mg ha^{-1}) in evergreen tropical forests applying the equation proposed by Das and Singh (2016). The accuracy of both methods is evaluated comparing the UAV results with the AGB values derived from LiDAR data for the same area.

1.4 References

- Aasen H, Honkavaara E, Lucieer A, Zarco-Tejada PJ (2018): Quantitative Remote Sensing at Ultra-High Resolution with UAV Spectroscopy: A Review of Sensor Technology, Measurement Procedures, and Data Correction Workflows. *Remote Sens.* **10**: 1091.
- Asner GP, Mascaro J (2014): Mapping tropical forest carbon: Calibrating plot estimates to a simple LiDAR metric. *Remote Sens. Environ.* **140**: 614–624.
- Beck E, Makeschin F, Haubrich F, Richter M, Bendix, Valarezo C (2008a): The Ecosystem (Reserva Biológica San Francisco). In: Beck E, Bendix J, Kottke I, Makeschin F, Mosandl R. (eds.): *Gradients in a tropical mountain ecosystem of Ecuador*. Ecological Studies **198**, Springer-Verlag, Berlin, Heidelberg, Germany: 1–13.
- Beck E, Harting K, Roos K (2008b): Forest clearing by slash and burn. In *Gradients in a Tropical Mountain Ecosystem of Ecuador*. In: Beck E, Bendix J, Kottke I, Makeschin F, Mosandl R. (eds.): *Gradients in a tropical mountain ecosystem of Ecuador*. Ecological Studies **198**, Springer-Verlag, Berlin, Heidelberg, Germany: 371–374.
- Bendix J, Rollenbeck R, Palacios E (2004): Cloud detection in the Tropics - a suitable tool for climate-ecological studies in the high mountains of Ecuador. In: *International Journal of Remote Sensing* **25**: 4521–4540.
- Bendix J, Rollenbeck R, Göttlicher D, Cermak J (2006): Cloud occurrence and cloud properties in Ecuador. *Inter-Research Climate Research* **30**: 133–147.
- Berenguer E, Ferreira J, Gardner TA, Aragão LEOC, De Camargo PB, Cerri CE, Durigan M, De Oliveira RC, Vieira ICG, Barlow J (2014): A large-scale field assessment of carbon stocks in human-modified tropical forests. *Glob. Chang. Biol.* **20**: 3713–3726.
- Brede B, Lau A, Bartholomeus H, Kooistra L (2017): Comparing RIEGL RiCOPTER UAV LiDAR derived canopy height and DBH with terrestrial LiDAR. *Sensors* **17**(10): 2371.
- Brehm G, Homeier J, Fiedler K, Kottke I, Illig J, Nöske NM, Werner F, Breckle S-W (2008): Mountain Rain Forests in Southern Ecuador as a Hotspot of Biodiversity – Limited Knowledge and Diverging Patterns. In: Beck E, Bendix J, Kottke I, Makeschin F, Mosandl R. (eds.), *Gradients in a Tropical Mountain Ecosystem of Ecuador*. Ecological Studies **198**, Springer-Verlag, Berlin, Heidelberg, Germany: 15–23.

- Brodu N, Lague D (2012): 3D terrestrial lidar data classification of complex natural scenes using a multi-scale dimensionality criterion: Applications in geomorphology, *ISPRS Journal of Photogrammetry and Remote Sensing* **68**: 121-134.
- Burns JHR, Delparte D (2017): Comparison of commercial structure-from-motion photogrammetry software used for underwater three-dimensional modeling of coral reef environments, *Int. Arch. Photogramm. Remote Sens. 2017. Spatial Inf. Sci.*, **XLII-2/W3**: 127-131.
- Cabrera O, Fries A, Hildebrandt P, Günter S, Mosandl R (2019): Early Growth Response of Nine Timber Species to Release in a Tropical Mountain Forest of Southern Ecuador. *Forests* **10**: 254.
- Canfield DE (2014): *Oxygen - a four billion year history*. Princeton University Press, United Kingdom.
- Célleri R, Feyen J (2009): The Hydrology of Tropical Andean Ecosystems: Importance, Knowledge Status, and Perspectives. *Mountain Research and Development* **29**(4): 350-55.
- Berenguer E, Ferreira J, Gardner TA, Aragão LEOC, De Camargo PB, Cerri CE, Durigan M, De Oliveira RC, Vieira ICG, Barlow J (2014): A large-scale field assessment of carbon stocks in human-modified tropical forests. *Glob. Chang. Biol.* **20**: 3713–3726.
- Chave J, Andalo C, Brown S, Cairns MA, Chambers JQ, Eamus D, Fölster H.; Fromard, F, Higuchi N, Kira T, Lescure JP, Nelson BW, Ogawa H, Puig H, Riéra B, Yamakura T (2005): Tree allometry and improved estimation of carbon stocks and balance in tropical forests. *Oecologia* **145**: 87–99.
- Chave J, Muller-Landau H, Baker T, Easdale T, Steege H, Webb C (2006): Regional and phylogenetic variation of wood density Across 2456 neotropical tree species. *Ecological Applications* **16**(6): 2356–2367.
- Chave J, Davies SJ, Phillips OL, Simon L, Lewis SL, Sist P, Schepaschenko D, Armston J, Baker TR, Coomes D, Disney M, Duncanson L, Hérault B, Labrière N, Meyer V, Réjou-Méchain M, Scipal C, Saatchi S (2019): Ground data are essential for Biomass Remote Sensing Missions. *Surv Geophys* **40**: 863.
- Chen PY, Srinivasan R, Fedosejevs G, Kiniry JR (2003): Evaluating different NDVI composite techniques using NOAA-14 AVHRR data. *International Journal of Remote Sensing* **24**: 3403–3412.
- Chuvieco E, Huete A (2009): *Fundamentals of satellite remote sensing*. CRC Press. Boca Raton.

- Clark ML, Roberts DA, Ewel JJ, Clark, DB (2011): Estimation of tropical rain forest aboveground biomass with small-footprint lidar and hyperspectral sensors. *Remote Sens. Environ* **115**: 2931–2942.
- Das S, Singh TP (2016): Forest Type, Diversity and Biomass Estimation in Tropical Forests of Western Ghat of Maharashtra Using Geospatial Techniques. *Small-Scale For.* **15**: 517.
- Dislich C, Huth A (2012): Modelling the impact of shallow landslides on forest structure in tropical montane forests. *Ecol. Model.* **239**: 40–53.
- Eastman JR, Sangermano F, Machado EA, Rogan J, Anyamba A (2013): Global trends in seasonality of Normalized Difference Vegetation Index (NDVI), 1982–2011. *Remote Sensing* **5**: 4799–4818.
- FAO (2010a): (Food and Agriculture Organization of the United Nations) Evaluación de recursos forestales mundiales 2010 – Informe principal. Roma. [<http://www.fao.org/3/i1757s/i1757s.pdf>; accessed: March 2016]
- FAO (2010b): (Food and Agriculture Organization of the United Nations) (2010b): Evaluación de los recursos forestales mundiales 2010 – Informe Nacional Ecuador. Roma. [<http://www.fao.org/3/a-az203s.pdf>; accessed: March 2016]
- FAO (2015): (Food and Agriculture Organization of the United Nations) Global Forest Resources Assessment 2015 Desk Reference; Food and Agriculture Organization of the United Nations: Rome, Italy. [<http://www.fao.org/forest-resources-assessment/current-assessment/en/>; accessed: March 2016]
- Farr TG, Rosen PA, Caro E, Crippen R, Duren R, Hensley S, Kobrick M, Paller M, Rodriguez E, Roth L, Seal D, Shaffer S, Shimada J, Umland J, Werner M, Oskin M, Burbank D, Alsdorf D (2007): The Shuttle Radar Topography Mission. *Reviews of Geophysics* **45**.
- Fensholt R, Rasmussen K, Nielsen TT, Mbow C (2009): Evaluation of earth observation based long term vegetation trends - Intercomparing NDVI time series trend analysis consistency of Sahel from AVHRR GIMMS, Terra MODIS and SPOT VGT data. *Remote Sensing of Environment* **113**: 1886–1898.
- Ferraz A, Saatchi S, Mallet C, Jacquemoud S, Goncalves G, Silva AA, Soares P, Tomé M, Pereira L (2016): Airborne Lidar Estimation of Aboveground Forest Biomass in the Absence of Field Inventory. *Remote Sens.* **8**: 653.
- Flores-López F, Galaiti SE, Escobar M, Purkey D (2016): Modeling of Andean páramo ecosystems' hydrological response to environmental change. *Water (Switzerland)* **8**: 94.

- Fritz A, Kattenborn T, Koch B (2013): Uav-Based Photogrammetric Point Clouds—Tree STEM Mapping in Open Stands in Comparison to Terrestrial Laser Scanner Point Clouds. *Isprs - Int. Arch. Photogramm. Remote Sens. Spat. Inf. Sci.* **XL-1/W2**: 141–146.
- Hansen MC, DeFries RS, Townshend JRG, Sohlberg R (2000): Global land cover classification at 1 km spatial resolution using a classification tree approach. In: *International Journal Remote Sensing* **21**: 1331–1364.
- Häger A, Schwendenmann L (2016): Forest Carbon Sequestration and Global Change. In *The Paradigm of Forests and the Survival of the Fittest*; Molina-Murillo, S.A., Rojas, C., Eds.; CRC Press: Boca Raton, FL, USA; London, UK; New York, NY, USA: 39–86.
- Homeier J, Werner FA, Gradstein SR, Breckle S-W, Richter M (2008): Potential vegetation and floristic composition of Andean forests in South Ecuador, with a focus on the RBSF. In: Beck E, Bendix J, Kottke I, Makeschin F, Mosandl R. (eds.), *Gradients in a Tropical Mountain Ecosystem of Ecuador. Ecological Studies* 198, Springer-Verlag, Berlin, Heidelberg, Germany: 87-100.
- IPCC (2013): (Intergovernmental Panel on Climate Change) Working Group I Contribution to the IPCC fifth assessment report climate change 2013: The Physical Science Basics. IPCC, Stockholm.
- Jiang S, Jiang W (2018): Efficient SfM for Oblique UAV Images: From Match Pair Selection to Geometrical Verification. *Remote Sens.* **10**: 1246.
- Kim E, Lee WK, Yoon M, Lee JY, Son Y (2016): Abu Salim, K. Estimation of Voxel-Based Above-Ground Biomass Using Airborne LiDAR Data in an Intact Tropical Rain Forest, Brunei. *Forests* **7**: 259.
- Kou W, Liang C, Wei L, Hernandez AJ, Yang X (2017): Phenology-based method for mapping tropical evergreen forests by integrating of MODIS and Landsat imagery. *Forests* **8**: 34.
- Larjavaara M, Muller-Landau HC (2013): Measuring tree height: A quantitative comparison of two common field methods in a moist tropical forest. *Methods Ecol. Evol.* **4**: 793–801.
- Latifovic R, Pouliot D, Dillabaugh C (2012): Identification and correction of systematic error in NOAA AVHRR long-term satellite data record. *Remote Sensing of Environment* **127**: 84–97.
- Leuschner C, Zach A, Moser G, Homeier J, Graefe S, Hertel D, Wittich B, Soethe N, Iost S, Röderstein M, Horna V, Wolf K (2013): The Carbon Balance of Tropical Mountain Forests Along an Altitudinal Transect. In: *Ecosystem Services*,

- Biodiversity and Environmental Change in a Tropical Mountain Ecosystem of South Ecuador, *Ecological Studies*; Bendix J, Beck E, Bräuning A, Makeschin F, Mosandl R, Scheu S, Wilcke W, Eds.; Springer: Berlin, Germany, 221: 117–139.
- Li A, Dhakal S, Glenn NF, Spaete LP, Shinneman DJ, Pilliod DS, Arkle RS, McIlroy SK (2017): Lidar Aboveground Vegetation Biomass Estimates in Shrublands: Prediction, Uncertainties and Application to Coarser Scales. *Remote Sens.* **9**: 903.
- MAE (2012): (Ministerio del Ambiente | Ecuador) Línea base de deforestación del Ecuador Continental. Quito. [<http://sociobosque.ambiente.gob.ec/files/Folleto%20mapa-parte1.pdf>; accessed: June 2015]
- Maisongrande P, Duchemin B, Dedieu G (2004): VEGETATION/SPOT: an operational mission for the Earth monitoring; presentation of new standard products. *International Journal of Remote Sensing* **25**: 9–14.
- Mauya EW, Hansen EH, Gobakken T, Bollandas OM, Malimbwi RE, Naesset E (2015): Effects of field plot size on prediction accuracy of aboveground biomass in airborne laser scanning-assisted inventories in tropical rain forest of Tanzania. *Carbon Balance Manag.* **10**: 10.
- Mitchard ETA, Feldpausch TR, Brien RJW, Lopez-Gonzalez G, Monteagudo A, Baker TR, Lewis SL, Lloyd J, Quesada CA, Gloor M, et al., (2014): Markedly divergent estimates of Amazon forest carbon density from ground plots and satellites. *Glob. Ecol. Biogeogr.* **23**: 935–946.
- Mlambo R, Woodhouse IH, Gerard F, Anderson K (2017): Structure from Motion (SfM) Photogrammetry with Drone Data: A Low Cost Method for Monitoring Greenhouse Gas Emissions from Forests in Developing Countries. *Forests* **8**: 68.
- Mosandl R, Günter S, Stimm B, Weber M (2008): Ecuador suffers the highest deforestation rate in South America. In: Beck E, Bendix J, Kottke I, Makeschin F, Mosandl R. (eds.): *Gradients in a tropical mountain ecosystem of Ecuador. Ecological Studies* **198**, Springer-Verlag, Berlin, Heidelberg, Germany: 37-40.
- NASA (2019): The Enhanced Thematic Mapper Plus. [<https://landsat.gsfc.nasa.gov/the-enhanced-thematic-mapper-plus/>; accessed: June 2019]
- NOAA-CLASS (2015): NOAA's Comprehensive Large Array-data Stewardship System (CLASS). <http://www.class.noaa.gov> (Date: 25.06.2015).
- NOAA (2019): History of NOAA Satellites. [<https://www.nesdis.noaa.gov/content/history-noaa-satellites>; accessed: June 2019]

- Olander LP, Gibbs HK, Steininger M, Swenson JJ, Murray BC (2008): Reference scenarios for deforestation and forest degradation in support of REDD: a review of data and methods. *Environmental Research Letters* **3**: 025011.
- Ochoa-Cueva P, Fries A, Montesinos P, Rodríguez-Díaz JA, Boll J (2015): Spatial Estimation of Soil Erosion Risk by Land-cover Change in the Andes of Southern Ecuador. *L. Degrad. Dev.* **26**: 565–573.
- Pan Y, Birdsey RA, Fang J, Houghton R, Kauppi PE, Kurz WA, Phillips OL, Shvidenko A, Lewis SL, Canadell JG, Ciais P, Jackson RB, Pacala SW, McGuire AD, Piao S, Rautiainen A, Sitch S, Hayes DA (2011): Large and Persistent Carbon Sink in the World's Forests. *Science* **333**: 988–993.
- Panda SS, Rao MN, Thenkabail PS, Fitzgerald JE (2016): Remote Sensing Systems—Platforms and Sensors: Aerial, Satellite, UAV, Optical, Radar, and LiDAR. In: Prasad S, Thenkabail PS (ed): *Remote Sensing Handbook, Volume I, Remotely Sensed Data Characterization, Classification, and Accuracies*. Boca Raton, U.S: 3 – 60.
- Paulick S, Dislich C, Homeier J, Fischer R, Huth A (2017): The carbon fluxes in different successional stages: Modelling the dynamics of tropical montane forests in South Ecuador. *For. Ecosyst.* **4**: 5.
- Poulter B, Hattermann F, Hawkins ED, Zaehle S, Sitch S, Restrepo-Coupe N, Heyder U, Cramer W (2010): Robust dynamics of Amazon dieback to climate change with perturbed ecosystem model parameters. *Global Change Biology* **16**: 2476–2495.
- Purnamasayangasukasih RP, Norizah K, Ismail AAM, Shamsudin I (2016): A review of uses of satellite imagery in monitoring mangrove forests. *IOP Conference Series: Earth and Environmental Science* **37**: 012034.
- Saatchi SS, Harris NL, Brown S, Lefsky M, Mitchard ETA, Salas W, Zutta BR, Buermann W, Lewis SL, Hagen S, Petrova S, White L, Morel, A (2011): Benchmark map of forest carbon stocks in tropical regions across three continents. *Proceedings of the National Academy of Science of the United States of America* **108**: 9899–9904.
- Silva B, Bendix J (2013): Remote sensing of vegetation in a tropical mountain ecosystem: Individual tree-crown detection. *Proc. SPIE* **2013**: 8893.
- Silleos NG, Alexandridis TK, Gitas IZ, Perakis K (2006): Vegetation Indices: Advances Made in Biomass Estimation and Vegetation Monitoring in the Last 30 Years, *Geocarto International*, **21**:4: 21-28.

- Spracklen DV, Righelato R (2016): Carbon storage and sequestration of re-growing montane forests in southern Ecuador. *For. Ecol. Manag.* **364**:139–144,
- Swennen R, Van der Suys J (2002): Anthropogenic impact on sediment composition and geochemistry in vertical overbank profiles of river alluvium from Belgium and Luxembourg. *Journal of Geochemical Exploration*, **75**, 1-3: 93-105.
- Swinfield T, Lindsell JA, Williams JV, Harrison RD, Habibi A, Gemita E, Schönlieb CB, Coomes DA (2019): Accurate Measurement of Tropical Forest Canopy Heights and Aboveground Carbon Using Structure From Motion. *Remote Sens.* **11**: 928.
- Stephens PR, Kimberley MO, Beets PN, Paul TSH, Searles N, Bell A, Brack C, Broadley J (2012): Airborne scanning LiDAR in a double sampling forest carbon inventory. *Remote Sens. Environ.* **117**: 348–357.
- Tapia-Armijos MF, Homeier J, Espinosa CI, Leuschner C, de la Cruz M (2015): Deforestation and forest fragmentation in South Ecuador since the 1970s – losing a hotspot of biodiversity. *PLOS ONE* **10**(9): e0133701.
- Wang L, Xiao P, Feng X, Li H, Zhang W, Lin J (2014): Effective compositing method to produce cloud-free AVHRR image. *IEEE Geoscience and Remote Sensing Letters* **11**: 328–332.
- Wallace L, Lucieer A, Malenovsky Z, Turner D, Vopenka P (2016): Assessment of Forest Structure Using Two UAV Techniques: A Comparison of Airborne Laser Scanning and Structure from Motion (SfM) Point Clouds. *Forests* **7**: 62.
- Weber A, Lerch T (2018): Point Clouds: Lase Scanning versus UAS Photogrammetry. *GIM Int.* **4**: 36–39.
- Werner FA, Homeier J (2015): Is tropical montane forest heterogeneity promoted by a resource-driven feedback cycle? Evidence from nutrient relations, herbivory and litter decomposition along a topographical gradient. *Funct. Ecol.* **29**: 430–440.
- Xiang T-Z, Xia G-S, Zhang L (2019): Mini-UAV-based Remote Sensing: Techniques, Applications and Prospectives. *IEEE Geoscience and Remote Sensing Magazine* **7**(3): 29-63.
- Yoshikawa S, Sanga-Ngoie K (2011): Deforestation dynamics in Mato Grosso in the southern Brazilian Amazon using GIS and NOAA/AVHRR data. *International Journal of Remote Sensing* **32**: 523–544.
- Zhang Z, Cao L, She G (2017): Estimating forest structural parameters using canopy metrics derived from airborne LiDAR data in subtropical forests. *Remote Sens.* **9**: 940.

2 Assessment of deforestation during the last decades in Ecuador using NOAA-AVHRR satellite data

This chapter is published in *Erdkunde* 2016, **70**(3):217-235

Received: 19 July 2015 / **Accepted:** 7 June 2016

ASSESSMENT OF DEFORESTATION DURING THE LAST DECADES IN ECUADOR USING NOAA-AVHRR SATELLITE DATA

Víctor González-Jaramillo, Andreas Fries, Rütger Rollenbeck, Jhoana Paladines,
Fernando Oñate-Valdivieso, Jörg Bendix

Summary

Human activities during the last decades provoked a notable reduction in global forest cover. Knowing that forest stands act as stock and sinks for carbon and other greenhouse gases, it is important to determine the existing forest cover at country level and to calculate annual deforestation rates. This work uses NOAA satellite images in a resolution of 1km x 1km to classify the surface of continental Ecuador in “forest” - “non-forest” pixels and to estimate the annual deforestation rate from 1986 to 2001 as well as from 2001 to 2008. The method is based on a decision tree algorithm that includes different spectral bands of the NOAA-AVHRR sensor and additional topographic and meteorological parameters.

The results show that the total forest cover of continental Ecuador was reduced from 48.1% in 1986 to 36.8% in 2008. The calculated annual deforestation rates indicate that forest reduction increased during the last decade. The most affected area is the Coastal Lowland, due to the enhanced population pressure, followed by the Amazon Basin, not only caused by the governmental supported oil and mining industry, but also due to the uncontrolled timber extraction. The Andean Highland has been less affected, because the major parts of this region were deforested before, during the Pre-Columbian-Era.

Keywords

Remote sensing, NOAA image processing, Forest cover, Annual deforestation rates, Ecuador

2.1 Introduction

Tropical forests cover about 7% of the Earth's surface and are home to millions of species (e.g. Olander et al. 2008), but during the most recent decades big parts of this unique ecosystem got lost because of human activities. The conversion from forest into pasture or agricultural land took place in all tropical countries, but especially in South-America, where highest deforestation rates are observed (FAO 2010a). Deforestation not only has serious impacts on native species, but also on global climate. As Aguiar et al. (2012) mentioned, deforestation in tropical regions is one of the key components of climate change. Burn activities lead to massive emissions of CO₂, CH₄ and other greenhouse gases into the atmosphere (e.g. Poulter et al. 2010; Saatchi et al. 2011; IPCC 2013). One-third of total greenhouse gas emissions are caused by agriculture practices, which also includes indirect emissions from deforestation as well as from land use-changes (Gilbert 2012). The global portion resulting from deforestation is estimated at 20% (Olander et al. 2008), which is a considerable fraction relative to total global warming.

Global warming leads to an additional pressure on the tropical ecosystems by coercing species into rapid adaptation. With a mean temperature increase of only 1°C per century, ecological zones shift poleward up to 160km (Thuiller 2007) while the altitudinal belts inside mountainous areas are also modified. This results in an increased rate of species extinction, because the time span to acclimatize, especially for highly adapted species, is too short (Thomas et al. 2004).

Besides global warming, deforestation in tropical forest ecosystems also has a direct impact on the regional and local climate. Fries et al. (2009) and Fries et al. (2012) showed in their studies the conversion from forest into pasture leads to higher temperature amplitudes and less water availability for evapotranspiration processes; the water availability decreases due to the increased runoff over deforested areas. Together with the predicted alterations in rainfall distribution and their amounts, the hydrological cycle may be modified, especially in the most affected regions. The hydrological cycle is fundamental for the primary production of an ecosystem, because the water cycle provides the main ecosystem services (e.g. nutrient availability; Breuer et al. 2013). The expectable modifications in local climate and the water cycle do not only affect species composition and reforestation efforts, but also endanger the water supply for the local population.

Therefore, knowledge about the spatial forest distribution and the human impact on ecosystems are crucial requirements for quantifying biosphere sinks and atmospheric sources of greenhouse gases (DeFries et al. 2000). With countrywide vegetation maps, the stocks and emissions of greenhouse gases can be determined and the most affected areas can be depicted at a local and regional scale (e.g. Tan et al. 2007; Moraes et al. 2013).

The highest deforestation rates in South America are reported for Ecuador (FAO 2010a,b). Thereby, not only the tropical lowland forest is affected, but also the tropical mountain forest (Mosandl et al. 2008). This is especially critical in the Ecuadorian Andes, a global hot spot in biodiversity, where an exceptional abundance of endemic species is located (e.g. Barthlott et al. 2007; Beck et al. 2008; Brehm et al. 2008). The Ecuadorian tropical mountain forest is reduced by slash-and burn activities, due to the growing population and economic incentives as well as the tropical lowland forest in the Amazon Basin, because of the governmental supported oil and mining industry (e.g. Ochoa et al. 2015).

Unfortunately, Ecuador does not have operational surveillance systems to monitor ongoing deforestation. Existing observations are scarce, especially for remote areas, including tropical mountain forest, paramos, and the tropical lowland forest in the Amazon Basin (FAO 2010a). The available datasets are mainly estimates based on statistical models and extrapolations of point observations. As the FAO report (2010b) specifies, the forest cover as well as the annual deforestation rates for Ecuador during the time periods 1990-2000, 2000-2005 and 2005-2010 were calculated by means of regression analyses and projections methods, because of the deficient data availability.

For a reliable quantification of forest cover and its reduction over time, satellite data supply a fast and efficient tool, especially for remote areas (e.g. Yoshikawa and Sanga-Ngoie 2011). Satellite data is widely used for vegetation classifications at a global, continental and local scale. Global vegetation estimations are published in Eastman et al. (2013), using NOAA-AVHRR data (National Oceanic and Atmospheric Administration - Advanced Very High Resolution Radiometer). Another, more recent application is the Global Forest Watch initiative, which generated worldwide forest cover maps based on Landsat satellite data (Global Forest Watch, 2015). For continental South-America, Latifovic et al. (2005) and Yoshikawa and Sanga-Ngoie (2011) also presented vegetation and forest cover maps using NOAA-AVHRR data. At a local scale Göttlicher et al. (2009)

published a vegetation classification for southern Ecuador by means of Landsat satellite data.

On a continental to global scale, NOAA-AVHRR satellite data have been widely used to monitor and classify vegetation cover and dynamics (e.g. Zhang et al. 2003; Latifovic et al. 2005; Fuller 2006; Eastman et al. 2013), because this satellite series provides the longest and most comprehensive source of remotely sensed data (Wang et al. 2014). To classify the vegetation cover, composites of the different spectral bands of the NOAA-AVHRR sensor are used to calculate the NDVI (Normalized Difference Vegetation Index) and other derived parameters and metrics (e.g. Loveland et al. 2000; Yoshikawa and Sanga-Ngoie 2011).

Previous studies in South America applied Principal Component Analysis (PCA) for forest classification in specific regions (e.g. Amazon Basin; Nonomura et al. 2003; Yoshikawa and Sanga-Ngoie 2011). However, there are still systematic errors inside the NOAA-AVHRR data used, because the degradation of the spectral images over the life time of the satellite is often not taken into account adequately (Latifovic et al. 2012). Furthermore, forest can only be classified at cloud free pixels within the satellite images (e.g. Wang et al. 2014), which is especially problematic in Ecuador. As Bendix et al. (2004) and Bendix et al. (2006) showed, the relative annual cloud frequency over some specific areas in Ecuador is frequently higher than 90%.

Hence, the objective of the present paper is to create forest cover maps for continental Ecuador at a national scale, wherefore the established correction algorithms are adapted to the local conditions. By means of these maps, the annual deforestation rates for the periods 1986 to 2001 and 2001 to 2008 are calculated. This product will be helpful as a baseline for initiatives such as REDD (Reducing Emissions from Deforestation and Forest Degradation), which was implemented by the Ecuadorian Environmental Ministry (MAE - Ministerio del Ambiente) in 2008 (MAE 2015).

To reach these targets, a combination of different methods is applied: First NOAA-AVHRR images are corrected by radiometric adjustments, using the optimized coefficients published by Latifovic et al. (2012). Then geometric rectification of the images is processed, applying orbital satellite parameters and “Image Matching” with ancillary data (Eugenio and Marquez 2003) derived from Landsat satellite images. Finally, to overcome the high cloudiness and cloud contour effects in the satellite image, a combination of the cloud classification and images composition is executed. The final

forest classification is based on a decision tree method adapted from Hansen et al. (2000), which additionally includes topographic and climatic parameters.

The paper is structured as follows: In section 2 the study area and the data are presented. Section 3 explains the used methods of the instant forest classification and the calculation of the annual deforestation rates per period. In section 4 the results are presented, discussed and validated. The paper ends with general conclusions.

2.2 Study area and data

The study has been executed in Ecuador, bordering on Colombia in the north, on Peru in the south and east and by the Pacific Ocean to the west ($\sim 1^{\circ}\text{N}$ to 5°S ; $\sim 75^{\circ}\text{W}$ to 81°W). The altitude ranges from sea-level up to over 6000m at the highest Andean mountain peaks. The Andes cross the country from the north to the south, wherefore the country can be divided into three principal climatic regions: the Coastal Lowland in the west, the Andean Highland in the centre (Sierra) and the Amazon Basin in the east (fig.2-1).

The natural vegetation in Ecuador is determined by these three principal climatic regions. The Coastal Lowland is characterized by semi-deciduous, deciduous forests and savannas; the Amazon Basin by tropical rain forest. The Andean Highland contains altitudinal vegetation belts (Bendix et al. 2008), which can be classified in montane broad-leaved forest and the upper montane forests (Elfin forest), otherwise known as the Ceja Andina. These two forest types are well developed on the eastern escarpment of the Andes and in the northern parts of the western Cordillera. Further to the south at the coastal Cordillera these forest types become more isolated, due to the drier climate conditions and Dry-Forest vegetation and savannas prevail (Dierl 2010). At higher elevations in the northern and central parts grass-páramo vegetation is formed, while shrub-páramo vegetation dominates in the southern part. This difference is caused by the Andean Depression situated between southern Ecuador and northern Peru (Richter 2003), leading to different climatic conditions. The upper treeline in the northern and central parts is situated at $\sim 4000\text{m}$ asl, determined by the temperature and moisture content of the air; at the southern part the treeline is notably lower ($2700\text{m} - 3300\text{m}$ asl), probably caused by the stronger wind conditions (Beck et al. 2008). Nevertheless, biodiversity is extraordinarily high in the area of the Andean Depression, due to the lower top altitudes,

which facilitate the exchange between the coastal and the Amazonian vegetation (e.g. Myers et al. 2000; Barthlott et al. 2005; Homeier et al. 2008).

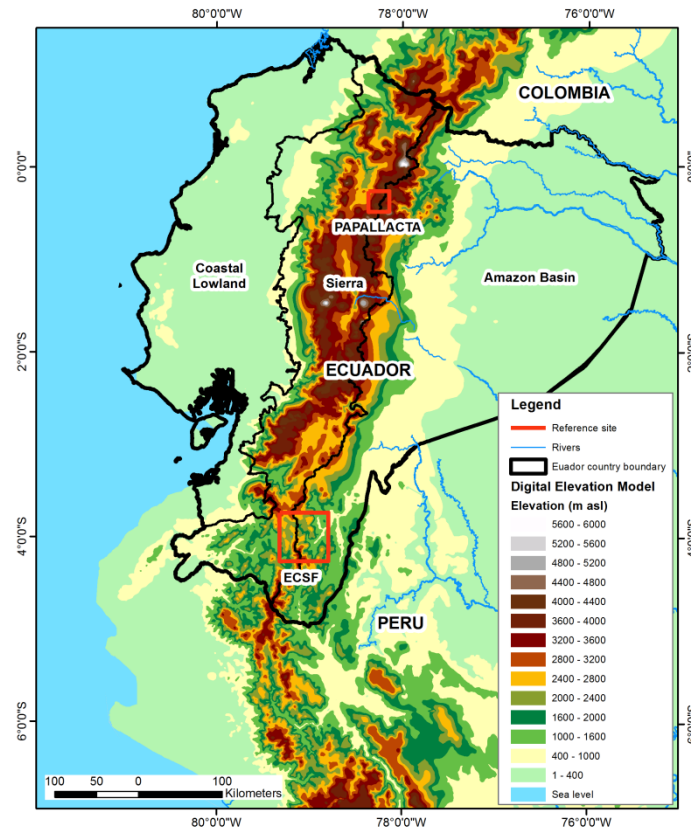


Figure 2-1: Digital Elevation Model (DEM; adapted from Farr et al. 2007) of the research area (continental Ecuador), including the three principal regions: Coastal Lowland, Andean Highland and Amazon Basin, as well as the reference sites for validation.

As mentioned above, deforestation rates are highest in Ecuador compared to the other countries in South America (Mosandl et al. 2008; FAO 2010a). Wunder (2000) assumed that the surface of Ecuador was originally covered with forest by 90% (~25 million ha). This is also confirmed by Cabarle et al. (1989), who estimated an original forest cover of about 26 million ha. There are two main deforestation periods in Ecuador: First a long-lasting deforestation in the Andean Highland over 1200m asl during the Pre-Colombian-Era and second a fast forest reduction in the Coastal Lowland during the last century (Mosandl et al. 2008). The Coastal Lowland forest was replaced by agricultural crops during the cacao-boom (1900 – 1920) and the banana-boom (1950 – 1965; Cabarle et al. 1989). The reduction of the Amazonian rain forest took place in the 1970s, caused by the oil-boom. Until 1990 the total forest cover of continental Ecuador was reduced to 48.7% and for 2010 a forest cover of about 34.7% was calculated (~9.9 million ha; FAO 2010b).

The recent deforestation mostly does not affect the primary forest areas, because the majority of these areas are protected. The actual deforestation is mainly observed in secondary forest areas and in the mountain forest ecotones, where nearly the complete forest cover has been replaced by pastures (Mosandl et al. 2008). Besides the recent land use change from forest to pasture, only small areas of reforestation are recorded for Ecuador compared to other countries in South-America. This additionally amplifies the deforestation rates for Ecuador and leads to the highest values at country level (FAO 2010a).

The Digital Elevation Model (DEM, fig.2-1) used in this study was originally created during the Shuttle Radar Topography Mission (SRTM) in 2007 and the data can be freely accessed online (http://www2.jpl.nasa.gov/srtm/southAmerica_sp.htm). The single steps of the DEM generation are published in Farr et al. (2007). For this approach the SRTM data was resampled to 1km x 1km to obtain the same resolution as the NOAA-AVHRR images.

Satellite data for vegetation classification are available from 1970s to present from different satellite types. The spatial resolution of the images depends on the sensor type installed, ranging from low resolution (4km x 4km; GOES imagery, Simic et al. 2004), over coarse resolution (1km x 1km; e.g. NOAA-AVHRR), moderate or medium resolution (up to 250m x 250m; e.g. MODIS), high resolution (up to 30m x 30m; e.g. Landsat TM), to very high resolution (up to 1m x 1m; e.g. Ikonos, QuickBird). In this approach NOAA-AVHRR data is used to classify the forest cover at a national scale, because after a careful inspection of the available data it was found that Landsat TM satellites (operating since the early 1980s) or MODIS (operating since 1999, Chuvieco and Huete 2009), do not cover the geographic boundary of continental Ecuador completely or historical data is not available, which also holds true for newer satellite types as Aster, RapidEye and QuickBird.

The NOAA-AVHRR resolution (1km x 1km) is lower compared to MODIS and Landsat TM images, but the data covers the whole continental Ecuador and historical data is available online (NOAA-CLASS 2015; <http://www.class.noaa.gov>). Furthermore, the coarse resolution of this satellite type fulfill the minimum requirements of the REDD+ initiative and reforestation programs conducted by MAE (2015), illustrating the forest cover of continental Ecuador in a 1km x 1km resolution. The data used here corresponds to the Local Area Coverage (LAC) format. The NOAA-AVHRR sensor provides data of

five spectral bands: one in the visible range (channel 1: 0.58-0.68 μ m), two in the near-infrared range (channel 2: 0.725-1.00 μ m; channel 3: 1.58-1.64 μ m (day), 3.55-3.93 μ m (night)), and two in the thermal infrared range (channel 4: 10.30-11.30 μ m; channel 5: 11.50-12.50 μ m). For the forest classification in the present study, channels 1, 2, and 5 were used.

For the calculation of total forest cover and annual deforestation rates in continental Ecuador over the periods 1986 – 2001 and 2001 – 2008 a set of NOAA-AVHRR satellite images of the years 1986, 2001 and 2008 are used. 1986 was selected as the base year because reference site data is available to validate the results (Papallacta, Bendix and Rafiqpoor 2001; fig. 2-1). Furthermore, total forest cover was estimated by Cabarle et al. (1989), respective to the years 1987/1988, which can be used as reference value. The same is valid for the year 2001 where reference site data is available, too (Estación Científica San Francisco – ECSF, Göttlicher et al. 2009; fig. 2-1), and a comparison to the official estimates presented in reports from MAE (2011 and 2012a) and FAO (2010b), respective to the year 2000, can be drawn. The raw data sets of 1986 and 2001 were downloaded from the NOAA-CLASS webpage (Comprehensive Large Array-data Stewardship System). The year 2008 was chosen because the REDD program in Ecuador started in 2008 (MAE 2015) and the calculated forest cover map provide basic data for this initiative. The raw data for the year 2008 was captured by the NOAA-AVHRR receiver station (coordinates: 3.986784 S, 79.198585 W) installed inside the campus of the Technical University of Loja/Ecuador (Universidad Técnica Particular de Loja, UTPL). The station, which consists of an antenna and a signal processor from Quorum Communications (2015), worked from 2007 to 2009 and raw data from all operating satellites could be received directly during this period. The receiver station location permitted a reception of the raw images in excellent satellite angles for vegetation classification at least two times a day. As Tucker et al. (2005) explained in their study, vegetation classification based on satellite images only is feasible if the viewing angle of the satellite is lower than 30°, because greater angles cause geometric distortions and blurring of pixels up to 2.4km x 6km.

2.3 Methods

To avoid miscalculations in the applied forest classification method, years with pronounced phenomena like ENSO or droughts, which cause short term variations in regional vegetation cover (under - or overestimation of the real forest cover), were not considered in this study. The same is valid for years of big volcanic eruptions (e.g. Mt. Pinatubo eruption in June of 1991), which bias forest classification by means of satellite data, because the dust in the atmosphere causes interference, wherefore the established thresholds for vegetation classification cannot be applied (Gutman et al. 1998).

The processing of the NOAA-AVHRR images to generate a forest classification for continental Ecuador can be divided in three parts (fig. 2-2).

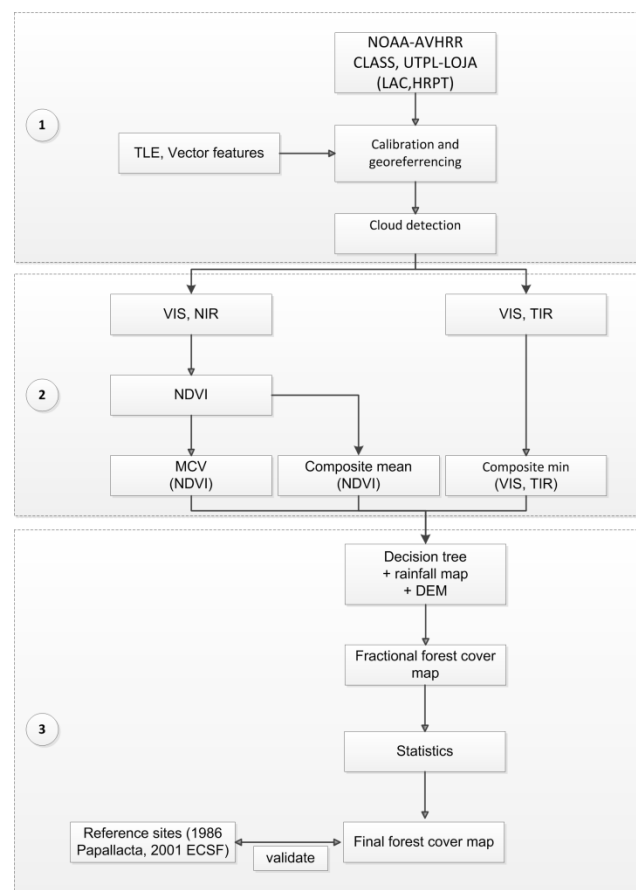


Figure 2-2: Processing scheme of the “forest” - “non-forest” classification.

The first step is the correction and calibration of the individual satellite raw images, including systematic corrections, geo-referencing, and cloud elimination. The radiometric corrections eliminate the atmospheric and solar radiation errors in the images (Roderick

et al. 1996), whereas specific parameters, suggested by Latifovic et al. (2012), are used. Then, the geometric correction is applied, implicating orbital parameters of each individual NOAA satellite, which are available online at the NOAA Class website, provided by the Advanced Earth Location Data System (AELDS). Next, a geo-referencing process is executed. A detailed description of the single steps can be found in Bachmann and Bendix (1992). During the geo-referencing process offsets from 4km to 6km frequently occur; hence, an additional adjustment has to be done. This further process is called “Image Matching” (e.g. Eugenio and Marquez 2003; Marcal and Borges 2003; Latifovic et al. 2005) and consists of auxiliary data from vector files, which distinguish and compare specific locations of main geographic features. The vector layer was generated by means of photointerpretation of Landsat Images in MrSID format from 1990 and 2000. The two vector layers compare the recognizable geographic features, such as the coast line, rivers, lakes, glaciers and/or city boundaries of the corrected NOAA images. If the position of these features is incorrect, each individual NOAA image is moved until it matches perfectly with the vector layers.

Hansen et al. (2002) exposed that special attention must be given to areas with clouds and cloud shadows because they alter the spectral values of the affected pixels as well as the pixels around these areas. As stated before, in Ecuador extremely high cloud frequency is present during the whole year (e.g. Bendix et al. 2006), which complicates any kind of satellite image product generation, especially at the escarpments of both cordilleras and at the Costal Lowland in the north (fig. 2-3a). The cloud detection scheme to eliminate the affected pixels is adopted from Bendix et al. (2004), which do not only determine cloud-filled pixels, but also classify the general cloud types (fig. 2-3b). For further information about the cloud classification please refer to Bendix et al. (2004). The result is a classified cloud mask, which is subtracted from the NOAA image. To avoid errors due to the cloud contour effect and cloud shadows a buffer of two pixels (= 2km) around each cloud field is also eliminated. Additionally, cloud shadows are identified by means of the solar angle and position during the satellite flyover and the affected areas subtracted. The result is a corrected and geo-referenced NOAA image, where all cloud contaminated pixels and shadows are removed.

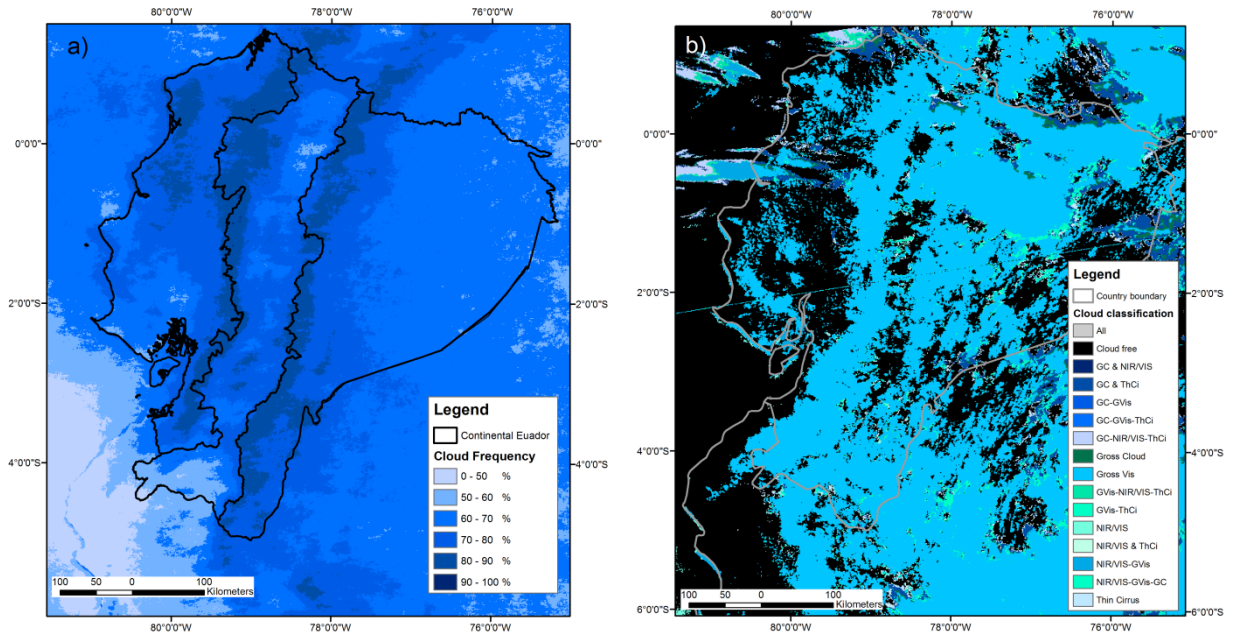


Figure 2-3: a) Annual cloud cover map of Ecuador (modified from Bendix et al. 2004)
b) Example of a cloud classification map.

The second step is the determination of the NDVI for all corrected NOAA images individually. The NDVI index is related to the photosynthetic capacity and hence to the energy absorption of the vegetation and is calculated as the ratio of channels 1 (VIS) and 2 (NIR) of the NOAA-AVHRR sensor (Fensholt et al. 2009):

$$NDVI = \frac{NIR - VIS}{NIR + VIS} \quad (1)$$

where NIR is the second NOAA-AVHRR channel (0.725-1.00 μ m) and VIS is the first NOAA-AVHRR channel (0.58-0.68 μ m).

To fill the cloud gaps in the individual NDVI maps a composite of several images has to be generated, using the Maximum Value Composite (MVC) method. The MVC consists of a multi-temporal composite of NDVI maps, where the maximum value for each pixel over a required time span is determined (Chen et al. 2003; Maisongrande et al. 2004). The MVC method also removes remaining clouds in the images, because clouds attenuate the spectral sensor values (Hansen et al. 2002). Generally, a temporal MVC composite of 10-days is created, but due to the high cloud frequency in Ecuador the temporal time span had to be extended to one month (e.g. Loveland et al. 2000; Los et al. 2002; Ma and Veroustraete 2006; Wang et al. 2014). Finally, all monthly composites are merged to annual NDVI maps for the years 1986, 2001 and 2008. However, even in the annual composites blank pixels remain, because in the images of the selected years clouds were

always present over some areas, especially at the escarpments of the cordilleras and over the northern Costal Lowland. An example of an annual NDVI composition (year 2001) is shown in figure 2-4.

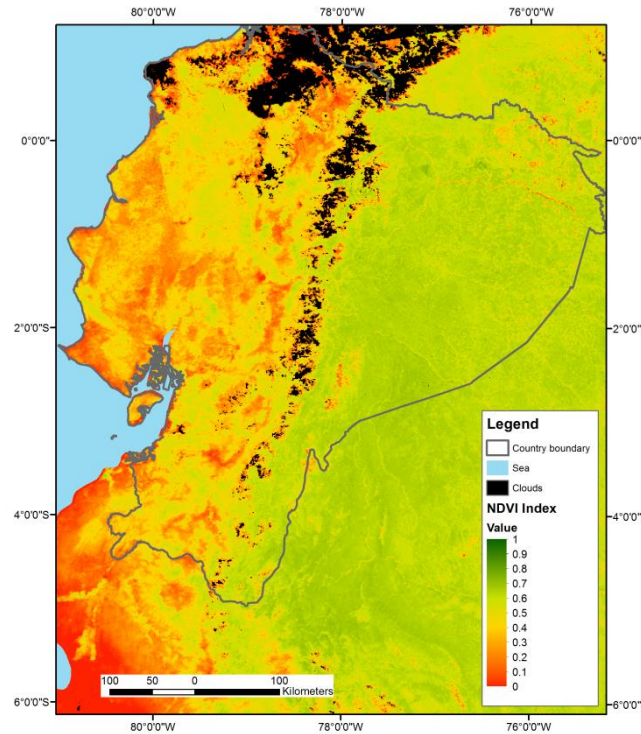


Figure 2-4: MVC composite of the annual NDVI (year 2001) with remaining clouds (black color).

Besides the MVC composites of the maximum NVDI maps, composites of the NOAA-AVHRR channels 1 and 5 are generated. These composition products are necessary for the decision tree to obtain the final forest classification (fig. 2-5). For channel 5 a composite of maximum values and for channel 1 a composite of minimum values are merged, in the same manner as explained before, and additionally a yearly composite of the mean values of the NDVI is generated.

The third step is the application of a decision tree to classify pixels with or without forest cover. Decision tree algorithms are widely used in forest classifications; because they represent a high overall accuracy (up to 90%; Lim et al. 1998; Hansen et al. 2000) and improve discriminations between different vegetation classes especially at coarse resolution (McIver and Friedl 2002). The decision tree algorithm (fig. 2-5) is adapted from Hansen et al. (2000) and automatized using the programming language “Fortran”.

In contrast to the original algorithm, where all five spectral bands of the NOAA-AVHRR sensor were used to classify different forest types, here only the composites of NDVI, channel 1 (VIS) and 5 (TIR) were included to detect “forest” respectively “non-forest” pixels. To improve the forest classification and to avoid false classification, additional topographic and meteorological data (precipitation and altitude) are also integrated in the decision tree algorithm (fig. 2-5).

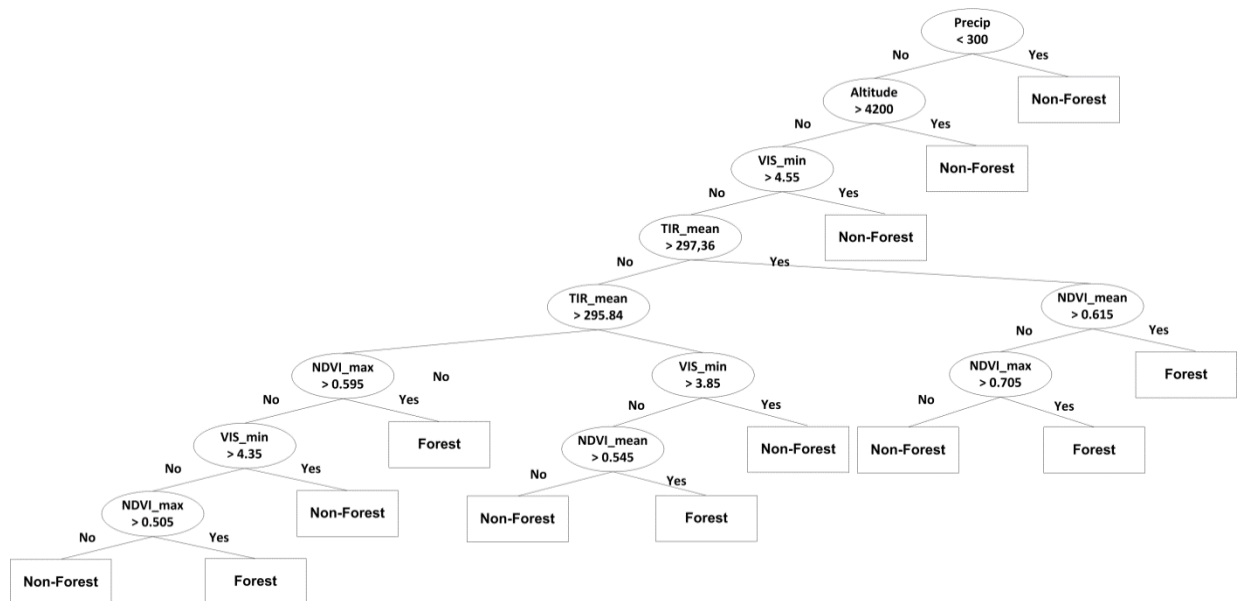


Figure 2-5: Decision tree algorithm of the “forest” – “non-forest” classification.

First an annual precipitation threshold was established, because forest vegetation needs at least 300mm of rainfall per year (Furley 2007). The annual precipitation map was obtained from the WorldClim database (Hijmans et al. 2005; <http://www.worldclim.org>), which has the same resolution as the NOAA images (1km x 1km). Each pixel within the satellite images is compared to the mean annual precipitation value in the WorldClim map (50 years average) and classified as “non-forest” if the threshold is not reached. Then, the remaining pixels are compared to the DEM (fig. 2-1), obtained from the SRTM (Farr et al. 2007), which was resampled to the satellite image resolution. Polylepis forest in the tropical Andes can be found in altitudes between 3600m and ~4200m (Cierjacks 2007), wherefore the tree-line threshold was set to 4200m asl and all pixels with higher elevation are flagged as “non-forest”. After this, the created composites of VIS, TIR and the NDVI are included in the decision tree (fig. 2-6). The respective thresholds of each

single step are taken from Hansen et al. (2000). The result is a forest cover map classified into “forest” and “non-forest” pixels for the years 1986, 2001 and 2008.

By means of the generated forest cover map the annual deforestation rates for the time span 1986 to 2001 and 2001 to 2008 are calculated. The annual rate of change can be estimated by comparing the forest cover in the same regions at two different times. According to Puyravaud (2003), the equation can be written as follows:

$$q = \left(\frac{A_2}{A_1} \right)^{1/(t_2-t_1)} - 1 \quad (2)$$

Where: A_1 y A_2 are the forest cover maps and t_1 and t_2 are the different time periods.

To avoid miscalculations of the annual deforestation rates per period (1986 – 2001; 2001 – 2008) the cloud contaminated pixels of both maps had to be merged (1986/2001; 2001/2008 respectively), because clouds cover different areas within each map. Then the merged cloud map is subtracted from both yearly forest classifications to guarantee the comparison of the same regions in the individual maps. Thereby, only pixels which could be classified within both years are taken into account for the calculation of the annual deforestation rate per period.

Finally, to validate the results available ancillary data (reference sites) from 1986 and 2001 are used to compare the generated forest cover map at the respective locations. The land cover at the reference site Papallacta (see fig. 2-1; year 1986) was classified using aerial photography by Bendix and Rafiqpoor (2001); the reference site ECSF (see fig. 2-1; year 2001) by Göttlicher et al. (2009) by means of Landsat satellite images. The reference site vegetation maps are taken as reliable for the respective year, because of the higher resolution of these data. Due to the different resolutions of the aerial photographs, the Landsat classification and NOAA-AVHRR satellite images, a reclassification was necessary. The original pixels with a resolution of 25m (aerial photography and Landsat) were aggregated into pixels of 1km (NOAA-AVHRR resolution). Then the percentage of forest cover of each aggregated pixel was calculated and declared as “forest” if more than 60% (threshold) are covered by forest stands (DeFries et al. 2000). By comparing the forest cover at the reference sites to the same areas in the generated yearly maps, the accuracy of our results is determined.

2.4 Results and discussion

The high cloud frequency over continental Ecuador during the whole year (Bendix et al. 2004) did not permit the creation of cloud free composites to calculate exactly the total forest cover and the annual deforestation rates per decade within the country. The generated forest cover maps always show areas of cloudiness (black color; see fig. 2-6a,b,c), therefore a definitive percentage of national forest cover could not be established. In the worst case clouds cover approximately 8.9% of the continental surface of Ecuador (year 2008; fig. 2-6c), which may increase the maximum inaccuracy of the generated maps and the error within the calculation of the annual deforestation rates. However, the final errors are not that pronounced, because clouded pixels mainly occur over areas where only small patches of possible forest can be expected (escarpments of the two cordilleras; see fig. 2-6), because most of these areas were previously deforested or the altitudinal threshold is exceeded (Cierjacks 2007; Mosandl et al. 2008).

The forest classification map for the year 1986 (fig. 2-6a) displays a total forest cover for continental Ecuador of ~11.9 million ha, which is equivalent to 48.1% of the land surface (tab. 1). The MAE report (2012a) published a value of about 12.9 million ha for the year 1990, using Landsat satellite images; and the FAO report (2010b), respectively to the year 1990, specifies a total forest cover of 13.8 million ha, equivalent to ~51.0% of the land surface. The higher amount of forested cover (between ~8.6% (MAE) and ~16.2% (FAO)) may be caused by cloud contaminated pixel, which are present in our calculated map (2.7%, more than 0.7 million ha). Supposing that all contaminated pixel are located over forest stands, our value is close to the MAE report (2012a), but this cannot be expected as fig. 2-6a indicates, because clouds occur mostly over the western cordillera where only small patch of mountain forest are located. The high FAO value is uncertain, as the report (2010a) specifies, due to the lack of information for this period and the applied interpolation method. However, Cabarle et al. (1989) also presented estimates of total forest cover for continental Ecuador for the period 1987-1988, indicating values between 43% and 50%, with a possible maximum forest cover of 13.6 million ha. The established range confirms our value of total forest cover of continental Ecuador at the end of the 1980s, although in our map cloud contaminated pixels are present.

Figure 2-6a illustrates that most of the Coastal Lowland and the Andean Highland are deforested, due to the intense deforestation phases during the last century and during the

Pre-Colombian-Era (e.g. Wunder 2000). The Coastal Lowland only show bigger patches of forest in the northern and the central parts, where protected areas were established (e.g. Reserva Ecológica, Manglares, Cayapas Mataje; Reserva Ecológica, Cotacachi Cayapas; Reserva Ecológica, Mache Chindul; Parque Nacional Machalilla; MAE 2012b). The Andean Highland forest basically covers uninhabited and/or steep valleys, whereas population pressure on the mountain ecosystems was still low during this period. In the extreme south, isolated patches of forest can be seen as well, indicating intact Dry Forest (west) and Tropical Mountain Forest (east) stands near the border of Peru. The Amazon Basin shows nearly a complete forest cover, except for the regions at the escarpment of the eastern cordillera and bigger areas in the southeast. These areas were deforested during the oil-boom, especially the northern and central parts, and with the beginning of the big scale mining industry in the southern part, during the 1970s (Bonan 2008). Inside the forest, along the big river systems, “non-forest” pixels are displayed, too, which is not only caused by the timber extraction, but also due to the existing water surfaces (see fig. 2-1).

Figure 2-6b shows the forest classification for the year 2001. Forest covers 10.4 million ha (~42.0%, tab. 2-1) of continental Ecuador. The MAE report (2012a) specifies a value of 11.8 million ha for the year 2000, the same value is reported by the FAO (2010b). These results, compared to our study, indicate a higher forest cover of continental Ecuador of about 1.6 million ha (~13.5%). This may be due to the high number of cloud affected pixels in our generated forest cover map (5.3%, more than 1.3 million ha; tab.2-1). However, an earlier MAE report (2011) specifies lower values of total forest cover in continental Ecuador between 10.5 million ha (MAE) and 11.6 million ha (CLIRSEN = Centro de Levantamientos Integrados de Recursos Naturales por Sensores Remotos del Ecuador) for the year 2000.

Compared to the year 1986 (fig. 2-6a) a reduction in forest cover of 12.7% could be stated (see tab. 2-1). Forested areas were considerably reduced in the whole country during the end of the last century, but especially at the Coastal Lowland and in the Andean Highland (see: Supplement 2A), where forest was replaced by pastures and agricultural land (e.g. Mosandl et al. 2008). At the Coastal Lowland deforestation took place even in the protected areas to the north and the central parts, only the core areas still show bigger patches of connected forests. Big parts of the Dry Forest in the south of the Andean Highland as well as most of the Tropical Mountain Forest in the Andean valleys got lost,

too, due to the enhanced population pressure (Ochoa et al. 2015). The Amazonian Basin also displays an increase of deforested areas, especially in the south-east near the border with Peru, mainly caused by the intense mining industry. Along the streams a reduction is visible, too, which is due to uncontrolled timber extraction near the bigger rivers.

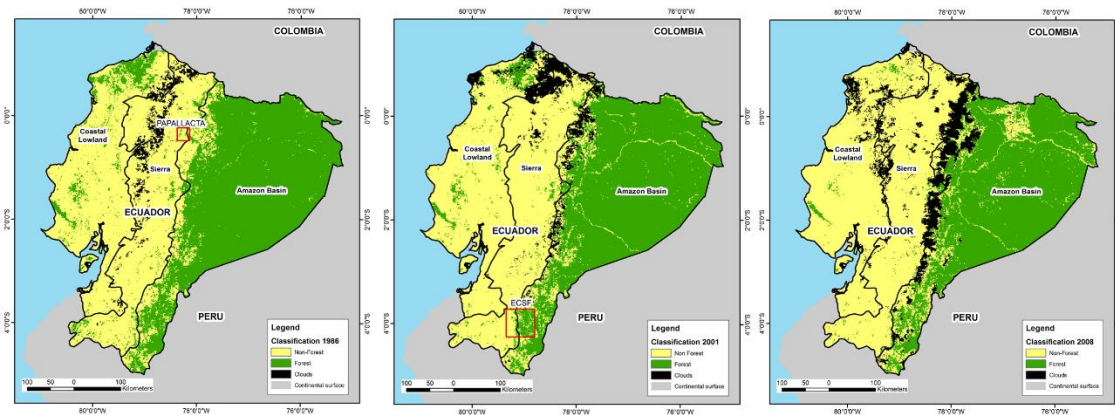


Figure 2-6: Forest classification of the year a) 1986 (with reference site), b) 2001 (with reference site) and c) 2008.

The calculated annual deforestation rate for the period 1986 to 2001 is $\sim -0.9\%$ (tab. 2-1), considering only areas which could be classified at both years (subtraction of the merged cloud mask). The FAO (2010a,b) published a notably higher deforestation rate for the period 1990-2000 (-1.5%). The difference may be caused by the high amount of cloud covered pixels in our map, especially over the northern Coastal Lowland. However, as explained above the published deforestation rate for Ecuador in the FAO reports (2010a,b) for the decade 1990 to 2000 is uncertain and MAE (2012a) indicates a value of -0.7% for the same period.

Figure 2-6c displays the forest classification map for 2008. Forest covers 9.1 million ha of the land surface, which compared to the year 1986 is a reduction in forest cover of 23.7% (tab. 2-1) and to the year 2001 of 12.6%. The FAO reports (2010b) specify a total forest cover for continental Ecuador of ~ 9.9 million ha for the year 2010, which means a reduction of 28.3% compared to the year 1990. In contrast, MAE (2012a) published a value of 11.3 million ha for the year 2008. Again, the difference in forest cover may be due to the high number of clouded pixels in our map (8.9%, more than 2.2 million ha; tab. 2-1).

Deforestation continued during the last decade in the whole country not only at the Coastal Lowland and the Andean Highland, but also in the Amazon Basin (fig. 2-6c). At the Coastal Lowland most of the forest stands are cleared to create agricultural land, due to the enhanced population pressure. Only in the core parts of major protected areas patches of dense forest still remain. The same scenario can be observed in the Andean Highland, where the forest is almost replaced completely to create pasture land (e.g. Mosandl et al. 2008; Ochoa et al. 2015). The most obvious reduction of forest cover is displayed in the north of the Amazon Basin, where oil companies expanded their production, while the expansion of the mining industry took place in the southeast (see: Supplement 2A). Furthermore, small patches of several deforested areas inside the Tropical Lowland Forest are visible, which is mainly caused by illegal timber extraction (Bonan 2008). But now, the clearance of the forest is not only shown near the bigger river systems but also in parts of difficult accessibility.

The calculated annual deforestation rate is -1.9% (tab. 2-1), respectively to the period 2001 to 2008. FAO (2010b) specifies the same value, while the MAE report (2012a) a notable lower value of -0.7%. The low annual deforestation rate published by MAE (2012a) seems to be underestimated, because other studies also confirm the increase of the deforestation rate in continental Ecuador during the last decade (e.g. Mosandl et al. 2008; Tapia et al. 2015).

The forest classification of continental Ecuador was validated by means of the generated maps for 1986 and 2001, and data from two independent study sites. For 1986 a photointerpretation product for a small area in northern Ecuador (Papallacta at 4800m asl; Bendix and Rafiqpoor 2001; fig. 2-7) is available and for 2001 a Landsat TM classification for an area in southern Ecuador (ECSF at 1850m asl; Göttlicher et al. 2009; fig. 2-8). First, both independent data sets were resampled to the same spatial resolution as the NOAA-AVHRR images (1km x 1km) and reclassified in “forest” and “non-forest” pixels. To classify a pixel as “forest” at least 60% of it must be covered by forest stands (threshold; DeFries et al. 2000). Then, the respective areas in our maps were subtracted and finally, the areas compared using the “Cross-Tabulation” application in the Idrisi-Taiga software package (IDRISI 2011; Clark Labs 2015). For the year 2001 additionally a cloud mask was generated, because the composite shows some cloud contaminated pixels within the reference site. The cloud mask was subtracted from both maps (reference site and composite) to ensure the comparison of the same areas (see fig. 2-8)

Table 2-1: Results of the comparison between reference sites and the new classification approach. The mean values show the percentage of forest present in class of forest/non-forest.

Year	Land cover	Total land surface [ha]	Forest cover [%]	Cloud cover [%]	Forest cover reduction in relation to 1986 [%]	Annual rates of deforestation [%]
1986	Non Forest	12132500				
	Forest	11871700	48.1		0.0	
	Clouds	654800		2.7		
	Total Area	24659000				
1986 - 2001						
2001	Non Forest	12975600				
	Forest	10368500	42.0		12.7	-0.9
	Clouds	1314900		5.3		
	Total Area	24659000				
2001 - 2008						
2008	Non Forest	13393800				
	Forest	9062800	36.8		23.7	-1.9
	Clouds	2202400		8.9		
	Total Area	24659000				

The validation for the composite of 1986 (fig. 2-7) produced a good accuracy with a Cramer's value of 0.704 and an overall Kappa value of 0.702 (see tab. 2-2). The discrepancies may be explained by the resampling technique applied to the photointerpretation map of 1986, the established forest threshold (60%) and/or the different classification methods. However, Hansen et al. (2000) obtained a similar agreement between 65% and 82% for their forest classification map, compared to different training sites. Also MAE (2012a) specified an equivalent overall Kappa value of about 0.7 for their classification, using Landsat satellite images.

Also for the composite of 2001 (fig. 2-8) a good accuracy was obtained with a Cramer value of 0.730 and an overall Kappa value of 0.720 (see tab. 2-2). The MAE report (2012a) stated the same accuracy for the year 2000 as for the year 1990 (overall Kappa

0.7) for their classification. Unfortunately, the FAO report (2010b) does not specify the accuracy of their maps; it only indicates that the errors are higher for 1990 due to the poor information compared to the year 2010.

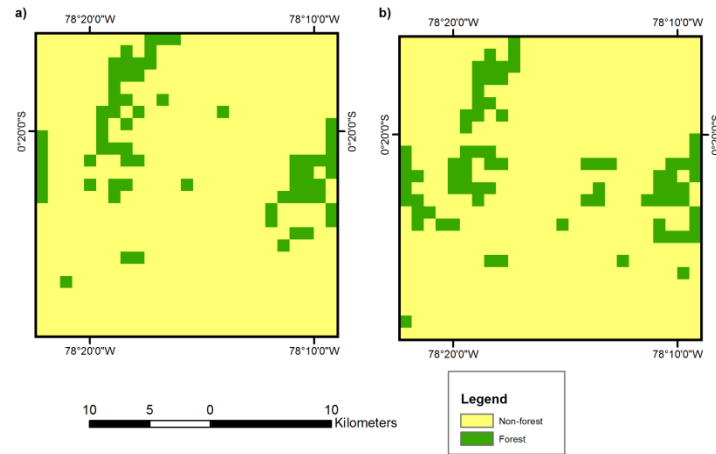


Figure 2-7: Forest classification at Papallacta for 1986 a) Reference site (adapted from Bendix and Rafiqpoor 2001), b) Classified NOAA-AVHRR image.

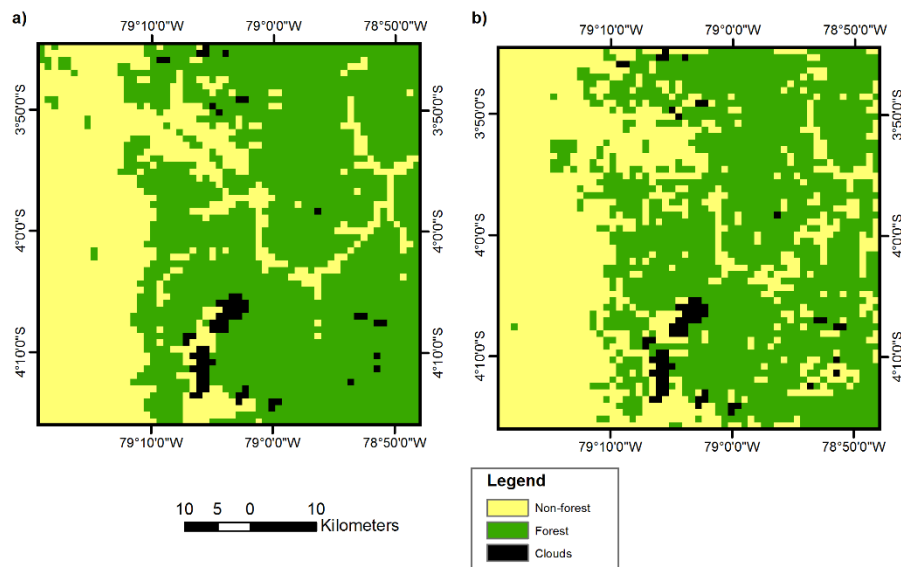


Figure 2-8: Forest Classification at ECSF for 2001 a) Reference site (adapted from Göttlicher et al. 2009), b) Classified NOAA-AVHRR image

Table 2-2: Accuracy between “forest” and “non-forest” pixel of the reference sites (rows); a) Papallacta 1986; b) ECSF 2001) and the generated forest cover maps (columns).

Cramer's value		Non-forest	Forest	Total	User's Accuracy	Commission's error
Papallacta	Non-Forest	0.8544	0.0384	0.8928	95.69	4.31
	Forest	0.0224	0.0848	0.1072	79.1	20.9
	Total	0.08768	0.1232	1		
	Producer's Accuracy	97.44	68.83			
	Omission's error	2.56	31.67			
	Overall Accuracy	0.9392				
Cramer's value		0.7041				
Overall Kappa		0.7019				
b		Non-forest	Forest	Total	User's Accuracy	Commission's error
Loja	Non-Forest	0.3513	0.0291	0.3805	92.34	7.66
	Forest	0.108	0.5115	0.6195	82.56	17.44
	Total	0.4593	0.5407	1		
	Producer's Accuracy	76.48	94.61			
	Omission's error	23.52	5.39			
	Overall Accuracy	0.8628				
Cramer's value		0.7298				
Overall Kappa		0.7203				

2.5 Conclusions

The methodology used for forest classification of continental Ecuador, including cloud detection and subtraction, the generation of the annual composites and the application of a decision tree algorithm provides a practical approach to estimate forest cover at a national scale. Compared to other studies and methods the accuracies of the generated

maps were determined to be within the same range (FAO 2010b; MAE 2012a), which confirms the reliability of the present approach.

The focus of the present investigation was to calculate the total forest cover and annual deforestation rates per period for continental Ecuador. Unfortunately, clouds were always present over some areas during the selected years and an exact percentage of national forest cover could not be established. However, using composites of one year a lot of the clouded pixels could be eliminated and the additional integration of topographic and meteorological parameters (precipitation and altitude) in the decision tree improved the forest classification.

The study has shown that forest cover in continental Ecuador was clearly reduced during the observation period (from 48.1% in 1986 to 36.8% in 2008; tab. 2-1). A definitive value of existing forest stand could not be established due to the cloud contamination in the individual maps. Nevertheless, the calculated total forest cover is close to the values presented in other studies (Cabarle et al. 1989, year 1986; MAE 2011, year 2001; FAO 2010b, year 2008). Forest reduction is especially obvious in the Coastal Lowland where only in the core zones of protected areas dense forest stands still remain. In this region deforestation is mainly caused by the enhanced population pressure. The Amazon Basin shows a notable reduction in forest cover as well, mostly resulting from the expansion of the oil and mining industry but also from the illegal timber extraction. The Andean forest stands display lesser deforestation, because most of the mountain forest was cleared during the Pre-Columbian-Era (Mosandl et al. 2008). Highest forest reduction can be stated for the eastern cordillera, as confirmed by MAE (2012a), due to the ongoing mining industry (fig. 2-6).

It was also found that annual deforestation rates have increased with the beginning of the new century (-0.9%, period 1986-2001; -1.9%, period 2001-2008; see tab. 2-1), which is confirmed by the FAO report (2010b) and other studies (Mosandl et al. 2008; Tapia et al. 2015). Although a definitive value could not be established due to the cloud contamination in the individual maps and the inaccuracies of the generated composites (Kappa-value: 0.7; tab. 2-2), the obtained results are close to MAE (2012a), respective to the period 1990 – 2000, and the FAO report (2010b), respective to the period 2000 – 2010.

To promote reforestation, the national government of Ecuador started a restoration program and identified 1.6 million ha of possible forest restoration (MAE 2014). The

generated forest cover maps depict the remaining forest stands and can help to expedite the reforestation program. The maps also are important for the REDD initiative driven by the Ecuadorian government since 2008, because forests are important stocks and sinks for carbon and other greenhouse gases.

To improve the results, future works should generate composites of several years to obtain cloud free forest cover maps of continental Ecuador. Also, additional topographic and meteorological parameters (e.g. landslide and temperature maps) can be integrated to avoid false calculations during the classification process. By means of these maps, total forest cover, annual deforestation rates and possible forest restoration area can be detected more adequately.

Acknowledgment

This study was executed in framework with the DFG Research Unit 816: Biodiversity and Sustainable Management of Mega-diverse Mountain Ecosystems in South Ecuador. Thanks to the members of the Laboratory of Climatology and Remote Sensing (LCRS) in Marburg for their support. Special thanks go to the Universidad Técnica Particular de Loja (UTPL) to facilitate this research.

2.6 References

- Aguiar, A. P. D.; Ometto, J. P.; Nobre, C.; Lapola, D. M.; Almeida, C.; Vieira, I. C.; Soares, J. V.; Alvala, R.; Saatchi, S.; Valeriano, D. and Castilla-Rubio, J. C. (2012): Modeling the spatial and temporal heterogeneity of deforestation-driven carbon emissions: the INPE-EM framework applied to the Brazilian Amazon. In: *Global Change Biology* 18, 3346–3366. DOI: 10.1111/j.1365-2486.2012.02782.x
- Bachmann, M. and Bendix, J. (1992): An improved algorithm for NOAA-AVHRR image referencing. In: *International Journal of Remote Sensing* 13, 3205–3215. DOI: 10.1080/01431169208904111
- Barthlott, W.; Mutke, J.; Rafiqpoor, M. D.; Kier, G. and Kreft, H. (2005): Global centers of vascular plant diversity. In: *Nova Acta Leopoldina NF* 92, 61–83.
- Barthlott, W.; Hostert, A.; Kier, G.; Küper, W.; Kreft, H.; Mutke, J.; Rafiqpoor, M. D. and Sommer, J. H. (2007): Geographic patterns of vascular plant diversity at continental to global scales. In: *Erdkunde* 61, 305–315. DOI: 10.3112/erdkunde.2007.04.01
- Beck, E.; Makeschin, F.; Haubrich, F.; Richter, M.; Bendix, J. and Valarezo, C. (2008): The Ecosystem (Reserva Biológica San Francisco). In: Beck, E.; Bendix, J.; Kottke, I.; Makeschin, F. and Mosandl, R. (eds.): *Gradients in a tropical mountain ecosystem of Ecuador*. Berlin, Heidelberg, 1–13. DOI: 10.1007/978-3-540-73526-7_1
- Bendix, J. and Rafiqpoor, M. D. (2001): Studies on the thermal conditions of soils at the upper tree line in the Páramo of Papallacta (Eastern Cordillera of Ecuador). In: *Erdkunde* 55, 257–276. DOI: 10.3112/erdkunde.2001.03.04
- Bendix, J.; Rollenbeck, R. and Palacios, E. (2004): Cloud detection in the Tropics - a suitable tool for climate-ecological studies in the high mountains of Ecuador. In: *International Journal of Remote Sensing* 25, 4521–4540. DOI: 10.1080/01431160410001709967
- Bendix, J.; Rollenbeck, R.; Göttlicher, D. and Cermak, J. (2006): Cloud occurrence and cloud properties in Ecuador. In: *Inter-Research Climate Research* 30, 133–147. DOI: 10.3354/cr030133
- Bendix, J.; Rollenbeck, R.; Richter, M.; Fabian, P. and Emck, P. (2008): Climate. In: Beck, E.; Bendix, J.; Kottke, I.; Makeschin, F. and Mosandl, R. (eds.): *Gradients in a tropical mountain ecosystem of Ecuador*. Berlin, Heidelberg, 63–73.
- Bonan, G. B. (2008): Forests and climate change: Forcings, feedbacks, and the climate benefits of forests. In: *Science* 320, 1444–1449. DOI: 10.1126/science.1155121

- Brehm, G.; Homeier, J.; Fiedler, K.; Kottke, I.; Illig, J.; Nöske, N. M.; Werner, F. a. and Breckle, S.-W. (2008): Mountain rain forests in southern Ecuador as a hotspot of biodiversity – limited knowledge and diverging patterns. In: Beck, E.; Bendix, J.; Kottke, I.; Makeschin, F. and Mosandl, R. (eds.): Gradients in a tropical mountain ecosystem of Ecuador. Berlin, Heidelberg, 15–24. DOI: 10.1007/978-3-540-73526-7_2
- Breuer, L.; Windhorst, D.; Fries, A. and Wilcke, W. (2013): Supporting, regulation, and provisioning hydrological services. In: Bendix, J.; Beck, E.; Bräuning, A.; Makeschin, F.; Mosandl, R.; Scheu, S. and Wilcke, W. (eds.): Ecosystem services, biodiversity and environmental change in a tropical mountain ecosystem of south Ecuador. Berlin, Heidelberg, 107–116. DOI: 10.1007/978-3-642-38137-9_9
- Clark Labs (2015): Geospatial software for monitoring and modeling the Earth system. <http://www.clarklabs.org/> (Date: 25.06.2015).
- Cabarle, B. J.; Crespi, M.; Dodson, C. H.; Luzuriaga, C.; Rose, D. and Shores, J. N. (1989): An assessment of biological diversity and tropical forests for Ecuador. USAID, Quito.
- Cierjacks, A. (2007): Environmental and human influences on tropical treeline formation: insights from the regeneration ecology of *Polylepis* spp. in the Páramo de Papallacta, Ecuador. ULB Sachsen-Anhalt. Karlsruhe.
- Chuvieco, E. and Huete, A. (2009): Fundamentals of satellite remote sensing. CRC Press. Boca Raton.
- Chen, P. -Y.; Srinivasan, R.; Fedosejevs, G. and Kiniry, J.R. (2003): Evaluating different NDVI composite techniques using NOAA-14 AVHRR data. In: International Journal of Remote Sensing 24, 3403–3412. DOI: 10.1080/0143116021000021279
- DeFries, R. S.; Hansen, M. C.; Townshend, J. R. G.; Janetos, A. C. and Loveland, T. R. (2000): A new global 1-km dataset of percentage tree cover derived from remote sensing. In: Global Change Biology 6, 247–254. DOI: 10.1046/j.1365-2486.2000.00296.x
- Dierl, K.-H. (2010): Pflanzendiversität entlang eines Höhengradienten in den Anden Südecuadors. Universität Erlangen-Nuremberg.
- Eastman, J. R.; Sangermano, F.; Machado, E. A.; Rogan, J. and Anyamba, A. (2013): Global trends in seasonality of Normalized Difference Vegetation Index (NDVI), 1982–2011. In: Remote Sensing 5, 4799–4818. DOI: 10.3390/rs5104799
- Eugenio, F. and Marques, F. (2003): Automatic satellite image georeferencing using a contour-matching approach. In: IEEE Transactions on Geosciences and Remote Sensing 41, 2869–2880. DOI: 10.1109/TGRS.2003.817226

- FAO (Food and Agriculture Organization of the United Nations) (2010a): Evaluación de recursos forestales mundiales 2010 – Informe principal. Roma.
- FAO (Food and Agriculture Organization of the United Nations) (2010b): Evaluación de los recursos forestales mundiales 2010 – Informe Nacional Ecuador. Roma.
- Farr, T. G.; Rosen, P. A.; Caro, E.; Crippen, R.; Duren, R.; Hensley, S.; Kobrick, M.; Paller, M.; Rodriguez, E.; Roth, L.; Seal, D.; Shaffer, S.; Shimada, J.; Umland, J.; Werner, M.; Oskin, M.; Burbank, D. and Alsdorf, D. (2007): The Shuttle Radar Topography Mission. In: Reviews of Geophysics 45. DOI: 10.1029/2005RG000183
- Fensholt, R.; Rasmussen, K.; Nielsen, T. T. and Mbow, C. (2009): Evaluation of earth observation based long term vegetation trends - Intercomparing NDVI time series trend analysis consistency of Sahel from AVHRR GIMMS, Terra MODIS and SPOT VGT data. In: Remote Sensing of Environment 113, 1886–1898. DOI: 10.1016/j.rse.2009.04.004
- Fries, A.; Rollenbeck, R.; Göttlicher, D.; Nauß, T.; Homeier, J.; Peters, T. and Bendix, J. (2009): Thermal structure of a megadiverse Andean mountain ecosystem in southern Ecuador and its regionalization. In: Erdkunde 4, 321–335. DOI: 10.3112/erdkunde.2009.04.03
- Fries, A.; Rollenbeck, R.; Nauß, T.; Peters, T. and Bendix, J. (2012): Near surface air humidity in a megadiverse Andean mountain ecosystem of southern Ecuador and its regionalization. In: Agricultural and Forest Meteorology 152, 17–30. DOI: 10.1016/j.agrformet.2011.08.004
- Fuller, D.-O. (2006): Tropical forest monitoring and remote sensing: A new era of transparency in forest governance?. In: Singapore Journal of Tropical Geography 27, 15–29. DOI: 10.1111/j.1467-9493.2006.00237.x
- Furley, P. A. (2007): Tropical forest of the lowlands. In: Veblen, T.; YOUNG, K.; Orme, A. (eds.): The physical geography of South America. Oxford University Press, New York, 135–157.
- Gilbert, N. (2012): One third of our greenhouse gas emissions come from agriculture. In: Nature News & Comment. DOI:10.1038/nature.2012.11708.
- Global Forest Watch (2015): Global Forest Watch. <http://www.globalforestwatch.org/> (Date: 02.10.2015)
- Göttlicher, D.; Obregon, A.; Homeier, J.; Rollenbeck, R.; Nauss, T. and Bendix, J. (2009): Land-cover classification in the Andes of southern Ecuador using LandsatETM+ data as a basic for SVAT modelling. In: International Journal of Remote Sensing 30, 1867–1886. DOI: 10.1080/01431160802541531

- Gutman, G.; Tarpley, D.; Ignatov, A. and Olson, S. (1998): Global AVHRR products for land climate studies. In: *Advances in Space Research* 22, 1591–1594. DOI: 10.1016/S0273-1177(99)00118-0
- Hansen, M. C.; DeFries, R. S.; Townshend, J. R. G. and Sohlberg, R. (2000): Global land cover classification at 1 km spatial resolution using a classification tree approach. In: *International Journal Remote Sensing* 21, 1331–1364. DOI: 10.1080/014311600210209
- Hansen, M. C.; DeFries, R. S.; Townshend, J. R. G.; Marufu, L. and Sohlberg, R. (2002): Development of a MODIS tree cover validation data set for Western Province, Zambia. In: *Remote Sensing of Environment* 83, 320–335.
- Hijmans, R.; Cameron, S. E.; Parra, J. L.; Jones, P. G. and Jarvis, A. (2005): Very high resolution interpolated climate surfaces for global land areas. In: *International Journal of Climatology* 25, 1965–1978. DOI: 10.1002/joc.1276
- Homeier, J.; Werner, F. A.; Gradstein, S. R.; Breckle, S. W. and Richter, M. (2008): Potential vegetation and floristic composition of Andean forests in South Ecuador, with a focus on the RBSF. Mountain rain forests in southern Ecuador as a hotspot of biodiversity – limited knowledge and diverging patterns. In: Beck, E.; Bendix, J.; Kottke, I.; Makeschin, F. and Mosandl, R. (Eds.): *Gradients in a Tropical Mountain Ecosystem of Ecuador*. Berlin, Heidelberg, 87–100. DOI: 10.1007/978-3-540-73526-7_10
- IDRISI (2011): *Manual Version 16*. Clark University. Worcester.
- IPCC (Intergovernmental Panel on Climate Change) (2013): Working Group I Contribution to the IPCC fifth assessment report climate change 2013: The Physical Science Basics. IPCC, Stockholm.
- Latifovic, R.; Trishchenko, A. P.; Chen, J.; Park, W. B.; Khlopenkov, K. V.; Fernandes, R.; Pouliot, D.; Ungureanu, C.; Luo, Y.; Wang, S.; Davidson, A. and Cihlar, J. (2005): Generating historical AVHRR 1 km baseline satellite data records over Canada suitable for climate change studies. In: *Canadian Journal of Remote Sensing* 31, 324–346. DOI: 10.5589/m05-024
- Latifovic, R.; Pouliot, D. and Dillabaugh, C. (2012): Identification and correction of systematic error in NOAA AVHRR long-term satellite data record. In: *Remote Sensing of Environment* 127, 84–97. DOI: 10.1016/j.rse.2012.08.032
- Lim, T.; Loh, W. and Shih, Y. (1998): An empirical comparison of decision trees and other classification methods. In: *Madison technical report 979*. Department of Statistics – University of Wisconsin.

- Los, S.O.; Tucker, C. J.; Anyamba, A.; Cherlet, M.; Collatz, G. J.; Giglio, L.; Hall, F. G. and Kendall, J. A. (2002): The biosphere: a global perspective. In: Andrew Skidmore (ed.): Environmental modelling with GIS and remote sensing. CRC Press, 70–96. DOI: 10.1201/9780203302217.ch5
- Loveland, T.R.; Reed, B. C.; Brown, J. F.; Ohlen, D. O.; Zhu, Z.; Yang, L. and Merchant, J. W. (2000): Development of a global land cover characteristics database and IGBP DISCover from 1 km AVHRR data. In: International Journal of Remote Sensing 21, 1303–1330. DOI: 10.1080/014311600210191
- Ma, M. and Veroustraete, F. (2006): Reconstructing pathfinder AVHRR land NDVI time-series data for the Northwest of China. In: Advances in Space Research 37, 835–840. DOI: 10.1016/j.asr.2005.08.037
- Maisongrande, P.; Duchemin, B. and Dedieu, G. (2004): VEGETATION/SPOT: an operational mission for the Earth monitoring; presentation of new standard products. In: International Journal of Remote Sensing 25, 9–14. DOI: 10.1080/0143116031000115265
- MAE (Ministerio del Ambiente | Ecuador) (2011): Estimación de la Tasa de Deforestación del Ecuador Continental. Quito. <http://simce.ambiente.gob.ec/sites/default/files/documentos/geovanna/Estimaci%C3%B3n%20de%20la%20Tasa%20de%20Deforestaci%C3%B3n%20del%20Ecuador%20Continental.pdf> (Date: 25.06.2015)
- MAE (Ministerio del Ambiente | Ecuador) (2012a): Línea base de deforestación del Ecuador Continental. Quito. <http://sociobosque.ambiente.gob.ec/files/Folleto%20mapa-parte1.pdf> (Date: 25.06.2015)
- MAE. (Ministerio del Ambiente | Ecuador) (2012b): Sistema Nacional de áreas protegidas del Ecuador. Quito. http://www.ambiente.gob.ec/wp-content/uploads/downloads/2012/10/SNAP_19_09_12.pdf (Date: 25.06.2015)
- MAE. (Ministerio del Ambiente | Ecuador) (2014): Plan nacional de Restauración Forestal 2014 – 2017. Quito. <http://sociobosque.ambiente.gob.ec/files/images/articulos/archivos/amrPlanRF.pdf> (Date: 25.06.2015)
- MAE. (Ministerio del Ambiente | Ecuador) (2015): Cambio climático una estrategia transversal de desarrollo. <http://www.ambiente.gob.ec/cambio-climatico-una-estrategia-transversal-de-desarrollo/> (Date: 24.06.2015)

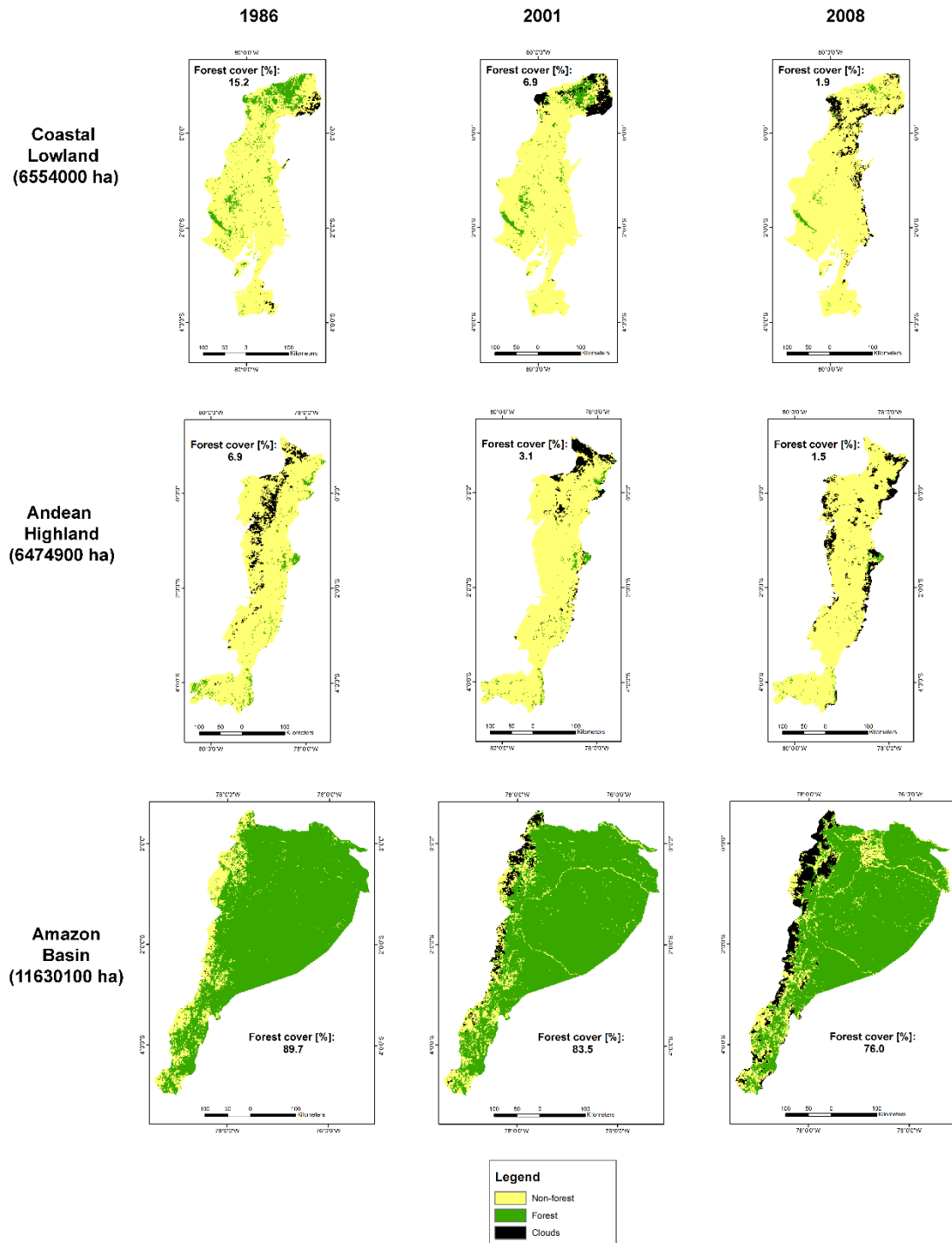
- Marcal, A. R. S. and Borges, J. (2003): AVHRR rectification using orbital navigation and image matching. In: *Image and Signal Processing for Remote Sensing VIII*, 13–21. DOI: 10.1117/12.463515
- McIver, D. K. and Friedl, M. A. (2002): Using prior probabilities in decision-tree classification of remotely sensed data. In: *Remote Sensing of Environment* 81, 253–261. DOI: 10.1016/S0034-4257(02)00003-2
- Moraes, E. C.; Franchito, S. and Rao, B. (2013): Amazonian Deforestation: Impact of global warming on the energy balance and climate. In: *Journal of Applied Meteorology and Climatology* 52, 521–530. DOI: <http://dx.doi.org/10.1175/JAMC-D-11-0258.1>
- Mosandl, R.; Günter, S.; Stimm, B. and Weber, M. (2008): Ecuador suffers the highest deforestation rate in South America. In: Beck, E.; Bendix, J.; Kottke, I.; Makeschin, F. and Mosandl, R. (eds.): *Gradients in a tropical mountain ecosystem of Ecuador*. Berlin, Heidelberg, 37–40. DOI: 10.1007/978-3-540-73526-7_4
- Myers, N.; Mittermeier, R. A.; Mittermeier, R. A.; Mittermeier, C. G.; da Fonseca, G. A. B. and Kent, J. (2000): Biodiversity hotspots for conservation priorities. In: *Nature* 403, 853–858. DOI: 10.1038/35002501
- NASA (National Aeronautics and Space Administration) (2005): Shuttle Radar Topography Mission – Imágenes SRTM de América del Sur. http://www2.jpl.nasa.gov/srtm/southAmerica_sp.htm (Date: 25.06.2015).
- NOAA-CLASS (2015): NOAA's Comprehensive Large Array-data Stewardship System (CLASS). <http://www.class.noaa.gov> (Date: 25.06.2015).
- Nonomura, A.; Sanga-Ngoie, K. and Fukuyama, K. (2003): Devising a new digital vegetation model for eco-climatic analysis in Africa using GIS and NOAA AVHRR data. In: *International Journal of Remote Sensing* 24, 3611–3633. DOI: 10.1080/0143116021000053779
- Olander, L. P.; Gibbs, H. K.; Steininger, M.; Swenson, J. J. and Murray, B. C. (2008): Reference scenarios for deforestation and forest degradation in support of REDD: a review of data and methods. In: *Environmental Research Letters* 3 025011. DOI: dx.doi.org/10.1088/1748-9326/3/2/025011
- Ochoa-Cueva, P.; Fries, A.; Montesinos, P.; Rodríguez-Díaz, J. A. and Boll, J. (2015): Spatial estimation of soil erosion risk by land-cover change in the Andes of Southern Ecuador. In: *Land Degradation & Development* 26, 565–573. DOI: 10.1002/ldr.2219
- Poulter, B.; Hattermann, F.; Hawkins, E.D.; Zaehle, S.; Sitch, S.; Restrepo-Coupe, N.; Heyder, U. and Cramer, W. (2010): Robust dynamics of Amazon dieback to climate

- change with perturbed ecosystem model parameters. In: *Global Change Biology* 16, 2476–2495. DOI: 10.1111/j.1365-2486.2009.02157.x
- Puyravaud, J. P. (2003): Standardizing the calculation of the annual rate of deforestation. In: *Forest Ecology and Management* 177, 593–596. DOI: 10.1016/S0378-1127(02)00335-3
- Quorum Communications (2015): Satellite Remote Sensing Systems & Electronics. <http://www.qcom.com/> (Date: 20.05.2015)
- Richter, M. (2003): Using epiphytes and soil temperatures for eco-climatic interpretations in southern Ecuador. In: *Erdkunde* 57, 161–181. DOI: 10.3112/erdkunde.2003.03.01
- Roderick, M.; Smith, R. and Lodwick, G. (1996): Calibrating long-term AVHRR-derived NDVI imagery. In: *Remote Sensing of Environment* 58, 1–12. DOI: 10.1016/0034-4257(96)00035-1
- Saatchi, S. S.; Harris, N. L.; Brown, S.; Lefsky, M.; Mitchard, E.; Salas, W.; Zutta, B. R.; Buermann, W.; Lewis, S. L.; Hagen, S.; Petrova, S.; White, L. and Morel, A. (2011): Benchmark map of forest carbon stocks in tropical regions across three continents. In: *Proceedings of the National Academy of Science of the United States of America* 108, 9899–9904. DOI: 10.1073/pnas.1019576108
- Simic, A.; Fernandes, R.; Brown, R.; Romanov, P. and Park, W. (2004): Validation of VEGETATION, MODIS, and GOES + SSM/I snow-cover products over Canada based on surface snow depth observations. In: *Hydrological Processes* 18, 1089–1104. DOI: 10.1002/hyp.5509
- Tan, K.; Piao, S.; Peng, C. and Fang, J. (2007): Satellite-based estimation of biomass carbon stocks for northeast China's forests between 1982 and 1999. In: *Forest Ecology and Management* 240, 114–121. DOI: 10.1016/j.foreco.2006.12.018
- Tapia-Armijos, M. F.; Homeier, J.; Espinosa, C. I.; Leuschner, C. and de la Cruz, M. (2015): Deforestation and forest fragmentation in South Ecuador since the 1970s – losing a hotspot of biodiversity. In: *PLOS ONE* 10. DOI: 10.1371/journal.pone.0133701.
- Thuiller, W. (2007): Biodiversity: Climate change and the ecologist. In: *Nature* 448, 550–552. DOI: 10.1038/448550a
- Thomas, C. D.; Cameron, A.; Green, R. E.; Bakkenes, M.; Beaumont, L. J.; Collingham, Y. C.; Erasmus, B. F. N.; Ferreira de Siqueira, M.; Grainger, A.; Hannah, L.; Hughes, L.; Huntley, B.; van Jaarsveld, A. S.; Midgley, G. F.; Miles, L.; Ortega-Huerta, M. A.; Townsend Peterson, A.; Phillips, O. L. and Williams, S. E. (2004):

- Extinction risk from climate change. In: *Nature* 427, 145–148. DOI: 10.1038/nature02121
- Tucker, C. J.; Pinzon, J. E.; Brown, M. E.; Slayback, D.; Pak, E. W.; Mahoney, R.; Vermote, E. and El Saleous, N. (2005): An extended AVHRR 8-km NDVI data set compatible with MODIS and SPOT Vegetation NDVI data. In: *International Journal of Remote Sensing* 26, 4485–4498. DOI: 10.1080/01431160500168686
- Wang, L.; Xiao, P.; Feng, X.; Li, H.; Zhang, W. and Lin, J. (2014): Effective compositing method to produce cloud-free AVHRR image. In: *IEEE Geoscience and Remote Sensing Letters* 11, 328–332. DOI: 10.1109/LGRS.2013.2257672
- WorldClim (2015): Global Climate Data - Free climate data for ecological modeling and GIS. <http://www.worldclim.org> (Date: 25.06.2015).
- Wunder, S. (2000): *The economics of deforestation: the example of Ecuador*. MacMillan and St. Martin Press in association with St. Anthony's College. London.
- Yoshikawa, S. and Sanga-Ngoie, K. (2011): Deforestation dynamics in Mato Grosso in the southern Brazilian Amazon using GIS and NOAA/AVHRR data. In: *International Journal of Remote Sensing* 32, 523–544. DOI: 10.1080/01431160903475225
- Zhang, X.; Friedl, M. A.; Schaaf, C. B.; Schss, C. B.; Strahler, A. H.; Hodges, J. C. F.; Gao, F.; Reed, B. C. and Huete, A. (2003): Monitoring vegetation phenology using MODIS. In: *Remote Sensing of Environment* 84, 471–475. DOI: 10.1016/S0034-4257(02)00135-9

2.7 Supplement 2A

Regional forest cover of the years 1986, 2001 and 2008



3 Estimation of Above Ground Biomass in a Tropical Mountain Forest in Southern Ecuador Using Airborne LiDAR Data

This chapter is published in *Remote Sens.* 2018, **10**(5):660

Received: 19 March 2018 / **Accepted:** 20 April 2018

Estimation of Above Ground Biomass in a Tropical Mountain Forest in Southern Ecuador Using Airborne LiDAR Data

Víctor González-Jaramillo, Andreas Fries, Jörg Zeilinger, Jürgen Homeier,
Jhoana Paladines-Benitez and Jörg Bendix

Abstract: A reliable estimation of Above Ground Biomass (AGB) in Tropical Mountain Forest (TMF) is still complicated, due to fast-changing climate and topographic conditions, which modifies the forest structure within fine scales. The variations in vertical and horizontal forest structure are hardly detectable by small field plots, especially in natural TMF due to the high tree diversity and the inaccessibility of remote areas. Therefore, the present approach used remotely sensed data from a Light Detection and Ranging (LiDAR) sensor in combination with field measurements to estimate AGB accurately for a catchment in the Andes of south-eastern Ecuador. From the LiDAR data, information about horizontal and vertical structure of the TMF could be derived and the vegetation at tree level classified, differentiated between the prevailing forest types (ravine forest, ridge forest and Elfin Forest). Furthermore, topographical variables (Topographic Position Index, TPI; Morphometric Protection Index, MPI) were calculated by means of the high-resolution LiDAR data to analyse the AGB distribution within the catchment. The field measurements included different tree parameters of the species present in the plots, which were used to determine the local mean Wood Density (WD) as well as the specific height-diameter relationship to calculate AGB, applying regional scale modelling at tree level. The results confirmed that field plot measurements alone cannot capture completely the forest structure in TMF but in combination with high resolution LiDAR data, applying a classification at tree level, the AGB amount (Mg ha^{-1}) and its distribution in the entire catchment could be estimated adequately (model accuracy at tree level: $R^2 > 0.91$). It was found that the AGB distribution is strongly related to ridges and depressions (TPI) and to the protection of the site (MPI), because high AGB was also detected at higher elevations (up to 196.6 Mg ha^{-1} , above 2700 m), if the site is situated in depressions (ravine forest) and protected by the surrounding terrain. In general, highest AGB is stored in the protected ravine TMF parts, also at higher elevations, which could only be detected by means of the remote sensed data in high resolution, because most of these areas are inaccessible. Other vegetation units, present in the study catchment

(pasture and subpáramo) do not contain large AGB stocks, which underlines the importance of intact natural forest stands.

Keywords: AGB estimation; Tropical Mountain Forest; LiDAR; Forest Structure

3.1 Introduction

Global forests cover ~31% of the earth surface [1] and play an important role in the global carbon (C) cycle as well as for the climate system [2]. Forests are the most important C stocks and sinks because they store 70–90% of the terrestrial carbon (e.g., [3,4]). However, forested areas are globally endangered by human activities, such as deforestation, which is mainly caused by enhanced population pressure, especially in tropical countries [5]. As the United Nations Framework Convention on Climate Change [6] indicates, the principal cause of today's deforestation is agriculture due to global food demand, as well as clear-cutting to make space for timber plantations [7].

This also holds true for the low-latitude tropical forests, covering ~10% of the Earth's surface [8,9], where deforestation and land use changes have a more corrupting influence on ecosystems than general global warming [10]. Deforestation accounts for 9% to 11% of global anthropogenic greenhouse gas (GHG) emission [11] and therefore is considered as the second major source of anthropogenic CO₂ present in the atmosphere [3,11]. However, the tropical forests still contain ~59% of the total C stored in the global forest biomass [12] but large portions of it are released into the atmosphere due to human activities.

Therefore, the determination of the actual C stocks in the Above Ground Biomass (AGB) of tropical forests is of utmost importance because the storage is rapidly altered by the high deforestation rates observed in tropical countries (e.g., [13]). As Berenguer et al. [14] stated, disturbed forests only store 40% of the AGB compared to undisturbed forests, while the actual C stocks in primary tropical forests must be quantified to evaluate possible future emissions and to illustrate the importance of intact natural forest ecosystems as stocks and sinks for the increasing CO₂ concentration in the atmosphere [15].

For this task, the AGB must be monitored in space and time, which is particularly challenging in Tropical Mountain Forests (TMF; elevation >1000 m above sea level), because of the more complex terrain in comparison to lowland tropical forests [16]. The fast-changing forest structure in tropical mountains is hardly detectable by field measurements, where the forest AGB is estimated by means of individual tree samples taken in relatively small field plots [8,12,17]. Field observations traditionally estimate the

mean forest AGB manually by means of random sampling of felled trees in the forest ecosystems [18]. The tree material is weighted in situ and the obtained values extrapolated to calculate mean AGB for the whole forest stand. More recent field methods use tree cores taken with increment borers to calculate the average Wood Density (WD) of the forest stand, besides other measurements, such as Tree Height (H) and Diameter at Breast Height (DBH) of individual trees present in the plots, to estimate the mean AGB, applying regional scale modelling (e.g., [19,20]). For AGB estimation, different empirical models (regional scale modelling) were developed, such as the models proposed by Chave et al. and Brown [21,22]. Notably, the generic allometric equation of Chave et al. [21] provides good results for an accurate AGB estimation, because the models include WD, H and DBH, in addition to specific variables for particular forest types (e.g., [19,23]). However, forest structure and thus AGB changes rapidly at fine scale in tropical mountains, due to the local topography, climate conditions, soil types and natural or anthropogenic disturbance, modifying the number of tree individuals, H and DBH (e.g., [24,25]). Therefore, plot based studies alone can estimate area-wide AGB in open forest stands or managed forests but in dense natural or unmanaged forests, these methods are limited due to the fast-changing forest structure, difficulty of access and the high cost of large field plot implementation [26]. In consequence, field plot measurements generally under- or overestimate the AGB in dense natural forest stands [3]. As Gourlet-Fleury et al. [27] clarified, for a reliable AGB estimation, the field plot distribution as well as the spatial scale must be fine enough to capture the landscape variability, which is especially complicated in tropical high mountains, because of the relation between forest structure, topography and morphometric protection of the site [16,28–30].

For a reliable quantification of AGB and C stocks, particularly in tropical mountain regions, high resolution data is necessary to detect the alterations in forest structure and land-use changes for smaller areas [12,31]. This can be determined by multispectral remote sensing observations [32], which facilitate information in very high spatial resolution. However, multispectral satellite data only provides two-dimensional information from the upper forest canopy, which can be used for forest type classifications [33,34] but hardly to detect the vertical structure of the forest for AGB and C stock estimations [35,36]. Furthermore, the availability of multispectral satellite data is limited, because areas covered by cloud cannot be classified, which is especially problematic in tropical regions, where cloud frequency is extraordinarily high [9,37].

An accurate estimation of AGB requires a tree level classification [23,38,39], which can be facilitated by modern instruments, like the Light Detection and Ranging (LiDAR) sensor [40,41]. From the three-dimensional LiDAR data, the horizontal and vertical forest structure can be derived as well as the dominant trees identified [42,43]. LiDAR data permits the generation of high resolution Digital Terrain Models (DTM) and high resolution Digital Surface Models (DSM), from which Canopy Height Models (CHM) can be obtained. These data can be used to derive different topographical indices and vegetation properties, such as the height of the vegetation at tree level (e.g., [36,38,44,45]). In general, the LiDAR measurements facilitate information about forest structure at tree level as well as information about the tree canopies, which can be used to detect the forest structure at fine scale and, in combination with field plot measurements, to estimate the AGB of the entire forest stand [46].

Area-wide AGB stock estimates in tropical regions are mainly obtained from forest inventory data by means of summary statistics, calculating mean parameters of WD, H and DBH and applying allometric equations to determine local and regional AGB storage (e.g., [47]). An alternative approach was presented by Asner and Mascaro [46], using LiDAR data in combination with field plot measurements and applying a power-law function of mean top canopy height to estimate the AGB and C distribution for tropical landscapes. However, the mean values of WD, H and DBH vary significantly at local and regional scale [48] as well as the number of individual trees at fine scale [24,25]. Hence, specific local mean WD and height-diameter relationships must be calculated and an individual tree classification applied to improve the final results [39,49].

Nonetheless, during recent years the knowledge about AGB storage in the tropical lowland forests was extended through the synthesis of plot inventory data and remote sensed data (e.g., [50–53]) but in TMF (elevation >1000 m above sea level) information is still needed [54], because an adequate field plot distribution as well as the availability of suitable high resolution remote sensed data is limited due to the difficulty in access, the complex topography (large elevation differences, steep slopes, etc.; [55–57]) and the fast changing climatic conditions [24,25]. Furthermore, to generate area-wide AGB and C maps as well as to illustrate the AGB distribution at local and regional scale, the land cover variability must be considered, identifying areas of forest, pastures and disturbance adequately [54,56].

The available information about AGB stocks and distribution in TMF is principally based on field plot data installed in undisturbed forest parts, calculating the local or regional AGB stock by multiplying the mean value per plot-area with the area of the forest region [58,59]. Although attempts were carried out to correlate the AGB with topographical and climatological variables, such as elevation (e.g., [60]), slope angle (e.g., [61]), temperature (e.g., [62]) and rainfall (e.g., [50]), the results did not indicate overall trends [59]. For the Andes in South America it is generally stated that AGB decreases with increasing elevation and slope angle [24,56] but depending upon the prevailing soil type and the nutrient availability [63–65]. However, Spracklen and Righelato [59] synthesized field plot measurements in TMF from different parts of the world and concluded that only a low to moderate correlation between AGB and elevation as well as slope angle, temperature or rainfall exists.

The lack of correlation between AGB and topographical as well as climatological variables was also stated in other studies (e.g., [50,66]), which indicates that these parameters only explain a fraction of the AGB variability in TMF, why additional environmental parameters must be analysed [59]. Therefore, the present study estimates the AGB and C stocks of a natural TMF inside a small watershed in the south-eastern Andes of Ecuador, using high resolution LiDAR data in combination with field plot measurements, while applying regional scale modelling at tree level. From the LiDAR data the H of the individual trees as well as the forest, terrain and land cover structure can be derived, whereas from the field plot measurements the local mean WD and the specific height-diameter relationship are obtained. The AGB stock and its distribution are analysed by means of the Topographic Position Index (TPI), which identifies ridges and depressions [30,67] and the Morphometric Protection Index (MPI), which illustrates the sheltering effect of the surrounding terrain [29]. The results are compared to AGB values calculated in previous plot-based investigations within the same area. The study also intends to demonstrate the importance of intact primary forest ecosystems as C stocks considering the ongoing deforestation, especially in tropical high mountains.

3.2 Materials and methods

3.2.1 Study Area

The research area, the San Francisco watershed, is located in the eastern escarpment of the south Ecuadorian Andes between the cities of Loja and Zamora (Figure 3-1), with drainage into the Amazon Basin. The catchment is part of the Cordillera Real and has an extension of ~85 km², including the “Reserva Biológica San Francisco” (RBSF) where the research station Estación Científica San Francisco (ECSF: lat. 3°58'18"S, long. 79°4'45"W, 1860 m above sea level; Figure 3-1) is situated. The altitudes range from 1600 m above sea level at the river outlet to 3200 m above sea level at the highest mountain tops [68]. The Andes between southern Ecuador and northern Peru are characterized by lower mean altitudes compared to other parts of the mountain range (Andean Depression, the Amotape-Huancabamba Depression), only reaching 3900 m above sea level at the highest mountains. Therefore, a strong exchange between the Ecuadorian coastal vegetation and the Amazon vegetation exists, leading to extraordinarily high biodiversity in this region (hottest hotspot in biodiversity; for example, References [69,70]).

The vegetation in the catchment can be divided into three classes of ecosystems: Tropical Mountain Forest (TMF), subpáramo and pastures [71]. The TMF (Figure 3-2a) is mostly undisturbed and covers the slopes of the southern, western and the upper parts of the northern ridge up to the tree line at ~2700 m above sea level [72]. The natural forest structure is related to the topography and can be divided into lower slope (ravine) forest and upper slope (ridge) forest (e.g., [16]). The ravine forest is characterized by lower stem density but higher basal areas (diameters) and canopy heights compared to the ridge forest, where less tree species are also observed [25]. The difference in forest structure is mainly due to the climatic conditions and the prevailing soil types [73–75]. As identified by Homeier et al. [76], the most abundant tree genera are *Miconia* (*Melastomatac*), *Ocotea* (*Laurac*), *Persea* (*Laurac*), *Ficus* (*Morac*), *Weinmannia* (*Cunoniac*), *Ilex* (*Aquifoliac*), *Hedyosmum* (*Chorantac*), *Inga* (*Fabac*), *Scheffera* (*Araliac*) and *Clusia* (*Clusiaceae*).

Between ~2700 m and ~3000 m above sea level a transition zone between the TMF and a shrub-dominated subpáramo exists, where patches of Elfin Forest (Figure 3-2b), the so-

called Ceja Andina, dominate the landscape. The Elfin forest is characterized by small trees, reaching heights up to 10 m [28]. Over 3000 m above sea level a shrub-dominated subpáramo (Figure 3-2c) prevails, which is the lowest and most diverse altitudinal zone of the páramo area, where aspects of the grass páramo (above) and the mountain forest (below) are mixed [77].

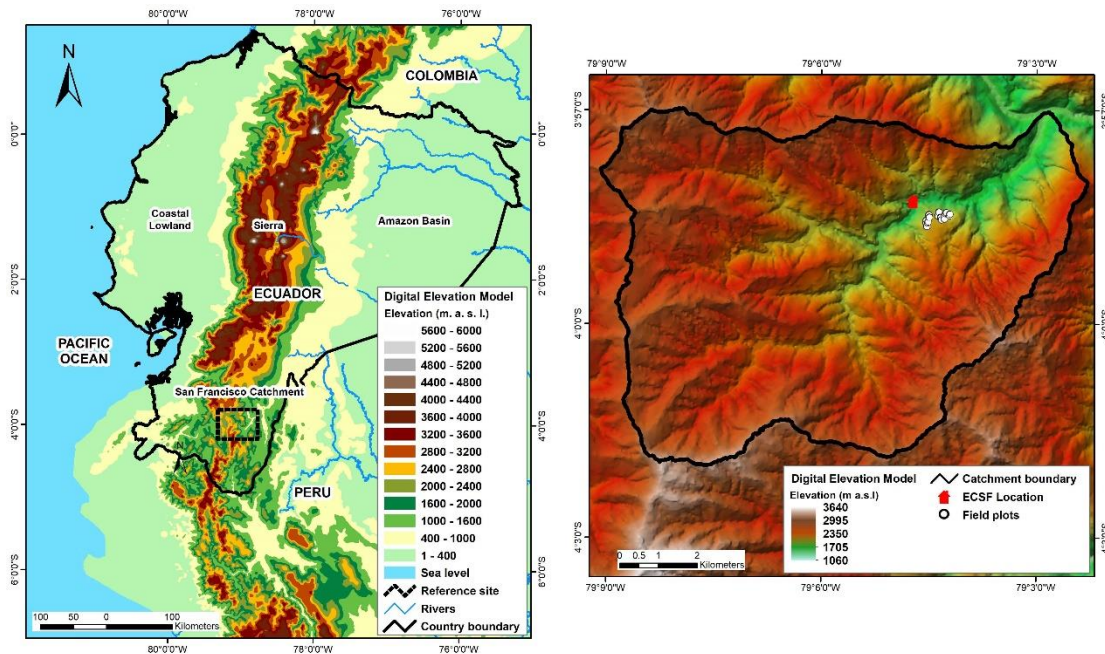


Figure 3-1: Digital Elevation Model (DEM) of the study area, the San Francisco catchment, including the field plot distribution.

The pastures (Figure 3-2d) cover mainly the lower parts of the northern mountain ridge, where the natural mountain forest was replaced by anthropogenic slash-and-burn activities [71,78]. However, some parts of the pastures have already been abandoned and dense stands of bracken fern, which are resistant to burn activities [79], have infested these areas [68,80].

The climate in the study catchment is per-humid with marked altitudinal gradients in air temperature, relative humidity [81,82] and rainfall [78,83]. The annual mean air temperature ranges from 19.4 °C at the valley bottom to 9.4 °C at the mountain tops, whereas annual mean relative humidity varies between 77% at the pasture sites and almost 100% inside the TMF as well as at the mountain ridges. The annual rainfall amounts reach 2300 mm near the valley bottom and 6700 mm at the mountain tops. These values of annual precipitation include rain and fog water precipitation, because clouds and fog

deposit water directly onto the vegetation and therefore must be considered as relevant available water input from the atmosphere [84]. The seasonal rainfall distribution of the watershed shows a clear annual cycle with the main rainy season in austral winter (between May and September) and a relative dry season in austral summer (between November and February).

3.2.2 LiDAR Data and Field Measurements

An airborne Light Detection and Ranging (LiDAR) survey in the study area was conducted in two campaigns in March and November 2012, due to the adverse climate conditions at the beginning and during the rainy season. The LiDAR data was obtained from a Leica Geosystem ALS50-II laser scanner installed on a Eurocopter AS350B2 Ecureuil helicopter. Table 3-1 shows the principal specifications of the equipment used. The Airborne Laser Scanning (ALS) produced point clouds with a density of at least 10 pulses per 1 m² for the entire watershed and a buffer around it, to ensure that all boundaries of the catchment were covered (total area: 108.93 km²). The point clouds of the study area were subdivided into 257 tiles to simplify the handling of the information. For more information about the LiDAR survey, please refer to Silva and Bendix [85].



Figure 3-2: Principal vegetation units in the San Francisco catchment: (a) Tropical Mountain Forest (TMF), (b) Elfin Forest, (c) subpáramo and (d) pasture.

Table 3-1: Leica Geosystems ALS-50 II CM specifications.

Parameter	Value
Scanning pattern	Sinusoid
Field Of View, deg	0–75
Pulse Rate (maximum), kHz	150
Pulse Wavelength, nm d	1064
Scan Rate (maximum), Hz	90
Number of returns	4

The forest inventory data used includes measurements of WD (tree cores), H (ultrasonic tree height meter) and DBH (dendrometer) of the tree species within the two different mountain forest types (ravine and ridge) along an altitudinal gradient from 1900 m to 2100 m above sea level (see Figure 3-1) [76,86]. The data was collected between 2010 and 2014 under dense canopies without larger forest gaps (<2 m) and consists of 540 tree samples from 18 plots of 0.04 ha [24,25]. To consider the local topography as well as the general forest structure, six plots were situated at the upper slope, six plots at the mid-slope and six plots at the lower slope.

3.2.3 Methods

The processing chain to estimate AGB and C stocks of the TMF as well as its distribution influenced by the forest structure is shown in Figure 3-3. AGB and C stock were only estimated for the TMF and the Elfin Forest by means of the LiDAR data in combination with field measurements, considering only trees higher than 5 m with a DBH greater than 10 cm, as recommended by Li et al. and Gianico et al. [87,88]. For the other vegetation units (pastures and subpáramo) the AGB and respectively C stock values from previous investigations inside or next to the study area were used [89,90].

The mean AGB value for the shrub-dominated subpáramo area was taken from Eguiguren et al. [90], who evaluated the C stock in the Podocarpus National Park, next to the study area. They established 25 plots of 1 m² at different altitudes and soil types, estimating a mean C stock of 8.2 Mg C ha⁻¹ for shrub-dominated areas. The C stock can be converted to AGB, applying a factor of 2, as Tan et al. and Ota et al. [33,44] demonstrated, which results in a mean AGB of 16.4 Mg ha⁻¹ for the subpáramo area.

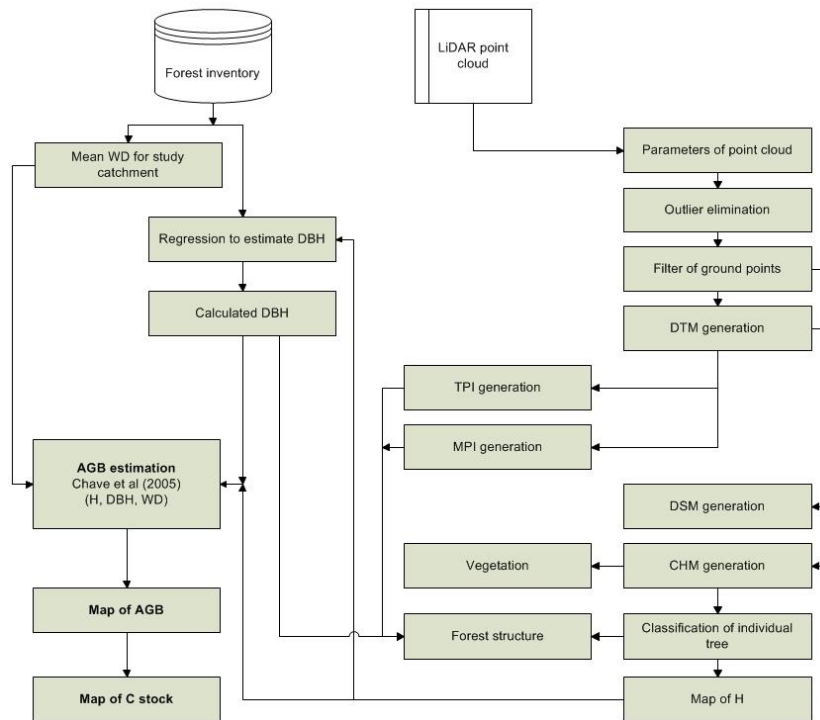


Figure 3-3: Processing chain to calculate above ground biomass (AGB) and C stock based on LiDAR point cloud data (WD = Wood Density, H = Tree Height, DBH = Diameter at Breast Height, DTM = Digital Terrain Model, DSM = Digital Surface Model, CHM = Canopy Height Model, TPI= Topographic Position Index and MPI= Morphometric Protection Index).

AGB values for recently abandoned tropical pastures (1–2 years) range between 2 Mg ha⁻¹ and 18 Mg ha⁻¹ with higher values for pasture with relict trees [8,79]. However, Knoke et al. [89] investigated C stocks for tropical pasture in southern Ecuador, based on CLM-DGVM modelling [91] and calculated values between 12.5 Mg C ha⁻¹ (low-input pastures) to 33.0 Mg C ha⁻¹ (long time abandoned pastures), which includes the whole C stock of the plant (roots and shoot). In the study catchment most of the pastures are in use and relict trees are generally isolated, in addition to a negligible pasture management (low-input pastures, own observations). Therefore, the C stock for low-input pastures was converted into AGB applying the shoot-root ratio for C4 grasses (here: mainly *Setaria sphacelata*; [79]), which resulted in a mean value of 10.8 Mg ha⁻¹ for the pasture site.

For an accurate AGB estimation different equations exist (e.g., [19,22]), in which one frequently used approach is the regional scale model of Chave et al. [21], who presented different equations for specific tropical forests types (dry forest, moist forest, moist

mangrove forest and wet forest). Due to the climate conditions in the study area, the equation for wet tropical forest stands was selected, which was also applied in previous plot based AGB estimation studies inside the San Francisco watershed [24,25,73] and in plot-based AGB estimations in other TMF in southern Ecuador [8]. However, due to the fast-changing forest structure in the TMF [25] a calculation at tree level is necessary [23,38,39], which can be realized by means of the LiDAR data in combination with the field measurements [40,41]. The equation to estimate the AGB at tree level can be written as follows:

$$AGB_{tree} = \exp(-2.557 + 0.940 \times \ln(\rho D^2 H)) = 0.0776 \times (\rho D^2 H)^{0.940} \quad (1)$$

where AGB_{tree} is the AGB of a specific tree (Mg), ρ is the average WD ($gr\ cm^{-3}$), D is the particular DBH (cm) and H the particular height of the tree (m).

The WD was determined by the extraction of tree cores (increment borer) from the species present in the installed field plots, following the method described by [18]. This method is non-destructive and recommended for tropical forest trees. The tree cores were taken at breast height and the WD of the individual trees determined by the ratio of the oven-dry wood mass and the green wood volume [76]. However, WD varies between the tree species and during the lifetime of the tree as well as within the same tree because the wood of the branches as well as the different parts of the trunk (interior and exterior) present different values [23]. To solve this problem, mean WD for the whole forest stand was calculated, averaging all individual WD from the trees sampled [8].

Due to the selective forest inventory (plot based), H and DBH field measurements were only used to establish a height-diameter relationship [92], because obtaining these values for all individual trees inside the catchment is difficult to realize. In general, height-diameter relationships vary significantly between regions because of the species composition and local climate conditions [49]. To determine the local relationship 244 tree measurements were used and the remaining trees sampled were preserved for validation. To the selected H and DBH data a logarithmic transformation was applied, as suggested by Gianico et al. and Djomo and Chimi [88,93] and then a linear regression analysis executed (Figure 3-4; [94]). The obtained local height-diameter relationship for this TMF is shown in Figure 3-4.

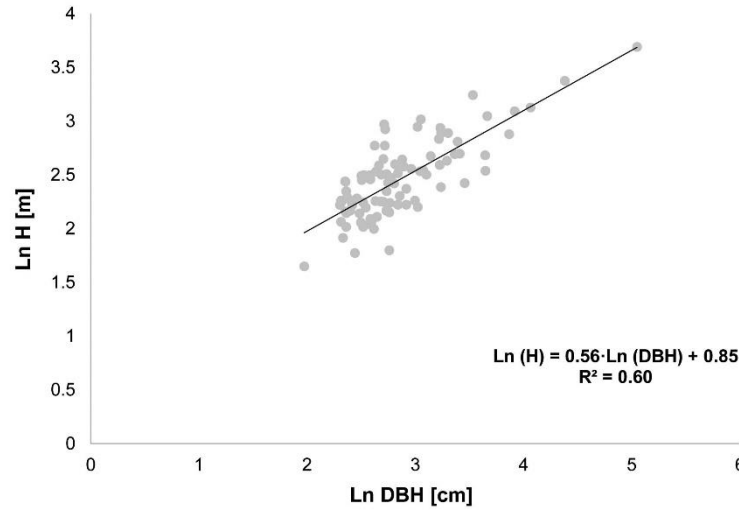


Figure 3-4: Relationship between DBH (cm) and H (m) of the field measurements.

The calculated coefficient of determination (R^2) indicates a low positive correlation between DBH and H ($R^2 = 0.60$), which is acceptable, due to fast changing topography and soil types, modifying the number of tree individuals, H and DBH [24,25,49]. Nevertheless, the calculated p-value (<0.001) confirmed a high significance of the relationship between H and DBH for the TMF in the study catchment.

The height-diameter relationship equation (Figure 3-4) was transposed to calculate the DBH (Equation (2)), because H was deviated from the LiDAR data.

$$\text{DBH} = e^{\left(\frac{\text{Ln(H)} - 0.85}{0.56}\right)} \quad (2)$$

In general, the LiDAR point clouds (raw data) facilitate information about the vertical and horizontal structure of the terrain and the vegetation [35]. From these data a DTM as well as a DSM can be generated, from which a CHM can be extracted [95]. Based on the CHM, the individual trees were detected and their specific height determined.

For this, the LiDAR point clouds were first corrected and processed by means of the software FUSION (Version 3.7), developed by the U. S. Department of Agriculture, Forest Service [42]. To assure the quality of the derived products, the point clouds were analysed with the Catalog tool, which evaluates several important metrics of the LiDAR data and the completeness of data coverage as well as the pulse return density. Then, outliers within the tiles were detected and eliminated, executing the FilterData extension of FUSION. Therefore, the mean elevation and its standard deviation within a user-

defined grid (here: $10\text{ m} \times 10\text{ m}$) was calculated and the individual point compared to the mean value. If the point value in the established grid cell was higher or lower than the mean elevation, adding 3 times the standard deviation, the point was eliminated as an outlier [38]. This tool detects the presence of electricity towers, power lines and so forth, which cause errors in the subsequent individual tree classifications because these objects are not part of the natural surface or the vegetation.

After the outlier elimination, the GroundFilter tool of FUSION was applied to determine the lowest elevations of each pulse return (bare-earth points) as well as the highest elevation of each pulse return (canopy height). Therefore, all cloud points are screened to identify the respective extreme values [42]. By means of these data a DTM was created, using the GridSurfaceCreate extension, which averages the bare-earth points for each grid cell. However, Jochem et al. [35] indicated that for an adequate DTM generation, different resolutions should be evaluated, because the optimal resolution depends on the requirements of the final product [45]. The analysis resulted in a final cell size of $0.25\text{ m} \times 0.25\text{ m}$, because with lower resolution the individual trees were not classified correctly [45,96].

Then, a DSM was generated, executing the CanopyModel extension of FUSION, which determine the canopy height. Therefore, the highest elevation pulse returns were identified and averaged to obtain a single value for the established grid cell ($0.25\text{ m} \times 0.25\text{ m}$). Subsequently, a CHM, which displays the above ground vegetation heights, was created, subtracting the generated DTM and DSM maps. For the tree detection process the CHM was smoothed, applying user defined mean and median filters (here: 5×5) integrated in this extension. Thereby, the local maxima are preserved while the surrounding cells (here: crowns) smoothed to adhere the highest point of a tree [42,96]. The individual trees were identified by means of the CanopyMaxima tool of FUSION, which detects local maxima by means of a variable-size evaluation window (here: 3×3) [97]. The tool identifies H and the location of dominant/codominant trees within the forest stand because mid-story and under-story trees are often covered by a higher canopy layer [42]. To evaluate the tree detection process for the study area, the number of detected trees as well as their H and their derived DBH were compared to the field plot measurements, which were not used for the determination of the local height-diameter relationship.

Based on the determined mean WD, the deviated DBH and the H of each detected tree, Equation (1) was applied to calculate the AGB at tree level. To calculate AGB (Mg ha^{-1}) and C stocks (Mg C ha^{-1}) of the TMF, first a land cover classification had to be performed, using the generated CHM ($0.25 \text{ m} \times 0.25 \text{ m}$ resolution) to determine the areas where forest is present. Therefore, a grid layer with a $1 \text{ ha} \times 1 \text{ ha}$ resolution was created and overlaid with the CHM. Then, each hectare grid was analysed and classified as forest if more than 50% of the included CHM pixels were higher than 5 m [87]. For non-forest grids, the AGB values for pasture (10.8 Mg ha^{-1}) and subpáramo (16.8 Mg ha^{-1}) were assigned, depending on the altitude (threshold 2700 m above sea level). To obtain AGB for the TMF, all individual AGB at tree level within a grid cell ($1 \text{ ha} \times 1 \text{ ha}$) were added up [98]. Finally, the C stock was calculated by multiplying the AGB with a factor of 0.5 [33,44].

In order to analyse the relationship of the complex topography, the forest structure and the AGB distribution in the study area, the Topographic Position Index (TPI), which identifies ridges and depressions [30,67] and the Morphometric Protection Index (MPI), which illustrates the sheltering effect of the surrounding terrain or the exposure of the cell [29], were calculated by means of the DTM ($0.25 \text{ m} \times 0.25 \text{ m}$ resolution), using the software SAGA GIS [99,100]. The TPI compares the elevation of each grid cell to the mean elevation within a specific distance to determine whether the position of the cell is situated on a ridge (positive values) or in a valley (negative values), which permits the separation into ravine and ridge forest [101]. The MPI evaluates, up to a given distance, whether the respective cell is protected by the surrounding relief to illustrate the topographic preference for bigger trees within the forest stands [29]. MPI-values near zero indicate unprotected locations, whereas higher positive values indicate the degree of protection of a grid cell within the catchment. In this study the distance for both indices was set to 100 m, as Detto et al. [102] recommended, due to the fast-changing topography, because canopy heights are strongly related to the proximity to depressions and the exposure of the site [29]. Furthermore, this distance also warrants the detection of smaller subsidiary valleys and ridges.

To illustrate the importance of the field plot distribution and size to capture the landscape variability for a reliable AGB estimation in natural TMF [27,103], the DBH of each detected tree was related to TPI and MPI. Therefore, a threshold of 20 cm (DBH) was

defined, as Bunning et al. [104] suggested, to analyse the conditions of forest trees. The results were related to the AGB distribution inside the San Francisco catchment, because dominant or bigger trees within a forest stand represent 70% to 90% of the total AGB [41,105,106].

3.3 Results

To estimate the AGB at tree level (Equation (1)) WD, H and DBH of each individual tree is necessary. The mean WD of the TMF, based on the field measurements, was determined at 0.59 g cm^{-3} , which was applied to every tree detected in the study catchment. The individual trees were identified by means of the CHM (Figure 3-5a) derived from the LiDAR data (DTM–DSM), which resulted in a total of 1,932,188 trees detected in the whole study catchment, including their position and H (Figure 3-5b). The H of each detected tree was used to calculate their specific DBH, applying Equation (2).

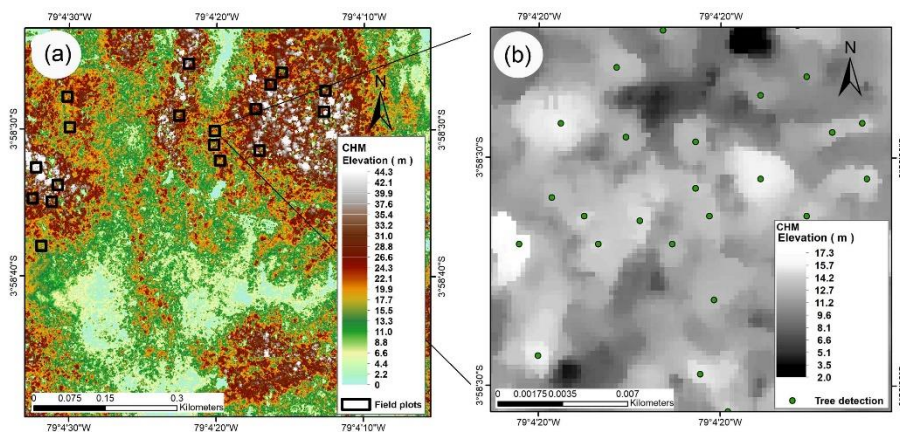


Figure 3-5: (a) Canopy Height Model (CHM), including field plots; (b) Example of the individual tree classification for one plot in the study area.

To evaluate these results, the specific H and DBH of the identified trees were compared to the field plot inventory (18 plots). As explained in Section 3.2.3, only the H and DBH measurements, which were not used for the determination of the local height-diameter relationship, were included for validation. During the field campaign 540 trees higher than 5 m with a DBH greater than 10 cm were sampled within the 18 plots. The tree detection process, based on the LiDAR data, found 319 dominant/codominant trees,

which corresponds to 55% of the trees present in the different plots (see example Figure 3-5b). The H of the detected trees were compared to the H measurements, realized by means of an ultrasonic tree height meter in the field (Figure 3-6a) and their derived DBH (Equation (2)) to the dendrometer measurements (Figure 3-6b). The results indicated a very good correlation for H and DBH with a coefficient of determination (R^2) of 0.92 (p -value < 0.001) and 0.93 (p -value < 0.001) respectively. However, the H of smaller trees up to 15 m were slightly underestimated as well as trees higher than 25 m, whereas trees with H between 15 m and 25 m were slightly overestimated (1:1 line; Figure 3-6a). The estimated DBH of the individual trees showed the same behaviour, because DBH of trees up to 25 cm as well as over 60 cm were slightly underestimated, whereas trees between 25 cm and 60 cm overestimated, caused by the applied local height-diameter relationship (Figure 3-6b).

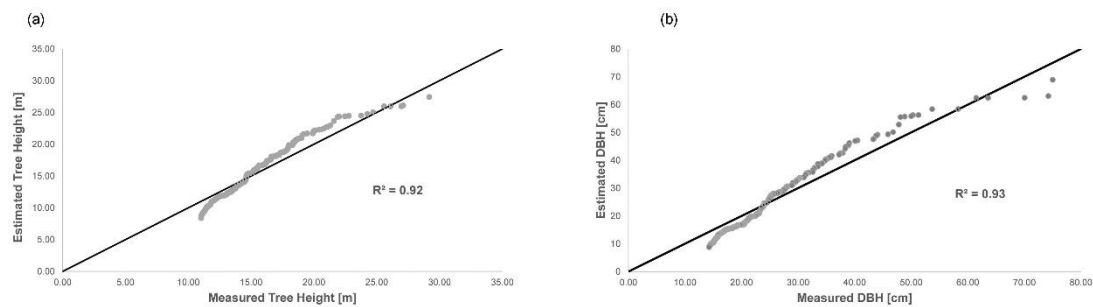


Figure 3-6: (a) Measured H compared to estimated H, derived from the LiDAR data; (b) Measured DBH compared to estimated DBH, obtained from the local height-diameter relationship.

To integrate the forest structure in the AGB estimation, the TPI (Figure 3-7a) as well as the MPI (Figure 3-7b) were calculated. These indices were used to identify the areas of ravine forest and ridge forest and to illustrate the protection of the site, because from these parameters the forest structure and the AGB distribution in the catchment can be deduced [29,101]. Therefore, a threshold of 20 cm (DBH) was set to depict the position of bigger trees within the forest stand [104]. All trees with respectively higher and lower DBH were marked in a different colour (Figure 3-7c). It is clearly visible that smaller trees with concurrently lower basal area (DBH) are mainly situated at unprotected sites, such as ridges or at slopes near the ridges (red polygons), whereas bigger trees cover the side valleys down to the valley bottom, protected by the surrounding relief (green polygons). The same distinction was made for the Elfin Forest areas above 2700 m above sea level

(Figure 3-7c), where bigger trees are situated inside the upper side valleys and smaller, more isolated, trees at the ridges.

The ravine and ridge forest classifications were used to analyse the mean and extreme values (H, DBH and AGB) at tree level within the San Francisco watershed (Table 3-2). For the ravine TMF (up to 2700 m) an average H of 13.3 m was calculated, whereas the trees in ridge TMF only had an average H of 11.3 m. In the Elfin Forest (over 2700 m) average H is generally lower, reaching 11.0 m in the ravine forest and 8.9 m in the ridge forest parts. The biggest trees were found in the protected ravine TMF areas, reaching heights of up to 48.4 m, whereas maximum H in the ridge TMF reached only 26.8 m at lower and more protected sites. The maximum H in the Elfin Forest is notably lower but the biggest trees are also situated at more protected areas inside the upper side valleys, reaching heights up to 15.7 m (Table 3-2).

DBH was derived from H (Equation (2)), which means that bigger trees concurrently have a greater basal area. The calculated DBH of the trees in the San Francisco catchment ranges between 10.0 cm and 223.1 cm in the ravine TMF (average 23.5 cm) and between 10.0 cm and 77.8 cm in the ridge TMF (average 17.1 cm; Table 3-2). In the Elfin Forest, tree DBH is notably smaller, reaching maximum values up to 30.1 cm in the ravine forest (average 16.4 cm) and 17.1 cm at the upper ridges (average 12.9 cm; Table 3-2). The biggest trees were found in the lower ravine TMF near the river outlet as well as at more protected lower ridges.

H and DBH are directly correlated to the AGB (Equation (1), [21]) and therefore AGB per tree vary notably within the different forest types. The mean AGB per tree in the ravine TMF was estimated at 0.3 Mg, whereas the mean AGB per tree in the ridge TMF resulted in 0.1 Mg. For the ravine Elfin Forest mean AGB per tree also resulted in 0.1 Mg but for the ridge Elfin Forest a mean AGB of 0.0 Mg was determined. Maximum AGB per tree was obtained for the lower ravine TMF, indicating values up to 47.1 Mg, whereas for the biggest trees in ridge Elfin Forest only an AGB of 0.1 Mg was estimated (Table 3-2). To evaluate these findings, the estimated AGB per tree were compared to the AGB per tree calculated from the plot data inventory (Figure 3-8). It is clearly visible that the AGB per tree is generally overestimated, which is mainly due to the applied average WD value, because Werner and Homeier [25] applied the specific WD to each individual tree species and the established local height-diameter relationship, which slightly

overestimates the DBH of the individual trees (see Figure 3-6b). However, the coefficient of determination ($R^2 = 0.91$; p -value < 0.001) indicated a very good correlation between measured and estimated AGB values per tree.

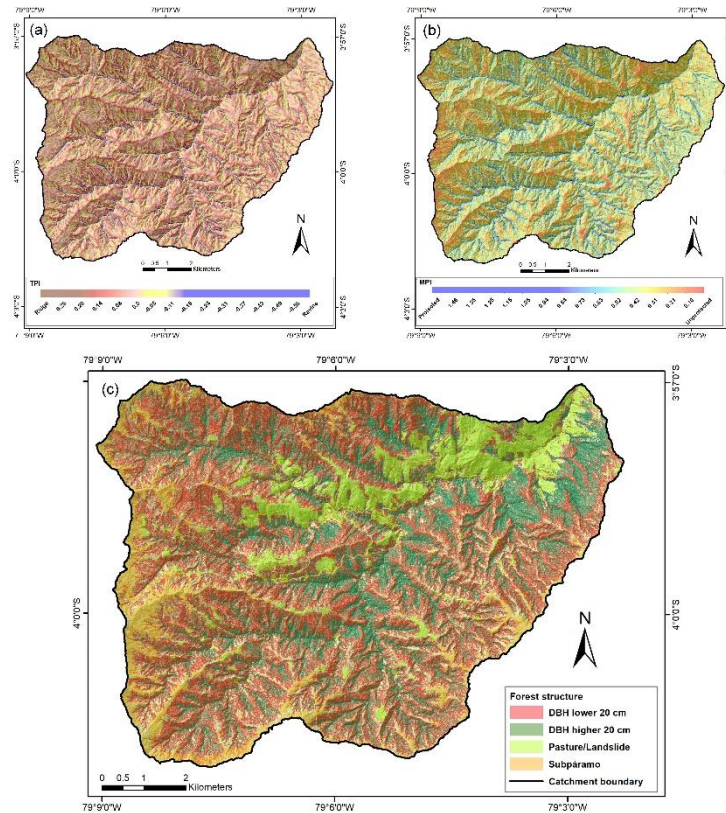


Figure 3-7: Forest structure detected in the research catchment by means of (a) TPI; (b) MPI; (c) distribution of trees with a DBH smaller than 20 cm (red) and bigger than 20 cm (green).

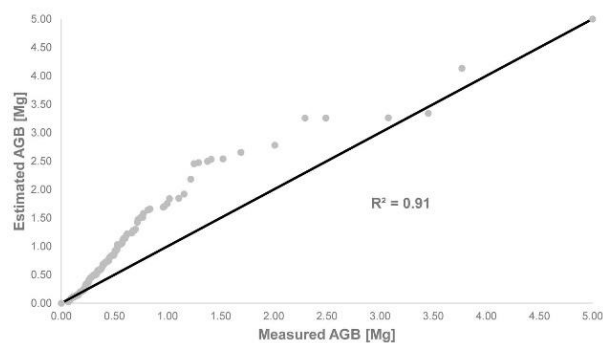


Figure 3-8: Calculated AGB by means of the individual tree measurements compared to estimated AGB.

The minimum H, DBH and AGB values per tree were equal for all forest types, due to the thresholds applied in this study, because only trees higher than 5 m with a DBH greater than 10 cm were considered (see Section 2.3 and Table 3-2; [87,88]).

Table 3-2: Mean and extreme values of H, DBH and AGB for individual trees in the TMF and the Elfin Forest.

Forest Type	Tree Individuals	H [m]			DBH [cm]			AGB Tree [Mg]		
		Min	Mean	Max	Min	Mean	Max	Min	Mean	Max
TMF	1,638,767									
Ravine	1,470,493	8.5	13.3	48.4	10.0	23.5	223.3	0.0	0.3	47.1
Ridge	168,274	8.5	11.3	26.8	10.0	17.1	77.8	0.0	0.1	3.7
Elfin Forest	293,421									
Ravine	271,717	8.5	11.0	15.7	10.0	16.4	30.1	0.0	0.1	0.4
Ridge	21,704	8.5	8.9	11.5	10.0	12.9	17.1	0.0	0.0	0.1

To illustrate the general forest structure within both forest types (ravine and ridge), the individual H (Figure 3-9a,b) and DBH (Figure 3-9c,d) of the trees were integrated into classes and the percentage of each class respective to the total number of trees calculated (Figure 3-9). The ravine TMF is generally characterized by trees with H between 10.0 m and 22.5 m, representing more than 97.2% of this forest type. The trees in the ravine Elfin Forest are notably smaller, reaching only heights up to 17.5 m, in which trees up to 15.0 m represent 97.3% (Figure 3-9a). H in the ridge TMF generally do not pass 20.0 m (99.2% of the forest stand), in which 91.8% of the trees only reach heights up to 15.0 m. In the ridge Elfin Forest, trees predominantly of up to 10.0 m can be found (62.5%), due to the adverse climate conditions (low temperatures [81] and strong winds [75]); biggest trees with H up to 12.5 m only exist at the more protected upper ridges (Figure 3-9b).

Respective to the DBH, the ravine TMF is generally characterized by trees with a DBH between 10.0 cm and 50.0 cm, representing more than 95.1% of this forest type. Most of the trees reach DBH up to 40.0 cm (89.9%), whereas the biggest trees (DBH > 50.0 cm) only occupy 4.9%. The DBH of trees in the ravine Elfin Forest do not exceed 30.0 cm, in which trees with a DBH up to 25.0 cm represent 92.7% of the forest type (Figure 3-9c). In the ridge TMF, trees are smaller compared to the ravine TMF, reaching mostly DBH up to 35.0 cm (97.0%). Trees with a DBH greater than 45.0 cm are generally absent in this forest type with some exceptions at the lower highly protected ridges. In the ridge

Elfin Forest only trees with a DBH up to 20.0 cm exist (100.0%) but the majority reach DBH around 15.0 cm (82.6%; Figure 3-9d).

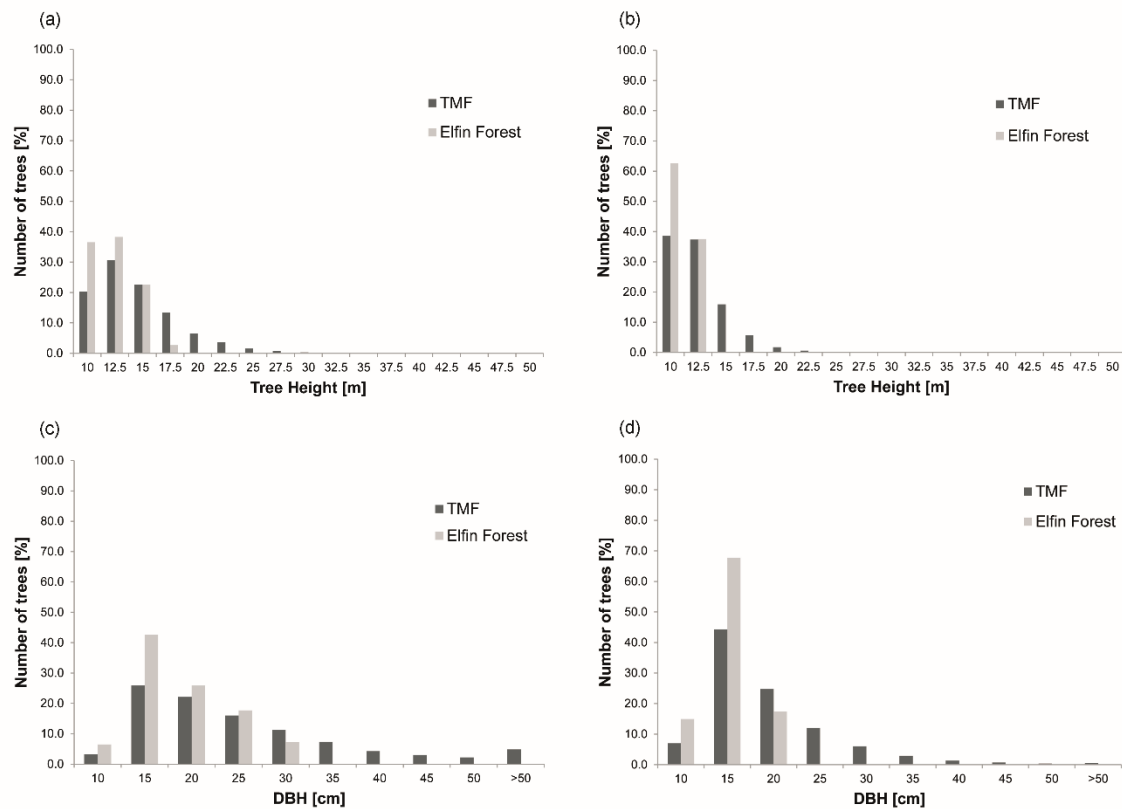


Figure 3-9: Portion of trees in the established H (above) and DBH (below) classes, divided in ravine forest: (a and c), and ridge forest (b and d).

Figure 3-10 illustrates the percentage of the different tree-height classes respective to total AGB value of the two forest types. In the ravine TMF the trees with heights between 15.0 m and 30.0 m contribute 82.7% of the total AGB (Figure 3-10a), representing only 48.8% of the trees present there (see Figure 3-9a). Trees smaller than 15.0 m only add 10.6% of the total AGB, standing for 51.0% of the trees, whereas trees bigger than 30 m account for 6.7% of the total AGB, representing only 0.2% of this forest type. In the ravine Elfin Forest, the situation is similar, because trees bigger than 15.0 m contribute 53.5% of the total AGB, accounting only for 25.2% of all trees present there. Trees up to 15.0 m are most frequent in this forest type (74.8%, Figure 3-10a) but their contribution to the total AGB is only 46.5% (Figure 3-9a).

The same distribution was found in the ridge forest areas (Figure 3-9b). In the ridge TMF trees higher than 15.0 m account for 63.7% of the total AGB, representing 24.1% of the

trees within this forest type (Figure 3-10b). Only 2.6% of trees are taller than 20 m but these trees contribute 20.9% to the total AGB. Trees up to 15.0 m represent 75.9% of this forest stand, which only add 36.3% to the total AGB. Also in the ridge Elfin Forest, where trees higher than 15.0 m are absent (Figure 3-9b), the biggest trees (taller than 12.5 m) contribute the majority of the total AGB (52.2%), representing only 37.5% of the trees; whereas trees of up to 12.5 m only account 47.8% for the total AGB in this forest type (Figure 3-10b).

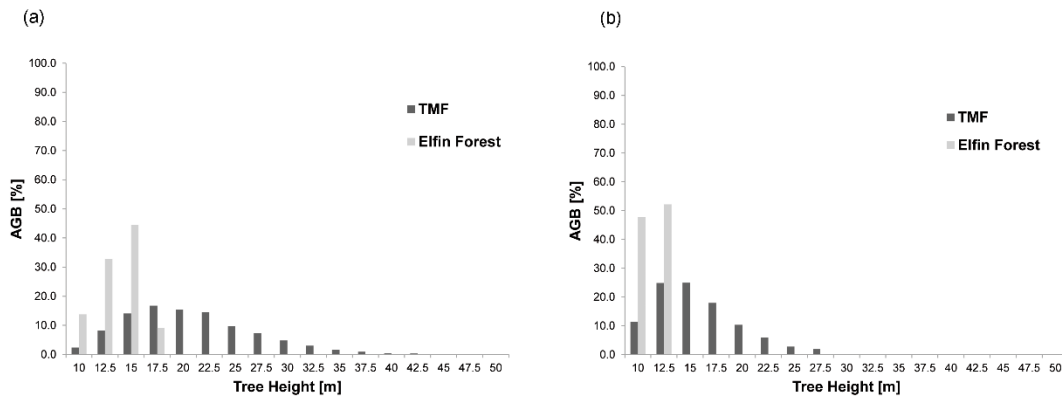


Figure 3-10: Portion of total AGB of the established H classes; (a) ravine forest, (b) ridge forest.

To obtain an AGB value (Mg ha^{-1}) for areas covered by forest, a land cover classification was initially performed (Figure 3-11). Therefore, a grid mask of $1 \text{ ha} \times 1 \text{ ha}$ was overlaid with the CHM and all grids classified as forest if more than 50% of the included CHM pixels were higher than 5 m [87]. Then, all AGB values of the individual trees within a grid cell were added up. Due to the complex terrain in the study area, it was only possible to analyse the differences between TMF and Elfin Forest, whereas a distinction between ravine and ridge forest areas was unfeasible.

The TMF covers 4608 ha of the San Francisco watershed, whereas the Elfin Forest only 1529 ha. The remaining hectares were classified as pasture (10.8 Mg ha^{-1}) or subpáramo (16.4 Mg ha^{-1}), depending on the elevation (threshold 2700 m), where the respective AGB values was set. The calculated mean AGB of the TMF was 106.2 Mg ha^{-1} , which is considerably higher compared to the Elfin Forest where only 32.8 Mg ha^{-1} was estimated (Table 3-3). Maximum AGB for the TMF was 664.1 Mg ha^{-1} , found at the lower ravine TMF near the river outlet, where undisturbed and dense forest stands exist, highly protected by the surrounding terrain (see Figure 3-6); whereas minimum AGB was

10.0 Mg ha⁻¹, displayed at the upper ridges (Figure 3-12). For the Elfin Forest, maximum AGB (196.6 Mg ha⁻¹) was estimated at protected areas inside the upper side valleys and minimum values (2.1 Mg ha⁻¹) at the exposed upper ridges (Table 3-3). The spatial distribution of AGB in the study catchment is shown in Figure 3-12.

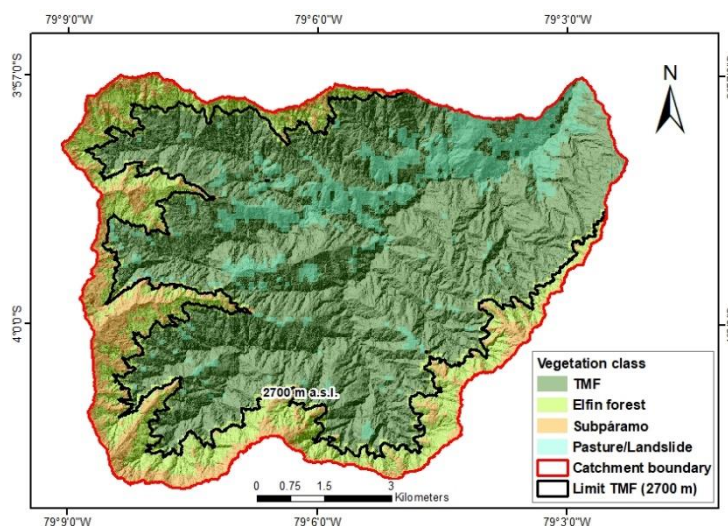


Figure 3-11: Land cover map in the San Francisco catchment obtained from the CHM (resolution 1 ha × 1 ha).

Table 3-3: AGB and C stock in the San Francisco catchment.

		AGB				C Stock			
		[Mg ha ⁻¹]				[Mg ha ⁻¹]			
Forest Type	N [ha]	Min	Mean	Max	SD	Min	Mean	Max	SD
TMF *	4608	10.0	106.2	664.1	94.1	5.0	53.1	332.0	47.0
Elfin Forest	1529	2.1	32.8	196.6	28.8	1.1	16.4	98.3	14.4

* TMF = Tropical Mountain Forest.

As mentioned before, AGB can be converted directly into C stock, applying a factor of 0.5 [33,44]. C stock is principally stored in the TMF ecosystem (average 53.1 Mg C ha⁻¹), especially in the ravine forest inside the side valleys and at the valley bottom, where undisturbed and dense forest stands exist (max. 332.0 Mg C ha⁻¹, Table 3-3). The Elfin Forest (average 16.4 Mg C ha⁻¹, Table 3-3), the pastures (5.4 Mg C ha⁻¹; [89]) as well as the subpáramo area (8.2 Mg C ha⁻¹; [90]) in no way approximate this high value.

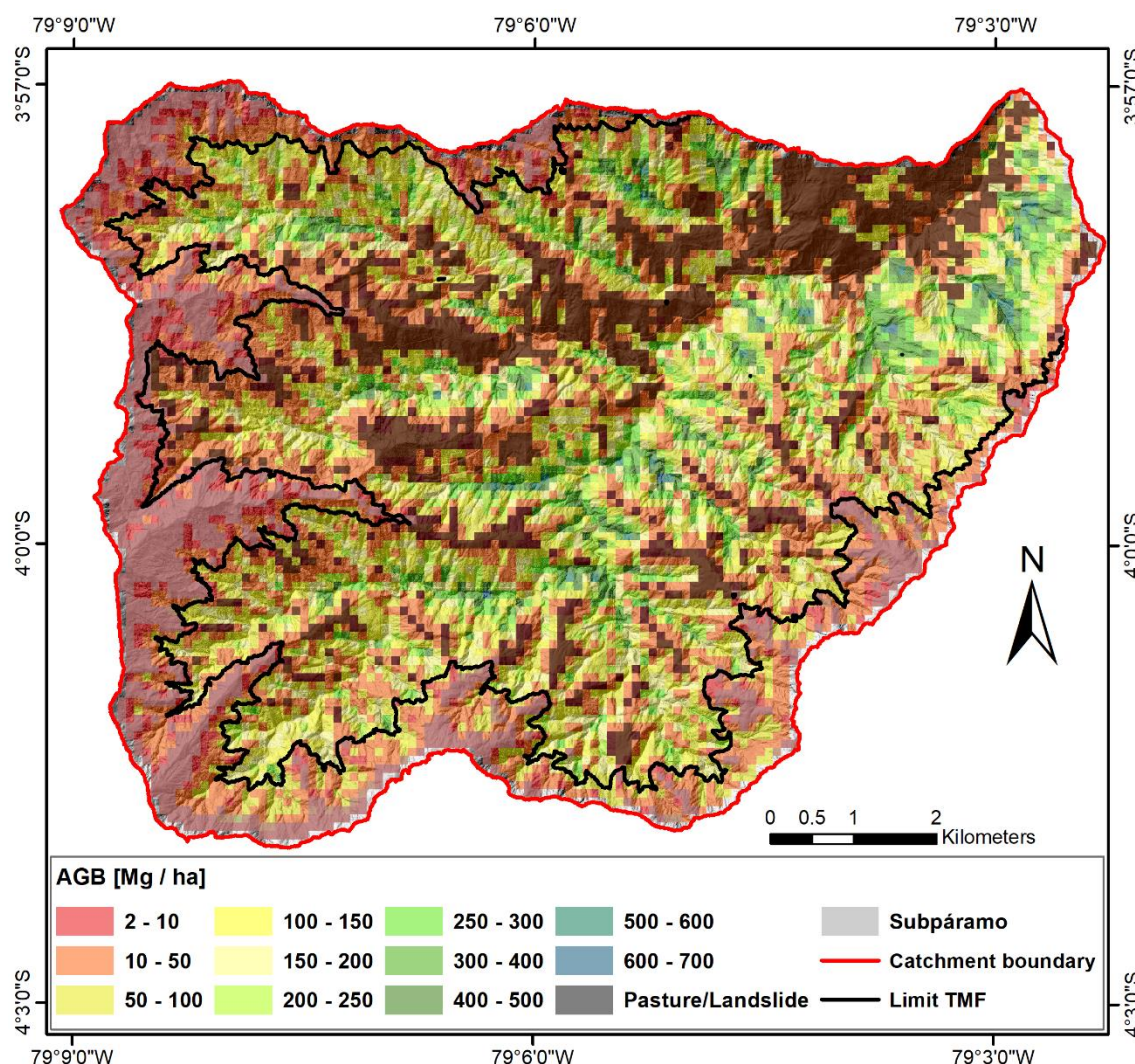


Figure 3-12: Spatial distribution of AGB in the Rio San Francisco catchment.

The total AGB for the whole study catchment was estimated at 565.3 Gg (C stock: 282.6 Gg C), in which the TMF contributes 489.3 Gg (C stock: 244.7 Gg C), 86.6% of the total amount, covering only 56.7% of the catchment area (Table 3-4). The Elfin Forest covers 18.8% of the catchment area and contributes 50.1 Gg (C stock: 25.0 Gg C), which is an 8.9% portion of the total AGB (C stock). The pasture sites only store 13.0 Gg (6.5 Gg C), representing 2.3% of the total AGB (C stock) amount, covering 14.8% of the catchment area. The subpáramo areas also account for 2.3% of the total AGB (12.9 Gg; C stock 6.4 Gg C) but only cover 9.7% of the watershed (Table 3-4). Taking only the natural forest ecosystems inside the study catchment into account, the TMF and the Elfin Forest contribute nearly 95.5% of the total AGB or C stock (Table 3-4).

Table 3-4: Portion of the individual vegetation units respective to the total catchment area, including total AGB and C stock.

Land Cover	Area [ha]	Area [%]	AGB [Mg]	C Stock [Mg C]	C Stock [%]
TMF	4608	56.7	489,343.6	244,671.8	86.6
Elfin Forest	1529	18.8	50,117.2	25,058.6	8.9
Pasture	1200	14.8	12,960.0	6480.0	2.3
Subpáramo	785	9.7	12,874.0	6437.0	2.3
TOTAL	8122	100.0	565,294.8	282,647.4	100.0

3.4 Discussion

The separation into ravine forest and ridge forest within the study catchment was also described in earlier investigations (e.g., [16,24,86]), which characterized the ravine forest by larger trees with concurrently higher basal areas (DBH) compared to the ridge forest, while also in the ridge forest, fewer tree species are observed. These investigations concluded that the forest structure is mainly due to the adverse climate conditions at the ridges (stronger winds, [75]) and the different soil types [73,74,107]. However, as this study showed, bigger trees can also be found at higher elevations and steeper slopes, if the site is protected by the surrounding terrain. This could only be determined using remote sensed data in high resolution, because most of these areas are inaccessible.

The mean WD of the TMF in the study catchment was estimated at 0.59 g cm^{-3} , which lies in the same range as other mean WD values reported for tropical forests in South America. For example, Chave et al. [18] presented mean WD values for Central and South America, sampling 2456 trees species and obtaining a mean value of 0.63 g cm^{-3} [15] calculated the same mean WD value (0.63 g cm^{-3}) estimating Amazon forest carbon density. However, taking only the available information from Mitchard et al. [15] for Ecuador into account, the mean WD is slightly lower (0.57 g cm^{-3}). This value was also applied by Gibbon et al. [108], investigating mean WD of a TMF in Peru and Spracklen and Righelato. [8], who estimated the AGB of another TMF in southern Ecuador. However, the field measurements determined WD between 0.16 g cm^{-3} and 0.92 g cm^{-3}

for the different tree species [86], from which the average WD was calculated and therefore this mean value (0.59 g cm^{-3}) should be more representative for the TMF in the San Francisco catchment.

The individual H in the TMF, as well as in the Elfin Forest, as obtained from the CHM and the individual tree classification, depends upon the forest type (ravine or ridge) and the degree of protection of the site. The average H values calculated in this study were similar to the values presented by Homeier et al. [86], who estimated an average tree height of 14.7 m for the ravine TMF and of 10.3 m for the ridge TMF (see Table 3-2). The small difference may be due to the slight underestimation of trees up to 15 m and over 25 m derived from the LiDAR data (Figure 3-6a). However, Werner and Homeier [25] presented notably higher average H values, estimated by means of field plot measurements at lower elevations using an ultrasonic tree height meter. They calculated an average tree height of 20.5 m for the lower ravine forest and 12.6 m for the lower ridge forest, which was confirmed by Leuschner et al. [24], who calculated 18.9 m for areas near the valley bottom and 12.0 m at higher elevations, without applying any distinction between the forest types. However, as Larjavaara and Muller-Landau [109] indicated, ultrasonic tree height meters in natural forests may produce errors of up to 20% due to the dense vegetation, which does not permit an undisturbed view up to the canopies and due to user errors. Furthermore, the mentioned variations in average H for the same forest stand are a result of the potential field plot distributions in natural TMF, which explains why the plots were installed at lower altitudes and under dense canopies without larger forest gaps ($<2 \text{ m}$; [25]) where trees are generally taller. As Gourlet-Fleury et al. [27] clarified, the accuracy of the calculated values depends upon the plot distribution and the spatial scale, which must be fine enough to capture the landscape variability. The same is valid for the maximum H, where the published values vary between 30.0 m and 40.0 m for this TMF and between 8.0 m and 9.0 m for the Elfin Forest (e.g., [16,24,28]). However, this study identified trees of up to 48.4 m in protected lower parts of the catchment and trees up to 15.7 m in the ravine Elfin Forest. Therefore, H and forest structure in TMF are hardly detectable by small field plots because of the local topography, the difficulty in access, the climate conditions and other disturbances, which change rapidly within small scales. The forest structure is better accessed by means of an individual tree classification, which can be derived from remote sensed LiDAR data in

high resolution and the derived topographic and morphometric indices (TPI and MPI; [29,67,101]).

The obtained individual H from the LiDAR data and the specific height-diameter relationship from the field data were used to calculate the DBH of each tree detected within the whole catchment (e.g., [92]). However, the accuracy of the height-diameter relationship depends on the model applied, the altitude, the climate conditions and the forest structure characteristics, as well as the location where the selected trees are sampled [49,110]. For tropical forests, only few investigations reported height-diameter relationships and the information about their performance is limited (e.g., [88,110]). In general, the height-diameter relationships vary significantly between regions because of the species composition and local climate and topographical conditions [49]. Only [93,111] presented coefficient of determination (R^2) values for their height-diameter relationships, which ranges between 0.5 and 0.9. The dataset used in this study to calculate the specific local height-diameter relationship includes all tree species present in the different plots, measured within the different forest types [25]. Therefore, the calculated local height-diameter relationship (R^2 : 0.60; p -value < 0.001; Figure 3-4) is acceptable, because it is representative for the two TMF types (ravine and ridge) considering the different tree species [112]. Additionally, the logarithmic data transformation and the linear regression analysis resulted in an improved correlation between H and DBH [88,93,94]. The determined relationship slightly overestimates the DBH of the trees, especially between 25 cm and 60 cm (Figure 3-6b), which also leads to a small overestimation of the AGB per tree (Figure 3-8), in conjunction with the applied average WD.

While, comparing the estimated DBH values of this study with DBH measurements carried out by other plot-based studies in the catchment, it can be stated that the obtained results lie within the same range, because trees of up to 200 cm were identified (e.g., [16]; Table 3-2). The maximum DBH depends on the species and the age of the trees, as well as on the position of the trees respective to the surrounding terrain [41,113]. Average DBH in the study area, as published by Leuschner and Moser [114], are notably lower (TMF: 9.8 cm to 12.2 cm; Elfin Forest: 7.2 cm) compared to the obtained values. The difference might be explained by the plot distribution, because at inaccessible sites no data can be collected and the LiDAR data includes information of each individual tree

detected. The individual tree classification applied here only considered dominant/codominant trees taller than 5 m with a DBH greater than 10 cm, in which smaller mid- and understory trees are often not detected because of higher canopies [42], which possibly increased the calculated average DBH for the forest stand. Nonetheless, the difference between TMF and Elfin Forest could be distinguished, which is due to harsher climate conditions at higher elevations, complicating the tree growth at these exposed positions (e.g., [73–75]). Therefore, the calculated mean values are representative for dominant/ codominant trees in the study catchment.

Highest AGB was calculated for the lower ravine TMF near the valley bottom and inside the side valleys, where protected and dense forest patches exist (664.1 Mg ha^{-1}). The AGB at the ridges are lower due to the more exposed position, which is why trees are smaller and do not accumulate much biomass and therefore do not contribute large amounts to the total AGB. In general, AGB at the ridge forests is reduced compared to the ravine forests (Table 3-2), because tree growth is inhibited. Additionally, the climate conditions become progressively harsher with increasing altitude [75], for which reason the Elfin Forest patches at the transition zone to the subpáramo area displayed even lower AGB (Figure 3-12). However, high AGB accumulations were also estimated at higher elevations inside the upper side valleys (up to 196.6 Mg ha^{-1} ; Elfin Forest), where the trees are specially protected by the surrounding terrain. In general, AGB for the Elfin Forest did not exceed 50.0 Mg ha^{-1} and mainly stayed below 20.0 Mg ha^{-1} , due to the unprotected topographic position which leads to smaller trees at these high altitudes.

The mean AGB for the TMF calculated in this study is notably lower than the values published by [16,24,25,115] for the same forest stand. These studies calculated mean AGB between 150 Mg ha^{-1} and 200 Mg ha^{-1} , based on data from field plots of $20 \text{ m} \times 20 \text{ m}$ at lower elevations under dense forest stands without larger forest gaps [25]. These field data were extrapolated to obtain a mean AGB for the whole study catchment but forest structure at higher elevations could not be included, due to the local topography, the difficulty in access, the climate conditions and natural disturbances (e.g., [3,27]). Taking into account only the trees of the lower TMF (up to 2100 m above sea level), the estimated mean AGB of this study increased to 151.6 Mg ha^{-1} , because trees are bigger at lower elevations. Above 2100 m above sea level, forest mean AGB decreased to 93.3 Mg ha^{-1} , because average H becomes lower and ridge forests dominate (Figure 3-7c).

These values are similar to the mean AGB published by Leuschner et al. [24], who calculated 163.2 Mg ha^{-1} at lower and 94.6 Mg ha^{-1} at higher elevations. Therefore, Richter and Moreira-Muñoz [28] classified the TMF into Lower Mountain Forest (LMF) and Upper Mountain Forest (UMF). Nonetheless, the calculated mean AGB for the whole TMF (106.2 ha^{-1} ; Table 3-3) is confirmed by Spracklen and Righelato [8], who estimated a similar mean AGB (104 Mg ha^{-1}) for a TMF in southern Ecuador by means of field plot measurements, which underlines the importance of an accurate field plot distribution to estimate AGB in natural forest stands.

Incidentally, the dominant/codominant trees within a forest stand represent 70% to 90% of the total AGB, as [41,105,106] indicated and therefore the inaccuracy of the present AGB estimation should be between 10% and 30%. This is verified by the comparison between the measured and calculated H, DBH and AGB values at tree level (Figures 3-6a,b and 3-8), in which the coefficients of determination ($R^2 > 0.91$) indicated a high accuracy for each parameter. Therefore, the overall error of the applied AGB estimation approach should lie between 12.5% and 24.0%, as also estimated by other studies taking into consideration sampling errors [8,21].

In summary, the natural forest stands, especially the TMF, store the majority of C (over 95%; Table 3-4), as has also been reported [4], which highlights the importance of intact forest ecosystems as C stocks. The pastures as well as the subpáramo area are negligible C stocks taking into consideration future anthropogenic CO_2 emissions [2,11]. However, the subpáramo areas, as well as the natural forest ecosystems (TMF and Elfin forest), provide another important service, being the water supply for the local and regional population (e.g., [116]). Therefore, the primary objective should be the protection of these natural ecosystems from human disturbance [4,6,7], while considering the possibility of additional greenhouse gas emissions caused by ongoing deforestation, which is especially problematic in the tropical mountains of Ecuador [9,13]. Also, reforestation programs, such as REDD+ [117] should be expedited, however, occasionally the efforts are complicated due to the changing and more extreme climatic conditions over pasture and agricultural lands (e.g., [81,82]).

3.5 Conclusions

The objective of the study was a reliable quantification of AGB and its distribution in a natural TMF in southern Ecuador using LiDAR data in combination with field measurements. In general, the applied method, based on a classification at tree level, allowed a reliable AGB estimation for the whole forest stand. Using high resolution LiDAR data in combination with field measurements, avoided high under- or overestimation of the AGB [46]. Furthermore, by means of the vegetation classification at tree level and the topographic (TPI) and morphometric (MPI) indices, the AGB distribution within the whole study catchment could be detected and analysed. The results showed that high AGB (Mg ha^{-1}) also exists at higher elevations if the site is protected by the surrounding terrain (ravine forest) but these areas are generally inaccessible, which explains why remote sensed data is necessary to detect the complete forest structure.

This indicates the importance of undisturbed natural forest ecosystems as C stocks, because over 95% of the total AGB is stored in the mountain forest ecosystems, especially in the ravine TMF, where the tallest trees are located. The pasture sites, as well as the subpáramo area, do not contribute much to the total AGB, because C is basically stored in woody vegetation (trunks and branches; for example, Reference [23]) and the woody plants of these vegetation units are generally small. However, the TMF as well as the subpáramo provide another important ecosystem service: the water supply for the population, which is non-negotiable with regards to ongoing deforestation. Therefore, protection of these natural ecosystems is the main issue for the development of the local population and concurrently for facing future GHG emissions.

Author Contributions: Víctor González-Jaramillo processed the LiDAR data, wrote and edited the manuscript. Andreas Fries gave advice on the research design, analysed the tree data and wrote the draft of the manuscript. Jörg Zeilinger provided the LiDAR raw data and revised the manuscript. Jürgen Homeier provided the tree data and revised the manuscript. Jhoana Paladines-Benitez gave advice on the statistics and revised the manuscript. Jörg Bendix gave advice on the research design and the methodology and also revised the manuscript.

Acknowledgments: This study was executed in framework with the DFG Research Unit 816: Biodiversity and Sustainable Management of Mega-diverse Mountain Ecosystems in South Ecuador (ALS under BE1780/17-2). The authors thank the German Research

Foundation DFG for funding the PhD of V. González-Jaramillo in the scope of the program “Bilateral Cooperation with South Ecuadorian Universities in Ecosystem Research” (BE1780-20-2; 27-2; 32-1). Thanks are also due to the collaboration of the Universidad Técnica Particular de Loja (UTPL) to facilitate this research and project PY1760, funded by the Smart Land initiative. Special thanks to Gregory Gedeon for text revision.

Conflicts of Interest: The authors declare no conflict of interest.

3.6 References

1. Kou, W.; Liang, C.; Wei, L.; Hernandez, A.J.; Yang, X. Phenology-based method for mapping tropical evergreen forests by integrating of MODIS and Landsat imagery. *Forests* 2017, 8, 34, doi:10.3390/f8020034.
2. Pan, Y.; Birdsey, R.A.; Fang, J.; Houghton, R.; Kauppi, P.E.; Kurz, W.A.; Phillips, O.L.; Shvidenko, A.; Lewis, S.L.; Canadell, J.G.; et al. A Large and Persistent Carbon Sink in the World's Forests. *Science* 2011, 333, 988–993, doi:10.1126/science.1201609.s.
3. Saatchi, S.S.; Harris, N.L.; Brown, S.; Lefsky, M.; Mitchard, E.T.A.; Salas, W.; Zutta, B.R.; Buermann, W.; Lewis, S.L.; Hagen, S.; et al. Benchmark map of forest carbon stocks in tropical regions across three continents. *Proc. Natl. Acad. Sci. USA* 2011, 108, 9899–9904, doi:10.1073/pnas.1019576108.
4. Häger, A.; Schwendenmann, L. Forest Carbon Sequestration and Global Change. In *The Paradigm of Forests and the Survival of the Fittest*; Molina-Murillo, S.A., Rojas, C., Eds.; CRC Press: Boca Raton, FL, USA; London, UK; New York, NY, USA, 2016; pp. 39–86, ISBN 978-1-4987-5106-3.
5. Ochoa-Cueva, P.; Fries, A.; Montesinos, P.; Rodríguez-Díaz, J.A.; Boll, J. Spatial Estimation of Soil Erosion Risk by Land-cover Change in the Andes of Southern Ecuador. *Land Degrad. Dev.* 2015, 26, 565–573, doi:10.1002/ldr.2219.
6. UNFCCC. Fact Sheet: Reducing Emissions from Deforestation in Developing Countries: Approaches to Stimulate Action; FAO: Rome, Italy, 2011.
7. Farmer, T.G. Modern Climate Change Science. An Overview of Today's Climate Change Science; Springer: LasCruces, NM, USA, 2015; pp. 1–40, ISBN 978-3-319-09222-5.
8. Spracklen, D.V.; Righelato, R. Carbon storage and sequestration of re-growing montane forests in southern Ecuador. *For. Ecol. Manag.* 2016, 364, 139–144, doi:10.1016/j.foreco.2016.01.001.
9. González-Jaramillo, V.; Fries, A.; Rollenbeck, R.; Paladines, J.; Oñate-Valdivieso, F.; Bendix, J. Assessment of deforestation during the last decades in Ecuador using NOAA-AVHRR satellite data. *Erdkunde* 2016, 70, 217–235, doi:10.3112/erdkunde.2016.03.02.
10. Franklin, J.; Serra-Diaz, J.M.; Syphard, A.D.; Regan, H.M. Global change and terrestrial plant community dynamics. *Proc. Natl. Acad. Sci. USA* 2016, 113, 3725–3734, doi:10.1073/pnas.1519911113.

11. Smith, P.; Bustamante, M.; Ahammad, H.; Clark, H.; Dong, H.; Elsiddig, E.A.; Haberl, H.; Harper, R.; House, J.; Jafari, M.; et al. Agriculture, Forestry and Other Land Use (AFOLU). In *Climate Change 2014: Mitigation of Climate Change; Contribution of Working Group III to the Fifth Assessment Report of the Intergovernmental Panel on Climate Change*; Edenhofer, O., Pichs-Madruga, R., Sokona, Y., Farahani, E., Kadner, S., Seyboth, K., Adler, A., Baum, I., Brunner, S., Eickemeier, P., et al., Eds.; Cambridge University Press: Cambridge, UK; New York, NY, USA, 2014; ISBN 978-1-107-65481-5.
12. Clark, M.L.; Roberts, D.A.; Ewel, J.J.; Clark, D.B. Estimation of tropical rain forest aboveground biomass with small-footprint lidar and hyperspectral sensors. *Remote Sens. Environ.* 2011, 115, 2931–2942, doi:10.1016/j.rse.2010.08.029.
13. Food and Agriculture Organization of the United Nations. *Global Forest Resources Assessment 2015 Desk Reference*; Food and Agriculture Organization of the United Nations: Rome, Italy, 2015.
14. Berenguer, E.; Ferreira, J.; Gardner, T.A.; Aragão, L.E.O.C.; De Camargo, P.B.; Cerri, C.E.; Durigan, M.; De Oliveira, R.C.; Vieira, I.C.G.; Barlow, J. A large-scale field assessment of carbon stocks in human-modified tropical forests. *Glob. Chang. Biol.* 2014, 20, 3713–3726, doi:10.1111/gcb.12627.
15. Mitchard, E.T.A.; Feldpausch, T.R.; Brien, R.J.W.; Lopez-Gonzalez, G.; Monteagudo, A.; Baker, T.R.; Lewis, S.L.; Lloyd, J.; Quesada, C.A.; Gloor, M.; et al. Markedly divergent estimates of Amazon forest carbon density from ground plots and satellites. *Glob. Ecol. Biogeogr.* 2014, 23, 935–946, doi:10.1111/geb.12168.
16. Paulick, S.; Dislich, C.; Homeier, J.; Fischer, R.; Huth, A. The carbon fluxes in different successional stages: Modelling the dynamics of tropical montane forests in South Ecuador. *For. Ecosyst.* 2017, 4, 5, doi:10.1186/s40663-017-0092-0.
17. Bhardwaj, D.R.; Banday, M.; Pala, N.A.; Rajput, B.S. Variation of biomass and carbon pool with NDVI and altitude in sub-tropical forests of northwestern Himalaya. *Environ. Monit. Assess.* 2016, 188, 635, doi:10.1007/s10661-016-5626-3.
18. Chave, J.; Muller-Landau, H.C.; Baker, T.R.; Easdale, T.A.; Steege, H.T.; Webb, C.O. Regional and phylogenetic variation of wood density across 2456 neotropical tree species. *Ecol. Appl.* 2006, 16, 2356–2367, doi:10.1890/1051-0761(2006)016[2356:RAPVOW]2.0.CO;2.
19. Vieilledent, G.; Vaudry, R.; Andriamanohisoa, S.F.D.; Rakotonarivo, O.S.; Randrianasolo, H.Z.; Razafindrabe, H.N.; Rakotoarivony, C.B.; Ebeling, J.; Rasamoelina, M. A universal approach to estimate biomass and carbon stock in

- tropical forests using generic allometric models. *Ecol. Appl.* 2012, 22, 572–583, doi:10.1890/11-0039.1.
20. Gao, X.; Li, Z.; Yu, H.; Jiang, Z.; Wang, C.; Zhang, Y.; Qi, L.; Shi, L. Modeling of the height–diameter relationship using an allometric equation model: A case study of stands of *Phyllostachys edulis*. *J. For. Res.* 2016, 27, 339–347, doi:10.1007/s11676-015-0145-6.
 21. Chave, J.; Andalo, C.; Brown, S.; Cairns, M.A.; Chambers, J.Q.; Eamus, D.; Fölster, H.; Fromard, F.; Higuchi, N.; Kira, T.; et al. Tree allometry and improved estimation of carbon stocks and balance in tropical forests. *Oecologia* 2005, 145, 87–99, doi:10.1007/s00442-005-0100-x.
 22. Brown, S. Estimating Biomass and Biomass Change of Tropical Forests: A Primer; Technical Report, FAO Forestry Paper 134; FAO: Rome, Italy, 1997.
 23. Ishihara, M.I.; Utsugi, H.; Tanouchi, H.; Aiba, M.; Kurokawa, H.; Onoda, Y.; Nagano, M.; Umehara, T.; Ando, M.; Miyata, R.; et al. Efficacy of generic allometric equations for estimating biomass: A test in Japanese natural forests. *Ecol. Appl.* 2015, 25, 1433–1446, doi:10.1890/14-0175.1.
 24. Leuschner, C.; Zach, A.; Moser, G.; Homeier, J.; Graefe, S.; Hertel, D.; Wittich, B.; Soethe, N.; Iost, S.; Röderstein, M.; et al. The Carbon Balance of Tropical Mountain Forests Along an Altitudinal Transect. In *Ecosystem Services, Biodiversity and Environmental Change in a Tropical Mountain Ecosystem of South Ecuador*, Ecological Studies; Bendix, J., Beck, E., Bräuning, A., Makeschin, F., Mosandl, R., Scheu, S., Wilcke, W., Eds.; Springer: Berlin, Germany, 2013; Volume 221, pp. 117–139, ISBN 978-3-642-38136-2.
 25. Werner, F.A.; Homeier, J. Is tropical montane forest heterogeneity promoted by a resource-driven feedback cycle? Evidence from nutrient relations, herbivory and litter decomposition along a topographical gradient. *Funct. Ecol.* 2015, 29, 430–440, doi:10.1111/1365-2435.12351.
 26. Ferraz, A.; Saatchi, S.; Mallet, C.; Jacquemoud, S.; Goncalves, G.; Silva A.A.; Soares, P.; Tomé, M.; Pereira, L. Airbone Lidar Estimation of Aboveground Forest Biomass in the Absence of Field Inventory. *Remote Sens.* 2016, 8, 653, doi:10.3390/rs8080653.
 27. Gourlet-Fleury, S.; Rossi, V.; Rejou-Mechain, M.; Freycon, V.; Fayolle, A.; Saint-André, L.; Cornu, G.; Gérard, J.; Sarrailh, J.M.; Flores, O.; et al. Environmental filtering of dense-wooded species controls above-ground biomass stored in African moist forests. *J. Ecol.* 2011, 99, 981–990, doi:10.1111/j.1365-2745.2011.01829.x.

28. Richter, M.; Moreira-Muñoz, A. Climatic heterogeneity and vegetation diversity in southern Ecuador investigated by phytoindication. *Rev. Peru. Boil.* 2005, 12, 217–238.
29. Toivonen J.M.; Gonzales-Inca, C.A.; Bader, M.Y.; Ruokolainen, K.; Kessler, M. Elevation Shifts in the Topographic Position of *Polylepis* Forest Stands in the Andes of Southern Peru. *Forests* 2018, 9, 7, doi:10.3390/f9010007.
30. Kane, V.R.; Lutz, J.A.; Cansler, C.A.; Povak, N.A.; Churchill, D.J.; Smith, D.F.; Kane, J.T.; North, P. Water balance and topography predict fire and forest structure patterns. *For. Ecol. Manag.* 2015, 338, 1–13, doi:10.1016/j.foreco.2014.10.038.
31. Paul, K.I.; Roxburgh, S.H.; Chave, J.; England, J.R.; Zerihun, A.; Specht, A.; Lewis, T.; Bennett, L.T.; Baker, T.G.; Adams, M.A.; et al. Testing the generality of above-ground biomass allometry across plant functional types at the continent scale. *Glob. Chang. Biol.* 2016, 22, 2106–2124, doi:10.1111/gcb.13201.
32. Kumar, L.; Mutanga, O. Remote sensing of above-ground biomass. *Remote Sens.* 2017, 9, 935, doi:10.3390/rs9090935.
33. Tan, K.; Piao, S.; Peng, C.; Fang, J. Satellite-based estimation of biomass carbon stocks for northeast China's forests between 1982 and 1999. *For. Ecol. Manag.* 2007, 240, 114–121, doi:10.1016/j.foreco.2006.12.018.
34. Qin, Y.; Xiao, X.; Wang, J.; Dong, J.; Ewing, K.; Hoagland, B.; Hough, D.J.; Fagin, T.D.; Zou, Z.; Geissler, G.L.; et al. Mapping annual forest cover in sub-humid and semi-arid regions through analysis of Landsat and PALSAR imagery. *Remote Sens.* 2016, 8, 933, doi:10.3390/rs8110933.
35. Jochem, A.; Hollaus, M.; Rutzinger, M.; Höfle, B.; Schadauer, K.; Maier, B. Estimation of aboveground biomass using airborne LiDAR data. In *Proceedings of the 10th International Conference on LiDAR Applications for Assessing Forest Ecosystems (Silvilaser 2010)*, Freiburg, Germany, 14–17 September 2010; p. 9.
36. Kim, E.; Lee, W.-K.; Yoon, M.; Lee, J.-Y.; Son, Y.; Abu Salim, K. Estimation of Voxel-Based Above-Ground Biomass Using Airborne LiDAR Data in an Intact Tropical Rain Forest, Brunei. *Forests* 2016, 7, 259. doi:10.3390/f7110259.
37. Bendix, J.; Rollenbeck, R.; Palacios, W.E. Cloud detection in the Tropics—A suitable tool for climate-ecological studies in the high mountains of Ecuador. *Int. J. Remote Sens.* 2004, 25, 4521–4540, doi:10.1080/01431160410001709967.
38. Posilero, M.A.V.; Paringit, E.C.; Argamosa, R.J.L.; Faelga, R.A.G.; Ibanez, C.A.G.; Zaragosa, G.P. Lidar—Based Canopy Cover Estimation Using Linear Regression Techniques. *J. Philipp. Geosci. Remote Sens. Soc.* 2016, 26–33.

39. Li, A.; Dhakal, S.; Glenn, N.F.; Spaete, L.P.; Shinneman, D.J.; Pilliod, D.S.; Arkle, R.S.; McIlroy, S.K. Lidar aboveground vegetation biomass estimates in shrublands: Prediction, uncertainties and application to coarser scales. *Remote Sens.* 2017, 9, 903, doi:10.3390/rs9090903.
40. Stephens, P.R.; Kimberley, M.O.; Beets, P.N.; Paul, T.S.H.; Searles, N.; Bell, A.; Brack, C.; Broadley, J. Airborne scanning LiDAR in a double sampling forest carbon inventory. *Remote Sens. Environ.* 2012, 117, 348–357, doi:10.1016/j.rse.2011.10.009.
41. Zhang, Z.; Cao, L.; She, G. Estimating forest structural parameters using canopy metrics derived from airborne LiDAR data in subtropical forests. *Remote Sens.* 2017, 9, 940, doi:10.3390/rs9090940.
42. McGaughey, R.J. FUSION/LDV: Software for LIDAR Data Analysis and Visualization, version 3.70; United States Department of Agriculture, Forest Service: Washington, DC, USA, 2018.
43. Piironen, R.; Heiskanen, J.; Maeda, E.; Viinikka, A.; Pellikka, P. Classification of tree species in a diverse African Agroforestry landscape using imaging spectroscopy and laser scanning. *Remote Sens.* 2017, 9, 875, doi:10.3390/rs9090875.
44. Ota, T.; Kajisa, T.; Mizoue, N.; Yoshida, S.; Takao, G.; Hirata, Y.; Furuya, N.; Sano, T.; Ponce-Hernandez, R.; Ahmed, O.S.; et al. Estimating aboveground carbon using airborne LiDAR in Cambodian tropical seasonal forests for REDD+ implementation. *J. For. Res.* 2015, 20, 484–492, doi:10.1007/s10310-015-0504-3.
45. Barnes, C.; Balzter, H.; Barrett, K.; Eddy, J.; Milner, S.; Suárez, J.C. Individual tree crown delineation from airborne laser scanning for diseased larch forest stands. *Remote Sens.* 2017, 9, 231, doi:10.3390/rs9030231.
46. Asner, G.P.; Mascaro, J. Mapping tropical forest carbon: Calibrating plot estimates to a simple LiDAR metric. *Remote Sens. Environ.* 2014, 140, 614–624, doi:10.1016/j.rse.2013.09.023.
47. Coomes, D.A.; Dalponte, M.; Jucker, T.; Asner, G.P.; Banin, L.F.; Burslem, D.F.R.P.; Lewis, S.L.; Nilus, R.; Phillips, O.L.; Phua, M.; et al. Area-based vs tree-centric approaches to mapping forest carbon in Southeast Asian forests from airborne laser scanning data. *Remote Sens. Environ.* 2017, 194, 77–88, doi:10.1016/j.rse.2017.03.017.
48. Duncanson, L.I.; Dubayah, R.O.; Cook, B.D.; Rosette, J.; Parker, G. The importance of spatial detail: Assessing the utility of individual crown information

- and scaling approaches for lidar-based biomass density estimation. *Remote Sens. Environ.* 2015, 168, 102–112, doi:10.1016/j.rse.2015.06.021.
49. Scaranello, M.A.S.; Alves, L.F.; Vieira, S.A.; Camargo, P.B.; Joly, C.A.; Martinelli, L.A. Height-diameter relationships of tropical Atlantic moist forest trees in Southeastern Brazil. *Sci. Agric.* 2012, 69, 26–37, doi:10.1590/S0103-90162012000100005.
 50. Slik, J.W.F.; Paoli, G.; McGuire, K.; Amaral, I.; Barroso, J.; Bastian, M.; Blanc, L.; Bongers, F.; Boundja, P.; Clark, C.; et al. Large trees drive forest aboveground biomass variation in moist lowland forests across the tropics. *Glob. Ecol. Biogeogr.* 2013, 22, 1261–1271, doi:10.1111/geb.12092.
 51. Asner, G.P.; Clark, J.K.; Mascaro, J.; Vaudry, R.; Chadwick, K.D.; Vieilledent, G.; Rasamoelina, M.; Balaji, A.; Kennedy-Bowdoin, T.; Maatoug, L.; et al. Human and environmental controls over aboveground carbon storage in Madagascar. *Carbon Balance Manag.* 2012, 7, 2, doi:10.1186/1750-0680-7-2.
 52. Lewis, S.L.; Sonké, B.; Sunderland, T.; Begne, S.K.; Lopez-Gonzalez, G.; van der Heijden, G.M.F.; Phillips, O.L.; Affum-Baffoe, K.; Baker, T.R.; Banin, L.; et al. Above-ground biomass and structure of 260 African tropical forests. *Philos. Trans. R. Soc. B* 2013, 368, 1625, doi:10.1098/rstb.2012.0295.
 53. El Hajj, M.; Baghdadi, N.; Fayad, I.; Vieilledent, G.; Bailly, J.-S.; Minh, D.H.T. Interest of Integrating Spaceborne LiDAR Data to Improve the Estimation of Biomass in High Biomass Forested Areas. *Remote Sens.* 2017, 9, 213, doi:10.3390/rs9030213.
 54. Carreiras, J.M.B.; Quegan, S.; Toan, T.L.; Minh, D.H.T.; Saatchi, S.S.; Carvalhais, N.; Reichsteine, M.; Scipal, K. Coverage of high biomass forests by the ESA BIOMASS mission under defense restrictions. *Remote Sens. Environ.* 2017, 196, 154–162, doi:10.1016/j.rse.2017.05.003.
 55. Leitold, V.; Keller, M.; Morton, D.C.; D Cook, B.; Shimabukuro, Y.E. Airborne lidar-based estimates of tropical forest structure in complex terrain: Opportunities and trade-offs for REDD+. *Carbon Balance Manag.* 2015, 10, doi:10.1186/s13021-015-0013-x.
 56. Asner, G.P.; Anderson, C.B.; Martin, R.E.; Knapp, D.E.; Tupayachi, R.; Sinca, F.; Malhi, Y. Landscape-scale changes in forest structure and functional traits along an Andes-to-Amazon elevation gradient. *Biogeosciences* 2014, 11, 843–856, doi:10.5194/bg-11-843-2014.
 57. Urbazaev, M.; Thiel, C.; Cremer, F.; Dubayah, R.; Migliavacca, M.; Reichstein, M.; Schmullius, C. Estimation of forest aboveground biomass and uncertainties by

- integration of field measurements, airborne LiDAR, and SAR and optical satellite data in Mexico. *Carbon Balance Manag.* 2018, 13, doi:10.1186/s13021-018-0093-5.
58. Baccini, A.; Goetz, S.J.; Walker, W.S.; Laporte, N.T.; Sun, M.; Sulla-Menashe, D.; Hackler, J.; Beck, P.S.A.; Dubayah, R.; Friedl, M.A.; et al. Estimated carbon dioxide emissions from tropical deforestation improved by carbon-density maps. *Nat. Clim. Chang.* 2012, 2, 182–185, doi:10.1038/nclimate1354.
 59. Spracklen, D.V.; Righelato, R. Tropical montane forests are a larger than expected global carbon Store. *Biogeosciences* 2014, 11, 2741–2754, doi:10.5194/bg-11-2741-2014.
 60. Girardin, C.A.J.; Farfan-Rios, W.; Garcia, K.; Feeley, K.J.; Jørgensen, P.M.; Murakami, A.A.; Pérez, L.C.; Seidel, R.; Paniagua, N.; Claros, A.F.F.; et al. Spatial patterns of above-ground structure, biomass and composition in a network of six Andean elevation transects. *Plant Ecol. Divers.* 2014, 7, 161–171, doi:10.1080/17550874.2013.820806.
 61. Mascaro, J.; Asner, G.P.; Muller-Landau, H.C.; van Breugel, M.; Hall, J.; Dahlin, K. Controls over aboveground forest carbon density on Barro Colorado Island, Panama. *Biogeosciences* 2011, 8, 1615–1629, doi:10.5194/bg-8-1615-2011, 2011.
 62. Raich, J.W.; Russell, A.E.; Kitayama, K.; Parton, W.J.; Vitousek, P.M. Temperature influences carbon accumulation in moist tropical forests. *Ecology* 2006, 87, 76–87, doi:10.5194/bg-8-1615-2011.
 63. Unger, M.; Homeier, J.; Leuschner, C. Effects of soil chemistry on tropical forest biomass and productivity at different elevations in the equatorial Andes. *Oecologia* 2012, 170, 263–274, doi:10.1007/s00442-012-2295-y.
 64. Homeier, J.; Hertel, D.; Camenzind, T.; Cumbicus, N.L.; Maraun, M.; Martinson, G.O.; Poma, L.N.; Rillig, M.C.; Sandmann, D.; Scheu, S.; et al. Tropical Andean forests are highly susceptible to nutrient inputs—Rapid effects of experimental N and P addition to an Ecuadorian Montane Forest. *PLoS ONE* 2012, 7, e47128, doi:10.1371/journal.pone.0047128.
 65. Fisher, J.B.; Malhi, Y.; Torres, I.C.; Metcalfe, D.B.; van de Weg, M.J.; Meir, P.; Silva-Espejo, J.E.; Huasco, W.H. Nutrient limitation in rainforests and cloud forests along a 3000 m elevation gradient in the Peruvian Andes. *Oecologia* 2013, 172, 889–902, doi:10.1007/s00442-012-2522-6.
 66. Leuschner, C.; Moser, G.; Bertsch, C.; Roderstein, M.; Hertel, D. Large altitudinal increase in tree root/shoot ratio in tropical mountain forests of Ecuador. *Basic Appl. Ecol.* 2007, 8, 219–230, doi:10.1016/j.baae.2006.02.004.

67. Riley, J.W.; Calhoun, D.L.; Barichivich, W.J.; Walls, S.C. Identifying Small Depressional Wetlands and Using a Topographic Position Index to Infer Hydroperiod Regimes for Pond-Breeding Amphibians. *Wetlands* 2017, 37, 325–338, doi:10.1007/s13157-016-0872-2.
68. Richter, M.; Beck, E.; Rollenbeck, R.; Bendix, J. The Study Area. In *Ecosystem Services, Biodiversity and Environmental Change in a Tropical Mountain Ecosystem of South Ecuador*, Ecological Studies; Bendix, J., Beck, E., Bräuning, A., Makeschin, F., Mosandl, R., Scheu, S., Wilcke, W., Eds.; Springer: Berlin, Germany, 2013; Volume 221, pp. 1–19, ISBN 978-3-642-38136-2.
69. Homeier, J.; Werner, F.A.; Gradstein, S.R.; Breckle, S.-W.; Richter, M. Potential vegetation and floristic composition of Andean forests in South Ecuador, with a focus on the RBSF. In *Gradients in a Tropical Mountain Ecosystem of Ecuador*; Beck, E., Bendix, J., Kottke, I., Makeschin, F., Mosandl, R., Eds.; Springer: Berlin, Heidelberg, 2008; Volume 198, pp. 87–100.
70. Bendix, J.; Beck, E. Spatial aspects of ecosystem research in a biodiversity hot spot of southern Ecuador—An introduction. *Erdkunde* 2009, 63, 305–308, doi:10.3112/erdkunde.2009.04.01.
71. Beck, E.; Makeschin, F.; Haubrich, F.; Richter, M.; Bendix, J.; Valerezo, C. The Ecosystem (Reserva Biológica San Francisco). In *Gradients in a Tropical Mountain Ecosystem of Ecuador*; Beck, E., Bendix, J., Kottke, I., Makeschin, F., Mosandl, R., Eds.; Springer: Berlin, Heidelberg, 2008; Volume 198, pp. 1–14.
72. Curatola Fernández, G.F.; Obermeier, W.A.; Gerique, A.; López Sandoval, M.F.; Lehnert, L.W.; Thies, B.; Bendix, J. Land cover change in the Andes of southern Ecuador-Patterns and drivers. *Remote Sens.* 2015, 7, 2509–2542, doi:10.3390/rs70302509.
73. Moser, G.; Leuschner, C.; Hertel, D.; Graefe, S.; Soethe, N.; Iost, S. Elevation effects on the carbon budget of tropical mountain forests (S Ecuador): The role of the belowground compartment. *Glob. Chang. Biol.* 2011, 17, 2211–2226, doi:10.1111/j.1365-2486.2010.02367.x.
74. Dislich, C.; Huth, A. Modelling the impact of shallow landslides on forest structure in tropical montane forests. *Ecol. Model.* 2012, 239, 40–53, doi:10.1016/j.ecolmodel.2012.04.016.
75. Wagemann, J.; Thies, B.; Rollenbeck, R.; Peters, T.; Bendix, J. Regionalization of wind-speed data to analyze tree-line wind conditions in the eastern Andes of southern Ecuador. *Erdkunde* 2015, 69, 13–19, doi:10.3112/erdkunde.2015.01.01.

76. Homeier, J.; Werner, F.A.; Gawlik, J.; Peters, T.; Diertl, K.H.J.; Richter, M. Plant Diversity and its Relevance for the Provision of Ecosystem Services. In *Ecosystem Services, Biodiversity and Environmental Change in a Tropical Mountain Ecosystem of South Ecuador*, Ecological Studies; Bendix, J., Beck, E., Bräuning, A., Makeschin, F., Mosandl, R., Scheu, S., Wilcke, W., Eds.; Springer: Berlin, Germany, 2013; Volume 221, pp. 100–118, ISBN 978-3-642-38136-2.
77. Aguirre-Mendoza, Z.; Aguirre, N.; Merino, B.; Ochoa, I. Los páramos del Parque Nacional Podocarpus: Una aproximación a su diversidad ecosistémica y florística. In *Cambio climático y Biodiversidad: Estudio de caso de los páramos del Parque Nacional Podocarpus*; Aguirre, N., Ojeda T., Eguiguren, E., Aguirre Z., Eds.; Edilaja: Loja, Ecuador, 2015; pp. 22–45.
78. Fries, A.; Rollenbeck, R.; Bayer, F.; Gonzalez, V.; Oñate-Valivieso, F.; Peters, T.; Bendix, J. Catchment precipitation processes in the San Francisco valley in southern Ecuador: Combined approach using high-resolution radar images and in situ observations. *Meteorol. Atmos. Phys.* 2014, 126, 13–29, doi:10.1007/s00703-014-0335-3.
79. Roos, K.; Bendix, J.; Curatola, G.; Gawlik, J.; Gerique, A.; Hamer, U.; Hildebrandt, P.; Knoke, T.; Meyer, H.; Pohle, P.; et al. Current Provisioning Services: Pasture Development and Use, Weeds (Bracken) and Management. In *Ecosystem Services, Biodiversity and Environmental Change in a Tropical Mountain Ecosystem of South Ecuador*, Ecological Studies; Bendix, J., Beck, E., Bräuning, A., Makeschin, F., Mosandl, R., Scheu, S., Wilcke, W., Eds.; Springer: Berlin, Germany, 2013; Volume 221, pp. 230–243, ISBN 978-3-642-38136-2.
80. Curatola Fernández, G.F.; Silva, B.; Gawlik, J.; Thies, B.; Bendix, J. Bracken fern frond status classification in the Andes of southern Ecuador: Combining multispectral satellite data and field spectroscopy. *Int. J. Remote Sens.* 2013, 34, 7020–7037, doi:10.1080/01431161.2013.813091.
81. Fries, A.; Rollenbeck, R.; Göttlicher, D.; Nauß, T.; Homeier, J.; Peters, T.; Bendix, J. Thermal structure of a megadiverse Andean mountain ecosystem in southern Ecuador and its regionalization. *Erdkunde* 2009, 63, 321–335, doi:10.3112/erdkunde.2009.04.03.
82. Fries, A.; Rollenbeck, R.; Nauß, T.; Peters, T.; Bendix, J. Near surface air humidity in a megadiverse Andean mountain ecosystem of southern Ecuador and its regionalization. *Agric. For. Meteorol.* 2012, 152, 17–30, doi:10.1016/j.agrformet.2011.08.004.
83. Bendix, J.; Rollenbeck, R.; Richter, M.; Fabian, P.; Emck, P. Climate. In *Gradients in a Tropical Mountain Ecosystem of Ecuador*; Beck, E., Bendix, J., Kottke, I.,

- Makeschin, F., Mosandl, R., Eds.; Springer: Berlin, Heidelberg, 2008; Volume 198, pp. 63–74.
84. Bendix, J.; Trachte, K.; Cermak, J.; Rollenbeck, R.; Nauß, T. Formation of Convective Clouds at the Foothills of the Tropical Eastern Andes (South Ecuador). *J. Appl. Meteorol. Climatol.* 2009, 48, 1682–1695, doi:10.1175/2009JAMC2078.1.
 85. Silva, B.; Bendix, J. Remote sensing of vegetation in a tropical mountain ecosystem: Individual tree-crown detection. *Proc. SPIE* 2013, 8893, 88930B-1–6, doi:10.1117/12.2029912.
 86. Homeier, J.; Breckle, S.-W.; Günter, S.; Rollenbeck, R.T.; Leuschner, C. Tree Diversity, Forest Structure and Productivity along Altitudinal and Topographical Gradients in a Species-Rich Ecuadorian Montane Rain Forest. *Biotropica* 2010, 42, 140–148, doi:10.1111/j.1744-7429.2009.00547.x.
 87. Li, Y.; Zhao, M.; Mildrexler, D.J.; Motesharrei, S.; Mu, Q.; Kalnay, E.; Zhao, F.; Li, S.; Wang, K. Potential and actual impacts of deforestation and afforestation on land surface temperature. *J. Geophys. Res.* 2016, 121, 14372–14386, doi:10.1002/2016JD024969.
 88. Gianico, V.; Laforteza, R.; Jhon, R.; Sanesi, G.; Pesola, L.; Chen, J. Estimating Stand Volume and Above-Ground Biomass of Urban Forest Using LiDAR. *Remote Sens.* 2016, 8, 339, doi:10.3390/rs8040339.
 89. Knoke, T.; Bendix, J.; Pohle, P.; Hamer, U.; Hildebrandt, P.; Roos, K.; Gerique, A.; Sandoval, M.L.; Breuer, L.; Tischer, A.; et al. Afforestation or intense pasturing improve the ecological and economic value of abandoned tropical farmlands. *Nat. Commun.* 2014, 5, 5612, doi:10.1038/ncomms6612.
 90. Eguiguren, P.; Aguirre, N.; Santín, A.; Vidal, E. Reservorios de carbono en los páramos del Parque Nacional Podocarpus. In *Cambio Climático y Biodiversidad: Estudio de caso de los Páramos del Parque Nacional Podocarpus*; Aguirre, N., Ojeda T., Eguiguren, E., Aguirre Z., Eds.; Ediloja: Loja, Ecuador, 2015; pp. 126–135.
 91. Levis, S.; Bonan, G.B.; Vertenstein, M.; Oleson, K.W. The Community Land Model's Dynamic Global Model (CLM-DGVM): Technical Description and User's Guide; National Center for Atmospheric Research: Boulder, Colorado, 2004.
 92. Spriggs, R.; Coomes, D.; Jones, T.; Caspersen, J.; Vanderwel, M. An Alternative Approach to Using LiDAR Remote Sensing Data to Predict Stem Diameter Distributions across a Temperate Forest Landscape. *Remote Sens.* 2017, 9, 944, doi:10.3390/rs9090944.

93. Djomo, A.N.; Chimi, C.D. Tree allometric equations for estimation of above, below and total biomass in a tropical moist forest: Case study with application to remote sensing. *For. Ecol. Manag.* 2017, 391, 184–193, doi: 10.1016/j.foreco.2017.02.022.
94. Nogueira, E.M.; Nelson, B.W.; Fearnside, P.M.; França, M.B.; Oliveira, Á.C.A. de Tree height in Brazil's "arc of deforestation": Shorter trees in south and southwest Amazonia imply lower biomass. *For. Ecol. Manag.* 2008, 255, 2963–2972, doi:10.1016/j.foreco.2008.02.002.
95. González-Ferreiro, E.; Diéguez-Aranda, U.; Barreiro-Fernández, L.; Buján, S.; Barbosa, M.; Suárez, J.C.; Bye, I.J.; Miranda, D. A mixed pixel- and region-based approach for using airborne laser scanning data for individual tree crown delineation in *Pinus radiata* D. Don plantations. *Int. J. Remote Sens.* 2013, 34, 7671–7690, doi:10.1080/01431161.2013.823523.
96. Edson, C.; Wing, M.G. Airborne Light Detection and Ranging (LiDAR) for Individual Tree Stem Location, Height, and Biomass Measurements. *Remote Sens.* 2011, 3, 2494–2528, doi:10.3390/rs3112494.
97. Shiota, H.; Tanaka, K.; Nagashima, K. LiDAR Data Analysis with Fusion/LDV for Individual Tree. *J. Biodivers. Manag. For.* 2017, 2017, 6, doi:10.4172/2327-4417.1000184.
98. Molto, Q.; Hérault, B.; Boreux, J.J.; Daullet, M.; Rousteau, A.; Rossi, V. Predicting tree heights for biomass estimates in tropical forests—A test from French Guiana. *Biogeosciences* 2014, 11, 3121–3130, doi:10.5194/bg-11-3121-2014.
99. SAGA GIS. System for Automated Geoscientific Analyses. Available online: <http://www.saga-gis.org> (accessed on 17 July 2017).
100. Moran, N.; Nieland, S.; Suntrup, G.T.; Kleinschmit, B. Combining machine learning and onlotigal data handling for multi-source classification for nature conservation areas. *Int. J. Appl. Earth Obs. Geoinf.* 2017, 54, 124–133, doi:10.1016/j.jag.2016.09.009.
101. Weiss, A.D. Topographic position and landforms analysis. Presented at the ESRI User Conference, San Diego, CA, USA, 9–13 July 2001; Volume 64, pp. 227–245. Available online: http://www.jennessent.com/downloads/TPI-poster-TNC_18x22.pdf (accessed on 10 June 2017).
102. Detto, M.; Muller-Landau, H.C.; Mascaro, J.; Asner, G.P. Hydrological Networks and Associated Topographic Variations as Templates for the Spatial Organization of Tropical Forest Vegetation. *PLoS ONE* 2013, 8, e76296, doi:10.1371/journal.pone.0076296.

103. Mauya, E.W.; Hansen, E.H.; Gobakken, T.; Bollandsas, O.M.; Malimbwi, R.E.; Naesset, E. Effects of field plot size on prediction accuracy of aboveground biomass in airborne laser scanning-assisted inventories in tropical rain forest of Tanzania. *Carbon Balance Manag.* 2015, 10, 10, doi:10.1186/s13021-015-0021-x.
104. Bunning, S.; McDonagh, J.; Rioux, J. Land Degradation Assessment in Drylands. Manual for Local Level Assessment of Land Degradation and Sustainable Land Management. Part 1. Planning and Methodological Approach, Analysis and Reporting; FAO: Rome, Italy, 2011; p. 163.
105. Kotowska, M.M.; Leuschner, C.; Triadiati, T.; Meriem, S.; Hertel, D. Quantifying above- and belowground biomass carbon loss with forest conversion in tropical lowlands of Sumatra (Indonesia). *Glob. Chang. Biol.* 2015, 21, 3620–3634, doi:10.1111/gcb.12979.
106. Bastin, J.-F.; Barbier, N.; Réjou-Méchain, M.; Fayolle, A.; Gourlet-Fleury, S.; Maniatis, D.; de Haulleville, T.; Baya, F.; Beeckman, H.; Beina, D.; et al. Seeing Central African forests through their largest trees. *Sci. Rep.* 2015, 5, 13156, doi:10.1038/srep13156.
107. Richter, M.; Diertl, K.H.; Peters, T.; Bussmann, R.W. Vegetation Structures and Ecological Features of the Upper Timberline Ecotone. In *Gradients in a Tropical Mountain Ecosystem of Ecuador*; Beck, E., Bendix, J., Kottke, I., Makeschin, F., Mosandl, R., Eds.; Springer: Berlin, Heidelberg, 2008; Volume 198, pp. 123–146.
108. Gibbon, A.; Silman, M.R.; Malhi, Y.; Fisher, J.B.; Meir, P.; Zimmermann, M.; Dargie, G.C.; Farfan, W.R.; Garcia, K.C. Ecosystem Carbon Storage Across the Grassland-Forest Transition in the High Andes of Manu National Park, Peru. *Ecosystems* 2010, 13, 1097–1111, doi:10.1007/s10021-010-9376-8.
109. Larjavaara, M.; Muller-Landau, H.C. Measuring tree height: A quantitative comparison of two common field methods in a moist tropical forest. *Methods Ecol. Evol.* 2013, 4, 793–801, doi:10.1111/2041-210X.12071.
110. Feldpausch, T.R.; Banin, L.; Phillips, O.L.; Baker, T.R.; Lewis, S.L.; Quesada, C.A.; Affum-Baffoe, K.; Arets, E.J.M.M.; Berry, N.J.; Bird, M.; et al. Height-diameter allometry of tropical forest trees. *Biogeosciences* 2011, 8, 1081–1106, doi:10.5194/bg-8-1081-2011.
111. Rahman, M.Z.A.; Bakar, M.A.A.; Razak, K.A.; Rasib, A.W.; Kanniah, K.D.; Kadir, W.H.W.; Omar, H.; Faidi, A.; Kassim, A.R.; Latif, Z.A. Non-destructive, laser-based individual tree aboveground biomass estimation in a tropical rainforest. *Forests* 2017, 8, 86.

112. González-Ferreiro, E.; Diéguez-Aranda, U.; Miranda, D. Estimation of stand variables in *Pinus radiata* D. Don plantations using different LiDAR pulse densities. *Forestry* 2012, 85, 281–292, doi:10.1093/forestry/cps002.
113. Zhang, C.; Wei, Y.; Zhao, X.; von Gadow, K. Spatial Characteristics of Tree Diameter Distributions in a Temperate Old-Growth Forest. *PLoS ONE* 2013, 8, e58983, doi:10.1371/journal.pone.0058983.
114. Leuschner, C.; Moser, G. Carbon Allocation and productivity in tropical mountain forest. In *The Tropical Mountain Forest. Patterns and Process in a Biodiversity Hotspot; Biodiversity and Ecology Series; Gradstein S.R., Homeier, J., Gansert, D., Eds., Universitätsverlang Göttingen: Göttingen, Germany, 2008; Volume 2, pp. 109–128.*
115. Dislich, C.; Günter, S.; Homeier, J.; Schröder, B.; Huth, A. Simulating forest dynamics of a tropical montane forest in South Ecuador. *Erdkunde* 2009, 63, 347–364, doi:10.3112/erdkunde.2009.04.05.
116. Flores-López, F.; Galaitsi, S.E.; Escobar, M.; Purkey, D. Modeling of Andean páramo ecosystems' hydrological response to environmental change. *Water (Switzerland)* 2016, 8, 94, doi:10.3390/w8030094.
117. MAE. Mecanismo REDD+ en Ecuador Introduce Material Informativo. Available online: <http://www.ambiente.gob.ec/mecanismo-redd-en-ecuador-introduce-material-informativo/> (accessed on 5 May 2017).

4 AGB Estimation in a Tropical Mountain Forest (TMF) by Means of RGB and Multispectral Images Using an Unmanned Aerial Vehicle (UAV)

This chapter is published in *Remote Sens.* 2019, **11**(12):1413

Received: 02 May 2019 / **Accepted:** 07 June 2019

AGB Estimation in a Tropical Mountain Forest (TMF) by Means of RGB and Multispectral Images Using an Unmanned Aerial Vehicle (UAV)

Víctor González-Jaramillo, Andreas Fries and Jörg Bendix

Abstract: The present investigation evaluates the accuracy of estimating above-ground biomass (AGB) by means of two different sensors installed onboard an unmanned aerial vehicle (UAV) platform (DJI Inspire I) because the high costs of very high-resolution imagery provided by satellites or light detection and ranging (LiDAR) sensors often impede AGB estimation and the determination of other vegetation parameters. The sensors utilized included an RGB camera (ZENMUSE X3) and a multispectral camera (Parrot Sequoia), whose images were used for AGB estimation in a natural tropical mountain forest (TMF) in Southern Ecuador. The total area covered by the sensors included 80 ha at lower elevations characterized by a fast-changing topography and different vegetation covers. From the total area, a core study site of 24 ha was selected for AGB calculation, applying two different methods. The first method used the RGB images and applied the structure for motion (SfM) process to generate point clouds for a subsequent individual tree classification. Per the classification at tree level, tree height (H) and diameter at breast height (DBH) could be determined, which are necessary input parameters to calculate AGB (Mg ha^{-1}) by means of a specific allometric equation for wet forests. The second method used the multispectral images to calculate the normalized difference vegetation index (NDVI), which is the basis for AGB estimation applying an equation for tropical evergreen forests. The obtained results were validated against a previous AGB estimation for the same area using LiDAR data. The study found two major results: (i) The NDVI-based AGB estimates obtained by multispectral drone imagery were less accurate due to the saturation effect in dense tropical forests, (ii) the photogrammetric approach using RGB images provided reliable AGB estimates comparable to expensive LiDAR surveys (R^2 : 0.85). However, the latter is only possible if an auxiliary digital terrain model (DTM) in very high resolution is available because in dense natural forests the terrain surface (DTM) is hardly detectable by passive sensors due to the canopy layer, which impedes ground detection.

Keywords: forest AGB; UAV; RGB data; multispectral data

4.1 Introduction

Accurate information about forest cover, land use and above-ground biomass (AGB) are critical parameters for many environmental studies as well as for conservation initiatives concerning the mitigation of global warming, such as REDD+ (Reducing emissions from deforestation and forest degradation and the role of conservation, sustainable management of forests and enhancement of forest carbon stocks in developing countries) [1,2]. By means of such data and their temporal development, the most vulnerable regions can be determined, and areas which deserve protection can be identified. In particular, natural forest cover is of utmost concern because it stores and sequesters large amounts of atmospheric carbon (nearly 30% of the cumulative anthropogenic emissions [3]) [4–6]. However, the high deforestation rates observed in tropical countries complicate mitigation actions and efforts. Furthermore, affected areas become sources of additional greenhouse gas (GHG) emissions [7,8], amplifying the global change [9].

The highest deforestation rates in South America were estimated in Ecuador [7,10], where specifically the tropical mountain forest (TMF) has been and is still affected for several reasons, such as population growth, economic crises, and planning processes [11,12]. During the last few decades, human activities changed the natural vegetation cover [13,14], mostly by slash-and-burn activities to produce pasture and agricultural land [15]. Therefore, carbon storage or AGB has changed, caused additionally by the extraction of desirable timber species, which is why natural forest cover is often disturbed or fragmented [16,17]. The AGB stock mostly consists of wood and branches of the different species (70% to 90% of AGB) [18,19] in which large or dominant trees (~25–30 m) contain more than 75% of total carbon stored [20]. Therefore, the determination of actual forest cover and AGB in high resolution is necessary to provide accurate data about existing carbon storage, which is the basis for future scenarios of potential C-sequestration or emission under environmental changes in the future [21].

To fulfill this requirement, information in very high resolution (cm) is necessary, which is especially challenging in TMF due to the high biodiversity, difficulties in access, and the fast-changing forest structure [22,23]. Remote sensing platforms provide a solution [24–27] because this technology offers information in very high resolutions and is independent of topographic conditions [28,29]. The best remote sensing alternative is

“light detection and ranging” (LiDAR) [30], a laser technology with an extremely high resolution, which provides 3D data suitable for a wide range of applications, including AGB estimation [31–33]. However, this technology is expensive and generally inaccessible for developing countries [8], requiring that other more cost-effective platforms must be considered.

Optical satellite data in very high spatial resolution can also provide the required information (e.g., platforms: WorldView, GeoEye, IKONOS, QuickBird, Pleiades) [34], but these sensors are sensitive to weather conditions (e.g., cloudiness [35]), besides the elevated costs for very high-resolution image acquisition [36]. Nonetheless, coarse to moderate resolution satellite images facilitate temporal information and historical data, at least for the last few decades (NOAA-AVHRR, Aster, MODIS or Landsat) [37–39]. This information can be used for forest classification, forest cover determination, and deforestation rate estimation [25,40] but hardly for accurate local AGB calculation and natural TMF monitoring due to high cloudiness and the fast-changing topography in tropical high mountains [41].

A third, more accessible technology is drones or unmanned aerial vehicles (UAV), which allow for the detection of surface data in very high spatial and temporal resolution [42–44]. The available sensors can provide 3D and multispectral information [4,45], which permit AGB estimation as well as ecosystem monitoring at small scale [28]. However, the range of UAVs is limited due to their battery capacity. At the same time, the image resolution as well as surface coverage depend on UAV flight height (ground sample distance - GSD) [2]. Nonetheless, UAVs have demonstrated their potential to complement or fill the gaps in more expensive surveys, like LiDAR [45,46]. As Weber and Lerch [47] stated, the accuracy level of photogrammetric products generated by means of UAV data is acceptable for relatively small areas where high resolution information is required (centimeter level).

According to our knowledge, AGB estimation by means of UAV data has not been applied in remote natural TMF. Thus, this study applies two different methods for AGB estimation in a remote TMF ecosystem in Southern Ecuador, using a UAV (DJI Inspire 1) [48] equipped with an RGB camera and a multispectral sensor. On the one hand, the RGB data were utilized to obtain 3D point-clouds [45] from which a digital terrain model

(DTM), a digital surface model (DSM), as well as a canopy height model (CHM) were generated and an individual tree classification executed. By means of the individual tree parameters, the specific allometric equation for tropical wet forest proposed by Chave et al. [49] was applied to estimate the AGB (Mg ha^{-1}). On the other hand, the Red and NIR bands of the multispectral sensor were used to calculate the normalized difference vegetation index (NDVI), which is the basis for AGB estimation applying the equation for evergreen forest proposed by Das and Singh [50]. Finally, the results of the two methods were evaluated comparing the obtained UAV AGB with an independent reference AGB dataset derived from LiDAR data for the same area [8].

4.2 Materials and Methods

4.2.1 Study Area

The study was executed in a natural TMF in the eastern escarpment of the South Ecuadorian Andes, specifically inside the San Francisco watershed, where the research station “Estación Científica San Francisco” (ECSF: Lat. $3^{\circ}58'18''$ S, long. $79^{\circ}4'45''$ W) is located. Altitudes range from 1600 m above sea level at the river outlet to 3200 m above sea level at the highest mountain peaks (Figure 4-1). The San Francisco watershed has an extension of $\sim 85 \text{ km}^2$ and is a hotspot for biodiversity due to its extraordinary variety of flora and fauna [51,52]. The natural TMF covers the slopes from the valley bottom up to the tree line (~ 2700 m above sea level) [12,53] and can be divided into lower slope (ravine) forest and upper slope (ridge) forest [54]. This natural forest structure is related to topography, climatic conditions, and prevailing soil types [55,56]. The ravine forest is characterized by lower stem density but higher basal areas (diameters) and canopy heights compared to the ridge forest, which also contains fewer tree species [8,22]. The selected study site has an area of 80 ha and is located at lower elevations (1700 m above sea level to 2200 m above sea level), including ravine and ridge forest areas (Figure 4-1).

The climate within the study area is per-humid with marked altitudinal gradients in air temperature, air humidity [57,58], cloudiness [59], rainfall [60], and wind conditions [56]. Mean annual air temperature ranges from 19.4°C at the valley bottom to 9.4°C at the mountain tops, whereas average relative humidity varies between 70% at the valley

bottom and at open sites to nearly 100% at the mountain ridges and inside the TMF. Precipitation shows a clear annual cycle with a main rainy season in austral winter (between May and September) and a relative dry season in austral summer (between November and February). Wind direction is predominately from the east due to the tropical easterlies, reaching average monthly velocities up to 15.5 m s^{-1} at the ridges in austral winter [61].

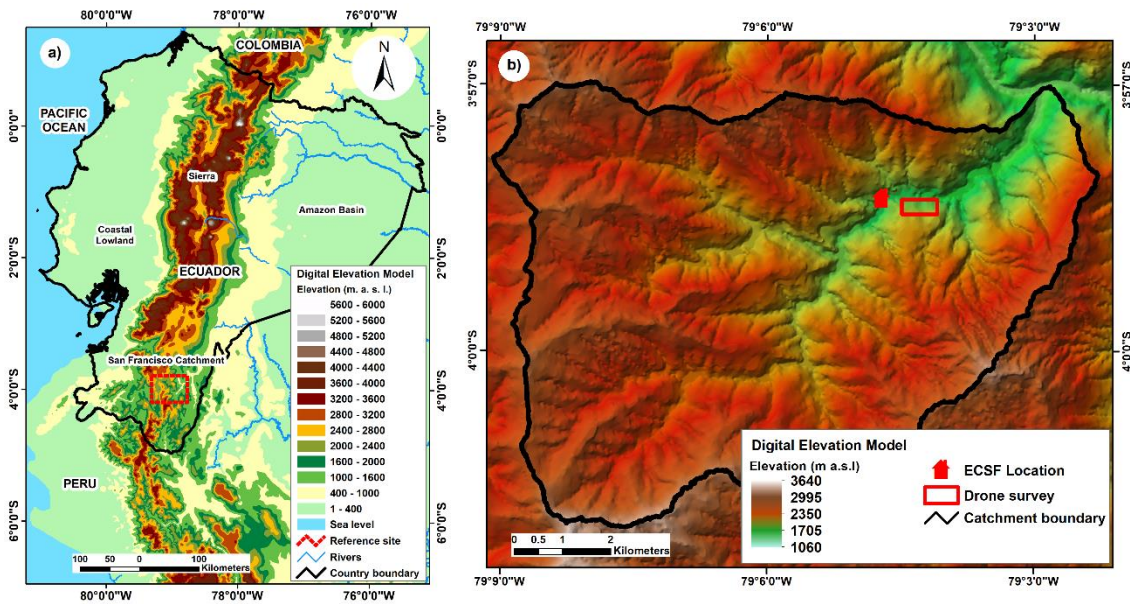


Figure 4-1: (a) Digital elevation model (DEM) of Ecuador, and (b) DEM of the San Francisco catchment including the study area.

4.2.2 Equipment

To estimate the AGB in the natural TMF, the UAV DJI Inspire 1 [48] was used, which was equipped with an RGB camera (ZENMUSE X3) and a multispectral camera (Parrot Sequoia) [62].

4.2.2.1 DJI Inspire 1

The UAV DJI Inspire 1 is a multi-rotor drone with 4 electric motors (quadcopter, Figure 4-2) that includes a remote controller that operates up to 2 km (radio) under unobstructed environmental and undisturbed meteorological conditions [48]. The maximum speed of the drone is 22 m s^{-1} , and its maximum operation altitude is 4500 m above sea level. Factory built, the DJI Inspire 1 is equipped with the RGB ZENMUSE X3 camera with a resolution of 12 megapixels, which also includes an integrated gimbal system that

provides stability and avoids distortion and blurring. The flight time varies with respect to payload, altitude above sea level, and weather conditions (mainly wind speed) but generally lies between 12–18 min. By considering the additional weight of a multispectral sensor and its external battery (approximately 250 g), an average flight time of about 10 min could be achieved for the mountainous environment in the study area.



Figure 4-2: Unmanned aerial vehicle (UAV) DJI Inspire 1, equipped with the RGB camera ZENMUSE X3 and the multi-spectral camera Parrot Sequoia.

4.2.2.2 Parrot Sequoia

The Parrot Sequoia camera is a multispectral sensor [62] that allows for the capture of imagery at 4 specific bands within the visible and infrared electromagnetic spectrum: Green (550 nm), red (660 nm), red edge (735 nm), and near infrared (790 nm). Furthermore, the camera includes a sunshine module that automatically calibrates the received images to compensate for the variability in sunlight conditions during flight as well as during different campaigns [63]. The specific bands of the Parrot Sequoia camera are similar to multispectral sensors onboard Landsat and NOAA-AVHRR satellites, allowing for comparable investigations to be conducted [62].

4.3 Methodology

4.3.1 Flight Planning and Data Acquisition

Depending on the size of study area, specific characteristics of the employed UAV must be considered (especially payload and resulting flight time) to determine the area covered by one single flight as well as the number of flights necessary to cover the whole area of interest. For the present research, a core site of 24 ha was selected, located at lower elevations in the San Francisco catchment, including parts of the valley bottom (river), side valleys, and ridges covered by natural TMF in which small gaps of natural succession (ancient landslides, grassland, and scrubs) are also present (Figure 4-3). To ensure complete coverage of the core site, the limits for data acquisition (vertical photographs) were extended at all borders (total area of coverage: 80 ha).

The flight characteristics were configured by means of the free software Precision Flight [64], an application that runs on an Android device that afterwards automatically executes the planned survey. The flight path was designed in an east-west direction with a nominal speed of 9 m s^{-1} to cover the whole area (80 ha) by two flights of approximately 10 min. The data were taken at a flight height of 300 m above the starting point with 90% side and forward overlap of the images, as recommended by the Pix4D documentation for locations with fast-changing topography and forests with dense canopies, to obtain enough points for individual image matching [65].

To improve the accuracy of the obtained images (coordinates X, Y and Z), ground control points (GCPs, Figure 4-3) were set within the area of coverage before executing the flights [28,66]. A minimum of 3 GCPs are necessary to ensure reliable image accuracy, but five to 10 GCPs are more suitable, particularly for larger areas [67]. It has been proven that a higher number of GCPs do not improve the final product significantly, nor do they improve the image accuracy [68], so for this reason six GCPs were set for the present study. The GCPs were located at flat open sites inside the total area (80 ha) to guarantee easy detection within the images. Therefore, dense canopies, steep slopes, and positions too close to the borders were avoided because the local topography as well as the camera position modifies the nadir angles of the different objects [29]. The exact geographical position of the GCPs (Figure 4-3) were determined using a GPS Trimble R6 system. Furthermore, the multispectral camera needs a radiometric calibration target to guarantee

reliable values for each individual spectral band. Therefore, an AirInov target, specifically designed for the Parrot Sequoia camera, was used to calibrate the bands before flight execution. More information about the target and its application can be found in [63].



Figure 4-3: Drone-based orthophoto of the selected study area, including the starting point, ground control points (GCP), and validation transects (yellow) inside the core area (rectangle).

The UAV flights were executed under sunny weather conditions during 26 April 2018, before the main rainy season started. During the survey, 132 RGB images and 230 multispectral images were obtained, which resulted in a total raw data size of 8 GB.

4.3.2 Data Processing

The data processing chain for AGB estimation by means of the RGB and multispectral images is shown in Figure 4-4. Both image types were analyzed independently.

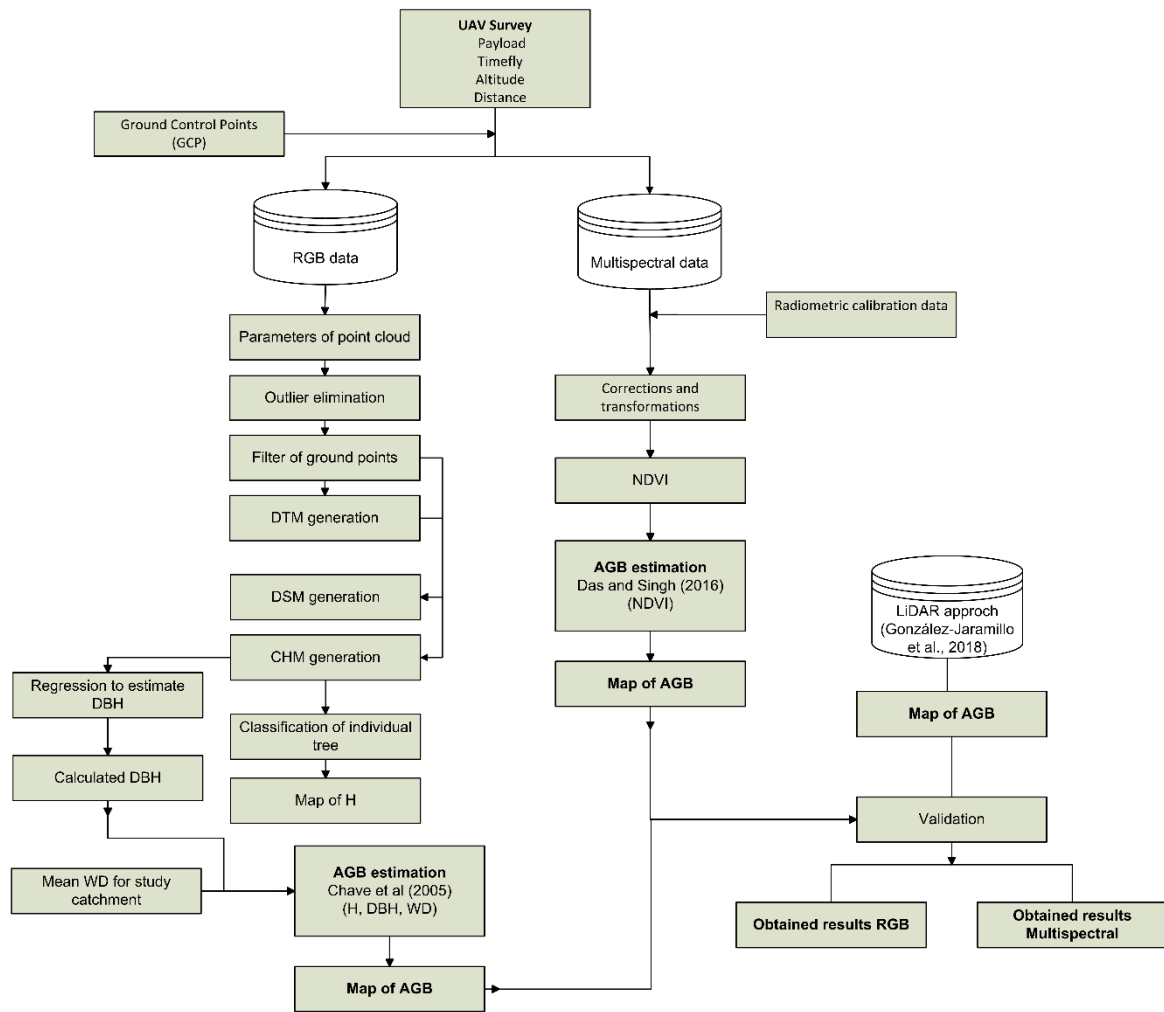


Figure 4-4: Processing chain to estimate above-ground biomass AGB (Mg ha^{-1}) using RGB (left) and multispectral imagery (right).

4.3.2.1 AGB Estimation by Means of RGB Data - Use of Photogrammetry

Allometric equations are widely used for AGB estimation [69–71] because they include forest structure parameters, such as tree height (H), tree diameter at breast height (DBH), and wood density (WD). The required information at tree level can be obtained by remote sensed data (H and DBH) and non-destructive field measurements (H, DBH, and WD), which do not harm the ecosystem [8,72]. For individual H detection, 3D data (point clouds) are required, which can be derived from expensive LiDAR surveys [73] but also from RGB data when applying computational photogrammetric techniques [1,74].

To obtain the 3D data, first, the raw data of the ZENMUSE X3 camera were checked and all images at the beginning and at the end of each individual flight eliminated because

these images do not comply with the established flight characteristics (flight height, image overlap, and pixel resolution). The revised dataset included 132 images, which were used to generate an orthophoto (Figure 4-3) and a point cloud for the whole study area (Figure 4-5). The remaining images were processed using the Pix4D software [65], which uses the structure from motion (SfM) process [75]. This process applies the principles of traditional stereoscopic photogrammetry in which the horizontal and vertical position of specific geometrical features are determined using several images of the same object taken under different viewing angles [74]. This can be done by means of a series of RGB images with a side and forward overlap of between 60% and 90%. For the present study, an overlap of 90% was fixed to avoid mismatches during the overlap process of the images. Furthermore, the fast-changing topography and forest structure in the study area requires a higher overlap to obtain enough points for image matching [65].

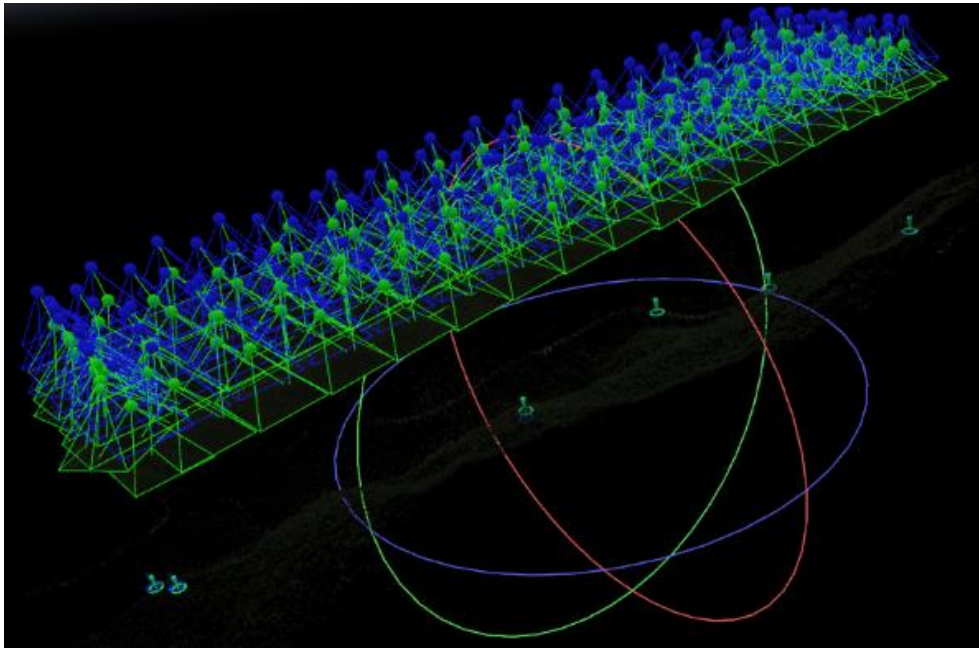


Figure 4-5: Data processing of the 132 RGB images in Pix4D (SfM), where dots in blue and green represent the individual photos and their overlap. GCPs are shown below.

As Aasen et al. [28] stated, the SfM processing provides a high geometric fidelity if the obtained/captured images contain the exact geographical position and orientation of the spectral sensor. These conditions are given for the present study because sensor orientation is implemented in the ZENMUSE X3 camera (orientation), and the DJI

Inspire 1 drone includes an on-board inertial measurement unit (IMU) sensor receiving GNSS signals (geographical position) [48]. As mentioned before, to improve the accuracy of the resulting images, six GCPs were set within the study area, which guarantees reliable image accuracy [76]. The location of the GCPs was introduced in the photogrammetric process, which identifies the specific GCP in each individual image and merges the image accordingly. The six GCPs were identified in 120 images, which is why a high geometric fidelity of the resulting information can be assumed [28,67].

In general, the workflow of the SfM approach consists of three major steps: (i) Feature extraction, (ii) feature matching, and (iii) reconstruction. Most of the processing time is needed for feature matching [76]. The software overlaps all available images and generates 3D-point clouds by means of the different angle views of the individual images [65,76]. Therefore, sufficient GCPs are necessary, especially in primary forests, to obtain reliable image matching [66]. The obtained point cloud was reduced to the core study site, located in the center of the investigation area. The Pix4D software also generates an orthophoto whose resolution depends on flight altitude (here: 300 m above ground). The programmed flight characteristics resulted in a pixel size (GSD) of about 25 cm for the orthophoto (see Figure 4-3) and the 3D point cloud (Figure 4-5).

To obtain H and DBH estimates for individual trees, the 3D point cloud was processed according to the method presented by González-Jaramillo et al. [8]. From the 3D point cloud, a digital terrain model (DTM) and a digital surface model (DSM) were created, in which the DTM model can be interchanged with any other DTM in very high resolution available for the study area [77]. The utilized software (Fusion 3.7) [78] subtracts the DTM from the DSM to obtain a canopy height model (CHM), which displays the difference between the ground (terrain, bare-earth points) and the highest elevation returns for each GSD [79]. In this case, the CHM depicts the vegetation height while the Canopy Maxima method was also applied within a variable-size evaluation window (here: 3×3) [80] to estimate individual H of dominant trees, which represent 70% to 90% of the total AGB of a forest stand [18,19]. For this study, only dominant trees higher than 5 m with a DBH greater than 10 cm were considered to calculate the AGB, as Gianico et al. [79] recommended.

The H of the individual trees detected was used to calculate the DBH based on the height-diameter relationship equation established by González-Jaramillo et al. [8] for the same study area (Equation (1)),

$$DBH = e^{\left(\frac{\ln(H)-0.85}{0.56}\right)} \quad (1)$$

where DBH is the diameter at breast height in cm, and H is the estimated height of the tree (m), obtained from the point cloud.

To estimate the AGB ($Mg\ ha^{-1}$), mean WD from a previous investigation was used, which was obtained by means of field measurements taken in the study area ($0.59\ g\ cm^{-3}$) [81]. The applied AGB equation at tree level corresponds to Chave et al. [49], who suggested a specific equation for tropical wet forest, which can be written as follows (Equation (2)),

$$\begin{aligned} AGB_{tree} &= \exp(-2.557 + 0.940 \times \ln(WD * D^2 * H)) \\ &= 0.0776 \times (WD * D^2 * H)^{0.940} \end{aligned} \quad (2)$$

where AGB_{tree} corresponds to the AGB of a specific tree (Mg), WD represents the wood density average ($gr\ cm^{-3}$), H is the obtained height of each detected tree (m) and D is the estimated DBH (cm) obtained by means of Equation (1). The product applying Equation (2) is the AGB per individual tree. Finally, a grid layer with a $1\ ha \times 1\ ha$ resolution was overlaid to determine AGB per hectare, where all individual tree AGB was added up for each grid cell [8].

4.3.2.2 AGB Estimation Using Multispectral Data

To estimate AGB by means of the multispectral data obtained from the Parrot Sequoia camera, the equation proposed by Das and Singh [50] was applied. They presented a specific equation for different tropical forest types. The selected equation corresponds to tropical evergreen forest, which is comparable to the forest type presented in the study area. The raw data with a spatial resolution of 25 cm (multispectral imagery) were processed using the Pix4D software [65] which allows radiometric and geometric corrections of each spectral band. As mentioned before, the radiometric calibration was done using an AirInov target [63] before executing the flights. The specific albedo values

were provided by the manufacturer [62], which allowed for the correction of the reflectivity values, ranging between 0 and 100.

To distinguish between forest, bare soil, and shrubs in the corrected images, first, a false color composite was generated. Therefore, the spectral bands NIR, RED, and GREEN were used [82], which highlight areas with vegetation in red, whereas other ground covers are shown in a different color. The false color composite was the basis for a non-supervised classification, using the Iso Cluster Unsupervised Classification tool available in ArcGis 10.5.1. [83,84]. This tool evaluates the whole dataset and classifies the vegetation into different categories (here: Herbs/bare soil, scrubland, and forest).

Then, the normalized difference vegetation index (NDVI) [85] was calculated, which expresses the vigorousness of the vegetation. The NDVI is directly related to the photosynthetic capacity and therefore to the energy absorption of the vegetation. Its magnitude ranges between -1 and 1 , in which negative values indicate water bodies, values near 0 bare soils, and positive values vegetation cover [86]. The NDVI is determined by the ratio of the NIR band (near infrared, 790 nm) and the RED band (red, 660 nm), expressed in Equation (3),

$$NDVI = \frac{NIR - RED}{NIR + RED} \quad (3)$$

where $NDVI$ is the normalized difference vegetation index, NIR = near-infrared band, and RED = red spectral band.

After the NDVI calculation, a regular grid mask of 1 hectare was overlaid, and all 25 cm pixels within a grid averaged to obtain a mean NDVI value per hectare. Finally, the equation for evergreen forest proposed by Das and Singh [50] was applied to calculate the AGB (Mg ha^{-1}), which can be written as follows,

$$AGB = 324.2 \times NDVI_{mean} + 14.18 \quad (4)$$

where AGB is the above-ground biomass (Mg ha^{-1}), and $NDVI_{mean}$ is the normalized difference vegetation index, averaged for 1 ha.

4.3.3 Validation of the RGB and Multispectral AGB Estimations

The two different techniques for AGB estimation (RGB and multispectral data) using a UAV were validated by means of an independent AGB dataset (Mg ha^{-1}) derived from LiDAR data. The LiDAR survey was executed in the same study area in 2012, using a Leica Geosystem ALS-50-II CM laser scanner installed onboard a Eurocopter AS350B2 Ecuriel Helicopter. The resulting point cloud density was at least 10 pulses per 1 m^2 [31], from which a DTM, DSM, and CHM model in a $25 \text{ cm} \times 25 \text{ cm}$ resolution was generated, and the AGB (Mg ha^{-1}) calculated applying an allometric equation [49]. For more details about the LiDAR-AGB calculation, please refer to González-Jaramillo et al. [8].

The RGB model executed in this study is similar to the LiDAR approach [8], although the RGB camera is a passive sensor, whereas the LiDAR laser scanner an active sensor. Therefore, the generated DTM, DSM, CHM and individual tree parameters obtained from the RGB data were compared to the reference data from LiDAR. The multispectral model is different because the AGB (Mg ha^{-1}) is directly calculated by means of the equation for tropical evergreen forests proposed by Das and Singh [50], which is why only the resultant AGB values were compared to the reference LiDAR-AGB.

The accuracy of the obtained results, RGB or multispectral vs. LiDAR, were determined by means of the coefficient of determination (R^2) and the root mean square error (RMSE) [46,87]. The equation for R^2 (Equation (5)) and RMSE (Equation (6)) are written as follows,

$$R^2 = \frac{\sum_{i=1}^n (x_i - \bar{x})^2 (y_i - \bar{y})^2}{\sum_{i=1}^n (x_i - \bar{x})^2 \sum_{i=1}^n (y_i - \bar{y})^2} \quad (5)$$

$$RMSE = \sqrt{\frac{\sum_{i=1}^n (x_i - y_i)^2}{n}} \quad (6)$$

where x_i and y_i are the estimated and measured values, \bar{x} and \bar{y} are the average estimated and measured values, and n is the total number of existing values with respect to the compared parameters.

4.4 Results

4.4.1 AGB Results by Means of RGB Data

By executing the explained photogrammetric processes for the RGB data, an orthophoto (Figure 4-3) and a point cloud image were obtained (Figure 4-5). The orthophoto was used simply for supervision, while from the point cloud, the horizontal and vertical structure of the TMF at tree level was determined. The point cloud image had an average density of 30 points/m² for the total zone (~80 ha), but zones with no information were also present, especially near the borders of the flight domain, for which reason a core area (24 ha) was established to avoid gaps in the information. Furthermore, due to the dense canopies and the fast-changing topography in the core area, which impede the determination of bare earth points by means of images of the RGB information, the high resolution DTM (25 cm × 25 cm) generated from the LiDAR survey (2012) was used to generate the CHM. As Karpina et al. [77] stated, this interchange is practicable because passive remote sensors cannot detect the terrain surface under dense canopy layers. Therefore, to generate the CHM, the ancillary LiDAR-DTM was subtracted from the RGB-DSM. Then, the Canopy Maxima tool of FUSION 3.7 was executed to detect the local maxima in the CHM, which represents the H of individual trees and their location. A total of 7075 dominant trees were detected (Figure 4-6a), and, by means of Equation (1), their individual DBH calculated. To estimate AGB (Mg ha⁻¹), a grid mask of 1 ha × 1 ha was overlaid and all AGB values of the individual trees within a grid cell were added up. The resulting AGB map of the core area is shown in Figure 4-6b.

H varied between 8.50 m to 35.32 m in the core area in which the individual tree distribution depended on the topographical position. Bigger trees were found in depressions (ravine forest) because these locations are topographically more protected compared to the ridges (ridge forest), and trees are generally taller there [22,88]. This is also caused by the prevailing soil types present at the different locations [53]. In general, the down-slope fluxes accumulate material and nutrients in the depression [22], which is why soil depth and nutrient concentrations are generally higher there, supporting the resulting tree growth [22,88]. The ridge forest parts are frequently affected by soil erosion processes due to the steeper slopes and harsher climate conditions [56], which lead to

shallow soils and unstable conditions (landslides) at these areas [55], subsequently reducing tree growth.

The DBH ranged between 10.01 cm and 127.39 cm, while distribution also depended on the topographical positions [54]. In general, the estimated AGB (Mg ha^{-1}) was related to the topographical position and the specific forest type (ravine or ridge) and ranged between 18.77 Mg ha^{-1} (open ridge forest) and $317.77 \text{ Mg ha}^{-1}$ (dense ravine forest), with a mean value of $148.83 \text{ Mg ha}^{-1}$ for the core study area. In Figure 4-6, the aforementioned distribution is clearly visible, where higher AGB values (green and yellow colors) are located inside the side valley and near the valley bottom, whereas lower AGB values (orange and red colors) are displayed at the ridges or steep slopes, where small vegetation (shrubs or small trees) or regeneration areas prevail.

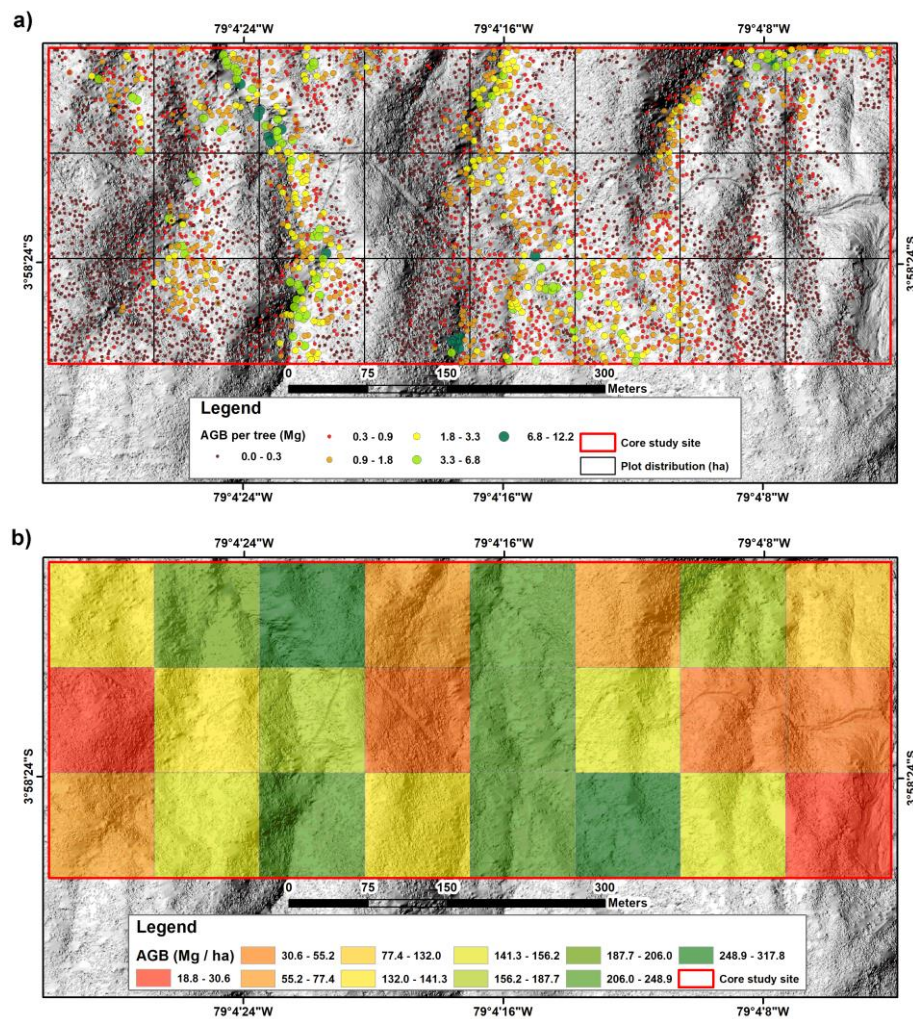


Figure 4-6: (a) Individual AGB values of the dominant trees detected in the core area; (b) Spatial distribution of AGB obtained from the RGB data.

4.4.2 AGB Results by Means of Multispectral Data

By utilizing the multispectral data, a false color composite was generated as well as the individual NDVI values for each pixel (25 cm) calculated. The false color composite provided the basis for an unsupervised classification to divide the vegetation cover in herbs/bare soil, scrubland, and forest (Figure 4-7a). The vegetation classification was used for visual inspection to verify the calculated NDVI values corresponding to these vegetation classes. The calculated NDVI map is illustrated in Figure 4-7b, displaying generally high values of between 0.38 and 0.86. Only water bodies (river course) showed negative values, while bare soil's NDVIs up to 0.20. The remaining land cover units had high positive values, which indicates vigorous vegetation [40,89]. Nonetheless, the forest distribution is detectable in the NDVI map, where higher values (dark green) were displayed inside the side valleys and slightly lower values (light green) at the ridges (Figure 4-7b). The individual NDVI values were averaged for each hectare and integrated in Equation (4) to obtain AGB (Mg ha^{-1}).

The resulting AGB map is illustrated in Figure 4-8, indicating values between 191.46 Mg ha^{-1} and 252.11 Mg ha^{-1} . The mean value corresponds to 237.21 Mg ha^{-1} . However, due to the generally high NDVI in the study area (natural TMF), the differences between ravine and ridge forest were indistinct, which resulted in high AGB values for the whole area.

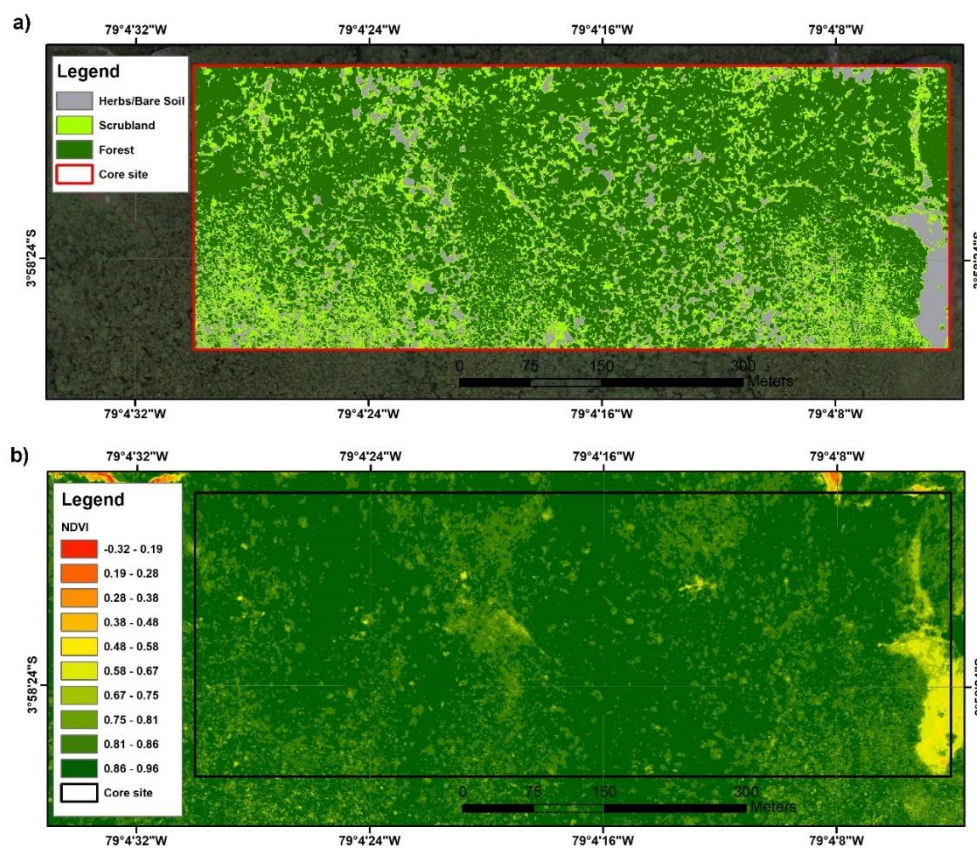


Figure 4-7: Multispectral data obtained by the multispectral camera, (a) non-supervised classification based on the false color composition image and (b) NDVI values.

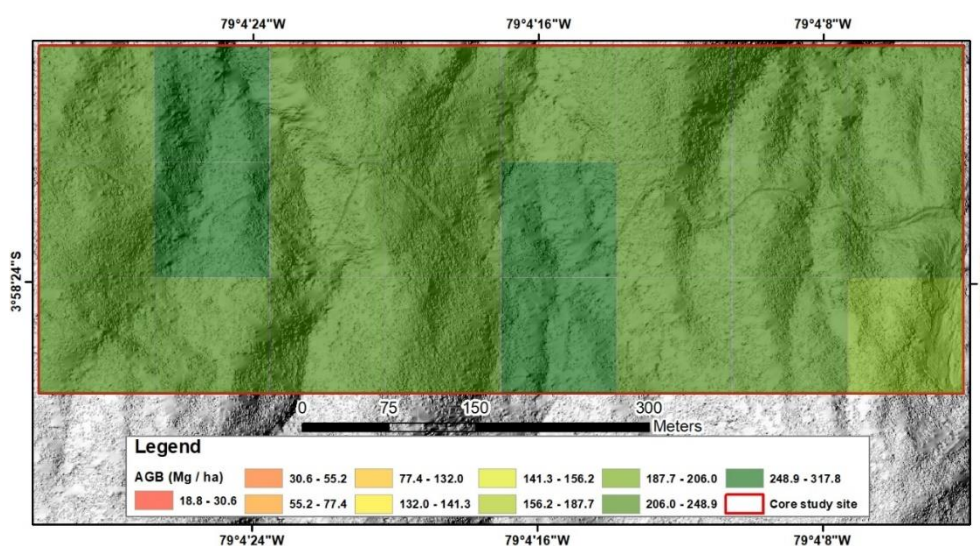


Figure 4-8: AGB estimation by means of multispectral data.

4.4.3 Validation

The validation was realized by means of the statistic software R-Studio (version 1.1.453) [90]. First, the results obtained from the RGB camera were analyzed, in which the individual generated models (DTM, DSM, and CHM) were compared to the LiDAR models [8]. The DTM comparison was made for two transects (Figure 4-3, yellow lines), one over dense vegetation cover and another over sparse or non-vegetation sites (Figure 4-9, red and black lines). It is clearly visible in Figure 4-9a that the RGB camera can hardly detect the terrain surface under dense vegetation (differences up to 20 m) because this passive sensor is not able to penetrate dense canopy layers [91,92]. In contrast, for sparse or non-vegetated areas (Figure 4-9b), only small differences between the RGB-DTM and the LiDAR-DTM were obtained (differences up to 2 m). Therefore, the RGB-DTM generation is largely inaccurate for natural tropical forests, especially for areas with dense vegetation, where high canopies obstruct the detection of the terrain surface (RGB-DTM RMSE: ~9 m, Table 4-1).

In contrast, the DSM comparison for both transects showed good accordance between the RGB and the LiDAR model because the top of the surface (here: Crown level) can be analyzed by means of RGB data (Figure 4-9, green and grey lines). This is confirmed by the statistics (Table 4-1), which determined a coefficient of determination (R^2) of 0.99 with an RMSE of 3.05 m at very high significance level <0.001 (p -value). However, differences between dense vegetation (Figure 4-9a, R^2 of 0.98 and a RMSE of 1.38 m) and less-vegetated sites (Figure 4-9b, R^2 of 0.99 with an RMSE of 0.49 m) were notable, which is due to the irregular canopy layer in dense natural TMF [22] and the time span between the LiDAR and UAV survey (vegetation growth).

By means of the DTM and the DSM, a CHM could be generated, but due to the high errors in the RGB-DTM, the RGB-CHM error also showed high inaccuracy (RMSE = 8.65 m), and no correlation between RGB-CHM and LiDAR-CHM could be determined ($R^2 = 0.18$, Table 4-1). Therefore, as Karpina et al. [77] suggested, the RGB-DTM was replaced by an accurate DTM in very high resolution (LiDAR-DTM) to guarantee a reliable CHM generation and a subsequent individual tree classification. Using the LiDAR-DTM in combination with the RGB-DSM (RGB-CHM*, Table 4-1), errors were notably reduced (RMSE = 3.00 m) and a good correlation between the models was

obtained ($R^2 = 0.80$). Therefore, the RGB-CHM* model was used for the individual tree classification to determine H and DBH for the final AGB estimation.

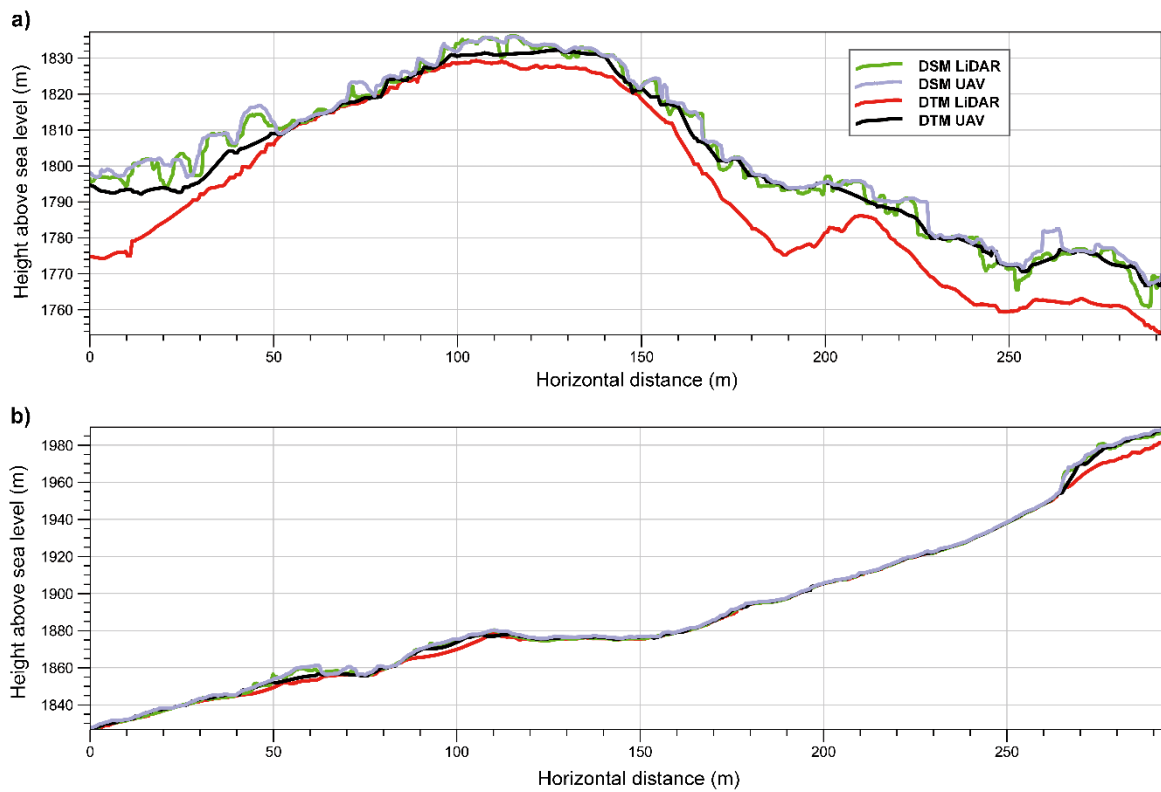


Figure 4-9: Transect profiles, comparing RGB and light detection and ranging (LiDAR) models: (a) Vegetated areas, (b) less vegetated areas.

Within the core study area, a total of 7075 dominant trees were detected on basis of the RGB-CHM*, applying the canopy maxima method [80]. In comparison to the LiDAR-CHM in which 7317 trees were detected for the same area, results were similar (96.69%, Table 4-2). From the individual tree detection, H was deviated and DBH of each tree calculated. As shown in Table 4-2, H and DBH values for the individual trees were in the same range comparing RGB and LiDAR data, which resulted in similar AGB values. However, maximum AGB values were slightly higher for the RGB data, which may be due to the RMSE of the RGB-DSM (Table 4-1) or the time span between the surveys (vegetation growth).

Table 4-1: AGB validation comparing RGB models with the LiDAR models.

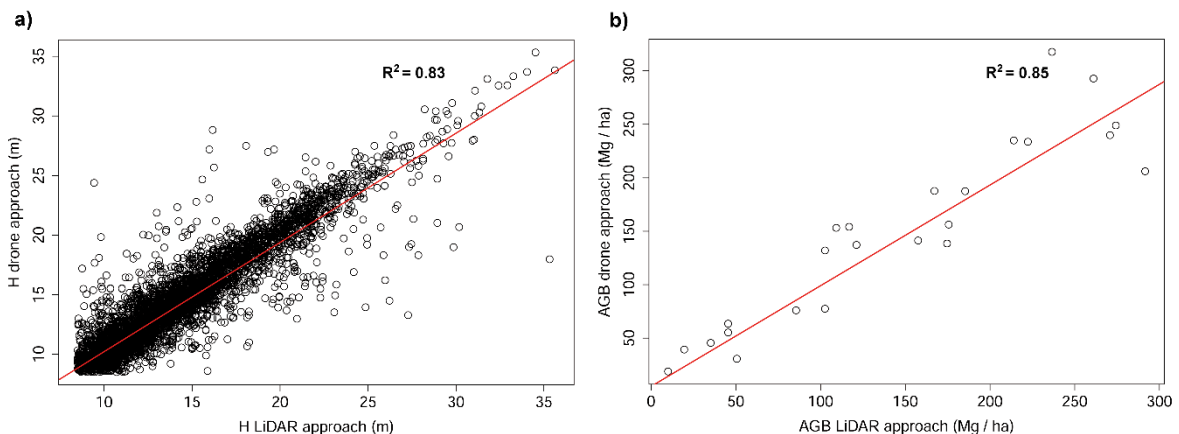
Approach	R ²	RMSE (m)	p-value
RGB-DTM vs. LiDAR-DTM	0.99	8.95	<0.001
RGB-DSM vs. LiDAR-DSM	0.99	3.05	<0.001
RGB-CHM vs. LiDAR-CHM	0.18	8.65	<0.001
RGB-CHM* vs. LiDAR-CHM	0.80	3.00	<0.001

* combination of LiDAR-DTM and RGB-DSM.

Table 4-2: Calculated H, DBH, and AGB values (RGB above and LiDAR below).

Sensor	Tree Individuals	Height (m)			DBH (cm)			AGB (Mg / ha)			
		Min	Mean	Max	Min	Mean	Max	Min	Mean	Max	SD
RGB	7075	8.50	14.66	35.32	10.01	28.08	127.39	18.77	148.66	317.77	83.96
LiDAR	7317	8.50	14.52	36.31	10.01	27.57	133.83	10.01	144.83	291.58	85.45

Furthermore, the RGB results (H, DBH, and AGB) were plotted against the LiDAR results (Figure 4-10). Therefore, the deviated H (Figure 4-10a) and calculated DBH values of all detected trees from the RGB (7075 individuals) were used and a linear regression analysis executed. The results showed a good correlation for H ($R^2 = 0.83$) and DBH ($R^2 = 0.83$). AGB amounts of the specific hectares (24 ha) were also compared, which resulted in a good correlation between RGB-AGB and LiDAR-AGB ($R^2 = 0.85$, at a significance level $p\text{-value} < 0.001$, Figure 4-10b).

**Figure 4-10:** Regression analysis between RGB and LiDAR data: (a) H correlation, (b) AGB correlation.

Then, the AGB results obtained from the multispectral data were validated against the LiDAR estimates. In Table 4-3, the calculated minimum, mean, and maximum AGB values are presented, which indicate notable differences. The calculated minimum AGB of the multispectral data ($191.46 \text{ Mg ha}^{-1}$) was notably higher, whereas as maximum AGB ($252.11 \text{ Mg ha}^{-1}$) was lower than the LiDAR estimates. The absence of correlation between the multispectral and LiDAR results ($p\text{-value} > 0.05$) was confirmed by the very low R^2 ($p\text{-value} < 0.01$) and the very high RMSE (127.35 m). The large differences were due to the tendency towards saturation of multispectral sensors for healthy and vigorous vegetation [82], for which reason, generally, high NDVI values were obtained for the whole area (Figure 4-7b), which resulted in similar AGB values for all hectares under study and consequently in unclear forest structure detection.

Table 4-3: Calculated AGB from multispectral and LiDAR data.

Sensor	Cover (ha)	AGB (Mg / ha)			
		Min	Mean	Max	SD
Multispectral	24	191.46	237.21	252.11	13.02
LiDAR	24	10.01	144.83	291.58	85.45

4.5 Discussion

Regarding the UAV technology used for AGB estimation in this natural TMF in Southern Ecuador, two main issues could be identified. First, flight time and image resolution are related to topographic conditions as well as to the payload capacity of the employed UAV, which determine the area covered by one single flight as well as the final GSD resolution (pixel size). Furthermore, a high overlap of the individual images is necessary and an adequate number of GCPs must be established [67,68] to obtain the required image accuracy during the photogrammetric process. The second issue refers particularly to the RGB images and the 3D point cloud generation. As the study showed, terrain or ground data (DTM) under dense forest canopies cannot be detected accurately because passive sensors do not have the capacity to penetrate dense forest canopies [91,92]. However, the methodology can be applied in managed forest, where gaps are big enough and generally homogeneous, which permits the detection of the terrain [93]. In dense natural forest, an

adequate auxiliary DTM in high resolution (here: LiDAR-DTM) is necessary to generate a realistic CHM for further analysis [77,94].

Considering the second issue, it could be stated that from the RGB-CHM* the structural parameters of the forest could be identified, which include the forest type (here: Ravine or ridge) as well as H of each individual tree detected. Biggest trees were found in the protected ravine TMF parts (valleys and side valleys) with H up to 35.32 m, similar to González-Jaramillo et al. [8], who used LiDAR data for individual tree classification (36.31 m, Table 4-1). The same maximum H was reported by Paulick et al. [54] and Leuschner et al. [95] within the same study area. Besides this, mean H (14.66 m) was equal to the values presented by of Homeier et al. [96], who installed field plots at lower elevation, which confirms the accuracy of the applied method.

By means of the individual H and the specific equation proposed by González-Jaramillo et al. [8] for the San Francisco catchment, DBH was calculated at tree level. Due to similar H values (Figure 4-10a), a good correlation for DBH between RGB and LiDAR data could be recorded (R^2 : 0.83, p -value < 0.001, Figure 4-10b). Mean DBH was only slightly higher (28.08 cm) than the validated values from the LiDAR data (27.57 cm, Table 4-1). However, other studies presented notably lower mean DBH for this TMF (Mean DBH: 9.8 cm) [97], but these investigations included mid- and understory trees as well as trees at higher elevations, where harsher climate conditions and the more exposed position reduce H and DBH of the trees [55,56].

The individual tree classification applied here only detects dominant trees because smaller mid- and understory trees are often not visible due to the upper canopy layer [78]. Therefore, RGB information, but also LiDAR approaches, slightly overestimate the real mean DBH in dense natural tropical forests [8]. Nonetheless, dominant trees are most important for AGB estimation because they represent 70% to 90% of the total AGB of a forest stand [18,19]. To calculate the AGB (Mg ha^{-1}) by means of the individual tree classification, the specific allometric equation for wet forests from Chave et al. [49] was applied. The results clearly reflected the forest structure of this TMF because highest AGB was estimated inside the side valleys (ravine forest, up to $317.77 \text{ Mg ha}^{-1}$), whereas lowest AGB was near the ridges (ridge forest, 18.77 Mg ha^{-1} , Figure 4-6). Mean AGB for the core area ($148.66 \text{ Mg ha}^{-1}$, Table 4-1) was in the same range as the LiDAR approach

[8], but also similar to other AGB estimations published in previous studies (150.0 Mg ha⁻¹) based on field plot measurements at lower elevation [22,54,95,98]. The small AGB differences between RGB-AGB and LiDAR-AGB were due to the RMSE of the RGB-CHM* and the number of trees detected, considering also the time span between RGB and LiDAR survey (see Section 4.4.3). Also of note, the TMF in the study area is protected and consists of mature forest (60 to 80 years old trees), where trees generally grow slowly, especially the older individuals [88]. Therefore, bigger AGB increments over time could not be expected, but other land cover changes, like landslides, which occur naturally, provoke a reduction in AGB for the affected areas until natural regeneration reestablishes the vegetation cover.

The multispectral image approach to calculate AGB by means of the deviated NDVI and applying the equation from Das and Singh [50] resulted in marked overestimations, especially for less vegetated sites (Table 4-3). This was principally due to the tendency towards saturation of the spectral bands over dense forest covers [82], resulting in similar and high AGB values for all hectares, which is why forest structure could not be depicted. This type of sensor saturation was also reported by Gu et al. [99], who obtained very high NDVI values in areas with dense canopies in the USA. Therefore, the NDVI can hardly be used in natural TMF for AGB estimation because differences in the fast-changing topography and vegetation cover cannot be detected. The applied equation from Das and Singh [50], who established their NDVI–AGB relationship in an evergreen forest in the Western Ghat region of India, also might not be suitable for AGB estimation in this TMF in Southern Ecuador. Therefore, the equation should be adjusted to provide explicit and more accurate NDVI–AGB relationships for individual ecosystems, but the matter with spectral band saturation for dense forest stand will persist. Nonetheless, the multispectral approach might be useful for crops in combination with crop height information to calculate the AGB [46,100] due to the generally more uniform ground cover and topography.

In summary, the more effective and accurate approach to estimate AGB by means of UAVs in natural TMF is the RGB alternative, applying an analysis at tree level. During the process, forest structure as well as individual H and DBH of each tree detected can be determined [101]. These parameters, in combination with mean WD of the specific forest type, allowed a realistic AGB calculation. The RGB data permit the precise detection of

the surface (DSM), but ancillary terrain data in high resolution (DTM) from other sources is necessary in natural tropical forest because the dense canopies impede ground detection (canopy closure often 100%) [39,58]. However, in natural mid and high latitude forests [102] as well as in managed forests [93], the RGB approach might be a cost-effective alternative to expensive LiDAR surveys [103] due to the different forest stand characteristics with open canopies or regular distance between individual trees, which allows for accurate ground detection [77].

4.6 Conclusions

UAVs have the potential to generate terrain and surface information in high temporal and spatial resolution, due to their portability and flexibility. Furthermore, UAVs can be equipped with different sensors, which allow a wide range of applications and contribute to the advances in the remote sensing field. In contrast to classical remote sensing data (satellite images), UAVs also avoid the problems of cloudiness, which is particularly advantageous in tropical high mountains. Nonetheless, their range is limited due to the battery capacity and the additional payload, which reduce their flight time. Therefore, UAVs can adequately monitor smaller areas, besides the ability to fill gaps in existing imagery (e.g., LiDAR data).

As the study showed, for a reliable AGB estimation (Mg ha^{-1}) in natural TMF, a tree level classification is necessary. This can be reached by RGB images with high side and forward overlap (80% or higher), to obtain multiple viewing angles of the objects to generate 3D point clouds. However, in natural tropical forests, terrain information is difficult to capture with this passive sensor due to the dense canopy layer, which impedes ground detection. Therefore, auxiliary DTMs in high resolution must be considered to generate reliable CHMs for the subsequent classification at tree level and AGB calculation.

In contrast, multispectral images suffer saturation of the spectral bands over dense natural forest stands, which results in generally high NDVI values with small differences between the land cover units. Therefore, AGB estimation, based on NDVI values, overestimates the real amounts in natural TMF, especially at less vegetated sites.

Author Contributions: Víctor González-Jaramillo processed the UAV data, wrote and edited the manuscript. Andreas Fries gave advice on the research design, analyzed the tree data and wrote the draft of the manuscript. Jörg Bendix gave advice on the research design and the methodology and also revised the manuscript.

Funding: This research was funded by DFG Research Unit 816: Biodiversity and Sustainable Management of Mega-diverse Mountain Ecosystems in South Ecuador (ALS under BE1780/17-2) and the APC was funded by Bilateral Cooperation with South Ecuadorian Universities in Ecosystem Research (BE1780-20-2; 27-2; 32-1).

Acknowledgments: This study was executed in framework with the DFG Research Unit 816: Biodiversity and Sustainable Management of Mega-diverse Mountain Ecosystems in South Ecuador (ALS under BE1780/17-2). The authors thank the German Research Foundation DFG for funding the PhD of V. González-Jaramillo in the scope of the program “Bilateral Cooperation with South Ecuadorian Universities in Ecosystem Research” (BE1780-20-2; 27-2; 32-1). Thanks, are also due to the collaboration of the Universidad Técnica Particular de Loja (UTPL) to facilitate this research by means of project PY1760, funded by the Smart Land initiative. Special thanks to Gregory Gedeon for text revision.

Conflicts of Interest: The authors declare no conflict of interest.

4.7 References

1. Iizuka, K.; Yonehara, T.; Itoh, M.; Kosugi, Y. Estimating Tree Height and Diameter at Breast Height (DBH) from Digital Surface Models and Orthophotos Obtained with an Unmanned Aerial System for a Japanese Cypress (*Chamaecyparis obtusa*). *For. Remote Sens.* **2018**, *10*, 13.
2. Shin, P.; Sankey, T.; Moore, M.M.; Thode, A.E. Evaluating Unmanned Aerial Vehicle Images for Estimating Forest Canopy Fuels in a Ponderosa Pine Stand. *Remote Sens.* **2018**, *10*, 1266.
3. IPCC. *Working Group I Contribution to the IPCC Fifth Assessment Report Climate Change 2013: The Physical Science Basics*; IPCC: Stockholm, Sweden, 2013.
4. Pütz, S.; Groeneveld, J.; Henle, K.; Camargo Martensen, A.; Metz, M.; Metzger, J.P.; Ribeiro, M.C.; Dantas de Paula, M.; Huth, A. Long-term carbon loss in fragmented Neotropical forests. *Nat. Commun.* **2014**, *5*, 5037.
5. Ota, T.; Kajisa, T.; Mizoue, N.; Yoshida, S.; Takao, G.; Hirata, Y.; Furuya, N.; Sano, T.; Ponce-Hernandez, R.; Ahmed, O.S.; et al. Estimating aboveground carbon using airborne LiDAR in Cambodian tropical seasonal forests for REDD+ implementation. *J. For. Res.* **2015**, *20*, 484–492, doi:10.1007/s10310-015-0504-3.
6. Mitchell, A.L.; Rosenqvist, A.; Mora, B. Current remote sensing approaches to monitoring forest degradation in support of countries measurement, reporting and verification (MRV) systems for REDD+. *Carbon Balance Manag.* **2017**, *12*, 9.
7. FAO. *Evaluación de Recursos Forestales Mundiales 2010—Informe Principal*; FAO: Roma, Italy, 2010.
8. González-Jaramillo, V.; Fries, A.; Zeilinger, J.; Homeier, J.; Paladines-Benitez, J.; Bendix, J. Estimation of Above Ground Biomass in a Tropical Mountain Forest in Southern Ecuador Using Airborne LiDAR Data. *Remote Sens.* **2018**, *10*, 660.
9. Tapia-Armijos, M.F.; Homeier, J.; Espinosa, C.I.; Leuschner, C.; de la Cruz, M. Deforestation and Forest Fragmentation in South Ecuador since the 1970s—Losing a Hotspot of Biodiversity. *PLoS ONE* **2015**, *10*, e0133701. doi:10.1371/journal.pone.0133701.
10. FAO. *Evaluación de los Recursos Forestales Mundiales 2010—Informe Nacional Ecuador*; FAO: Roma, Italy, 2010.
11. Ochoa-Cueva, P.; Fries, A.; Montesinos, P.; Rodríguez-Díaz, J.A.; Boll, J. Spatial Estimation of Soil Erosion Risk by Land-cover Change in the Andes of Southern Ecuador. *Land Degrad. Dev.* **2015**, *26*, 565–573, doi:10.1002/ldr.2219.
12. Curatola Fernández, G.; Obermeier, W.; Gerique, A.; López Sandoval, M.; Lehnert, L.; Thies, B.; Bendix, J. Land cover change in the Andes of Southern Ecuador—Patterns and drivers. *Remote Sens.* **2015**, *7*, 2509–2542.

13. Mosandl, R.; Günter, S.; Stimm, B.; Weber, M. Ecuador suffers the highest deforestation rate in South America. In *Gradients in a Tropical Mountain Ecosystem of Ecuador*, 1st ed.; Beck, E., Bendix, J., Kottke, I., Makeschin, F., Mosandl, R., Eds.; Ecological Studies; Springer: Berlin/Heidelberg, Germany, 2008; Volume 198, pp. 37–40.
14. Richter, M.; Beck, E.; Rollenbeck, R.; Bendix, J. The Study Area. In *Ecosystem Services, Biodiversity and Environmental Change in a Tropical Mountain Ecosystem of South Ecuador*, 1st ed.; Bendix, J., Beck, E., Bräuning, A., Makeschin, F., Mosandl, R., Scheu, S., Wilcke, W., Eds.; Springer: Berlin/Heidelberg, Germany, 2013; Volume 221, pp. 1–19, ISBN 978-3-642-38136-2.
15. Beck, E.; Harting, K.; Roos, K. Forest clearing by slash and burn. In *Gradients in a Tropical Mountain Ecosystem of Ecuador*, 1st ed.; Beck, E., Bendix, J., Kottke, I., Makeschin, F., Mosandl, R., Eds.; Ecological Studies; Springer: Berlin/Heidelberg, Germany, 2008; Volume 198, pp. 371–374.
16. Miettinen, J.; Stibig, H.-J.; Achard, F. Remote sensing of forest degradation in Southeast Asia—Aiming for a regional view through 5–30 m satellite data. *Glob. Ecol. Conserv.* **2014**, *2*, 24–36, doi:10.1016/j.gecco.2014.07.007.
17. Ortiz-Colín, P.; Toledo-Aceves, T.; López-Barrera, F.; Gerez-Fernández, P. Can traditional selective logging secure tree regeneration in cloud forest. *iForest* **2017**, *10*, 369–375.
18. Kotowska, M.M.; Leuschner, C.; Triadiati, T.; Meriem, S.; Hertel, D. Quantifying above- and belowground biomass carbon loss with forest conversion in tropical lowlands of Sumatra (Indonesia). *Glob. Chang. Biol.* **2015**, *21*, 3620–3634, doi:10.1111/gcb.12979.
19. Bastin, J.F.; Barbier, N.; Réjou-Méchain, M.; Fayolle, A.; Gourlet-Fleury, S.; Maniatis, D.; de Haulleville, T.; Baya, F.; Beeckman, H.; Beina, D. et al. Seeing Central African forests through their largest trees. *Sci. Rep.* **2015**, *5*, 13156, doi:10.1038/srep13156.
20. Meyer, V.; Saatchi, S.; Clark, D.B.; Keller, M.; Vincent, G.; Ferraz, A.; Espírito-Santo, F.; d'Oliveira, M.V.N.; Kaki, D.; Chave, J. Canopy area of large trees explains aboveground biomass variations across neotropical forest landscapes. *Biogeosciences* **2018**, *15*, 3377–3390, doi:10.5194/bg-15-3377-2018.
21. Cuni-Sanchez, A.; Pfeifer, M.; Marchant, R.; Calders, K.; Sørensen, C.L.; Pompeu, P.V.; Lewis, S.L.; Burgess, N.D. New insights on above ground biomass and forest attributes in tropical montane forests. *For. Ecol. Manag.* **2017**, *399*, 235–246, doi:10.1016/j.foreco.2017.05.030.
22. Werner, F.A.; Homeier, J. Is tropical montane forest heterogeneity promoted by a resource-driven feedback cycle? Evidence from nutrient relations, herbivory and litter decomposition along a topographical gradient. *Funct. Ecol.* **2015**, *29*, 430–440, doi:10.1111/1365-2435.12351.

23. Ferraz, A.; Saatchi, S.; Mallet, C.; Jacquemoud, S.; Goncalves, G.; Silva, A.A.; Soares, P.; Tomé, M.; Pereira, L. Airbone Lidar Estimation of Aboveground Forest Biomass in the Absence of Field Inventory. *Remote Sens.* **2016**, *8*, 653.
24. Sinha, S.; Jeganathan, C.; Sharma, L.K.; Nathawat, M.S. A review of radar remote sensing for biomass estimation. *Int. J. Environ. Sci. Technol.* **2015**, *12*, 1779–1792.
25. Qin, Y.; Xiao, X.; Wang, J.; Dong, J.; Ewing, K.; Hoagland, B.; Hough, D.J.; Fagin, T.D.; Zou, Z.; Geissler, G.L.; et al. Mapping annual forest cover in sub-humid and semi-arid regions through analysis of Landsat and PALSAR imagery. *Remote Sens.* **2016**, *8*, 933.
26. Galidaki, G.; Zianis, D.; Gitas, I.; Radoglou, K.; Karathanassi, V.; Tsakiri–Strati, M.; Woodhouse, I.; Mallinis, G. Vegetation biomass estimation with remote sensing: Focus on forest and other wooded land over the Mediterranean ecosystem. *Int. J. Remote Sens.* **2017**, *38*, 1940–1966, doi:10.1080/01431161.2016.1266113.
27. MacLachlan, A.; Roberts, G.; Biggs, E.; Boruff, B. Subpixel land-cover classification for improved urban area estimates using Landsat. *Int. J. Remote Sens.* **2017**, *38*, 5763–5792, doi:10.1080/01431161.2017.1346403.
28. Aasen, H.; Honkavaara, E.; Lucieer, A.; Zarco-Tejada, P.J. Quantitative Remote Sensing at Ultra-High Resolution with UAV Spectroscopy: A Review of Sensor Technology, Measurement Procedures, and Data Correction Workflows. *Remote Sens.* **2018**, *10*, 1091.
29. Dash, J.P.; Pearse, G.D.; Watt, M.S. UAV Multispectral Imagery Can Complement Satellite Data for Monitoring Forest Health. *Remote Sens.* **2018**, *10*, 1216.
30. Rodríguez-Veiga, P.; Wheeler, J.; Louis, V.; Tansey, K.; Balzter, H. Quantifying forest biomass carbon stocks from space. *Curr. For. Rep.* **2017**, *3*, 1–18. doi:10.1007/s40725-017-0052-5.
31. Silva, B.; Bendix, J. Remote sensing of vegetation in a tropical mountain ecosystem: Individual tree-crown detection. *Proc. SPIE* **2013**, *8893*, 99830B.
32. Asner, G.P.; Mascaro, J. Mapping tropical forest carbon: Calibrating plot estimates to a simple LiDAR metric. *Remote Sens. Environ.* **2014**, *140*, 614–624.
33. Li, A.; Dhakal, S.; Glenn, N.F.; Spaete, L.P.; Shinneman, D.J.; Pilliod, D.S.; Arkle, R.S.; McIlroy, S.K. Lidar Aboveground Vegetation Biomass Estimates in Shrublands: Prediction, Uncertainties and Application to Coarser Scales. *Remote Sens.* **2017**, *9*, 903.
34. Wallis, C.I.; Homeier, J.; Peña, J.; Brandl, R.; Farwig, N.; Bendix, J. Modeling tropical montane forest biomass, productivity and canopy traits with multispectral remote sensing data. *Remote Sens. Environ.* **2019**, *225*, 77–92.
35. Bendix, J.; Rollenbeck, R.; Palacios, E. Cloud detection in the Tropics—A suitable tool for climate-ecological studies in the high mountains of Ecuador. *Int. J. Remote Sens.* **2004**, *25*, 4521–4540. doi:10.1080/01431160410001709967.

36. Purnamasayangasukasih, R.P.; Norizah, K.; Ismail, A.A.M.; Shamsudin, I. A review of uses of satellite imagery in monitoring mangrove forests. *IOP Conf. Ser. Earth Environ. Sci.* **2016**, *37*, 012034.
37. Zhang, X.; Friedl, M.A.; Schaaf, C.B.; Strahler, A.H.; Hodges, J.C.F.; Gao, F.; Reed, B.C.; Huete, A. Monitoring vegetation phenology using MODIS. *Remote Sens. Environ.* **2003**, *84*, 471–475. doi:10.1016/S0034-4257(02)00135-9.
38. Paruelo, J.M.; Garbulsky, M.F.; Guerschman, J.P.; Jobbágy, E.G. Two decades of Normalized Difference Vegetation Index changes in South America: Identifying the imprint of global change. *Int. J. Remote Sens.* **2004**, *25*, 2793–2806, doi:10.1080/01431160310001619526.
39. Göttlicher, D.; Obregon, A.; Homeier, J.; Rollenbeck, R.; Nauss, T.; Bendix, J. Land-cover classification in the Andes of southern Ecuador using Landsat ETM+ data as a basis for SVAT modelling. *Int. J. Remote Sens.* **2009**, *30*, 1867–1886.
40. González-Jaramillo, V.; Fries, A.; Rollenbeck, R.; Paladines, J.; Oñate-Valdivieso, F.; Bendix, J. Assessment of deforestation during the last decades in Ecuador using NOAA-AVHRR satellite data. *Erdkunde* **2016**, *70*, 217–235.
41. Kim, E.; Lee, W.K.; Yoon, M.; Lee, J.Y.; Son, Y.; Abu Salim, K. Estimation of Voxel-Based Above-Ground Biomass Using Airborne LiDAR Data in an Intact Tropical Rain Forest, Brunei. *Forests* **2016**, *7*, 259.
42. Candiago, S.; Remondino, F.; De Giglio, M.; Dubbini, M.; Gattelli, M. Evaluating Multispectral Images and Vegetation Indices for Precision Farming Applications from UAV Images. *Remote Sens.* **2015**, *7*, 4026–4047.
43. Connor, D.; Martin, P.G.; Scott, T.B. Airborne radiation mapping: Overview and application of current and future aerial systems. *Int. J. Remote Sens.* **2016**, *37*, 5953–5987, doi:10.1080/01431161.2016.1252474.
44. Saarinen, N.; Vastaranta, M.; Näsi, R.; Rosnell, T.; Hakala, T.; Honkavaara, E.; Wulder, M.A.; Luoma, V.; Tommaselli, A.M.G.; Imai, N.N.; et al. Assessing Biodiversity in Boreal Forests with UAV-Based Photogrammetric Point Clouds and Hyperspectral Imaging. *Remote Sens.* **2018**, *10*, 338.
45. Kachamba, D.J.; Ørka, H.O.; Gobakken, T.; Eid, T.; Mwase, W. Biomass Estimation Using 3D Data from Unmanned Aerial Vehicle Imagery in a Tropical Woodland. *Remote Sens.* **2016**, *8*, 968.
46. Yue, J.; Yang, G.; Li, C.; Li, Z.; Wang, Y.; Feng, H.; Xu, B. Estimation of Winter Wheat Above-Ground Biomass Using Unmanned Aerial Vehicle-Based Snapshot Hyperspectral Sensor and Crop Height Improved Models. *Remote Sens.* **2017**, *9*, 708.
47. Weber, A.; Lerch, T. Point Clouds: Lase Scanning versus UAS Photogrammetry. *GIM Int.* **2018**, *4*, 36–39.
48. DJI. Inspire 1 Specs. Available online: <https://www.dji.com/inspire-1/info#downloads> (accessed on 10 October 2018).

49. Chave, J.; Andalo, C.; Brown, S.; Cairns, M.A.; Chambers, J.Q.; Eamus, D.; Fölster, H.; Fromard, F.; Higuchi, N.; Kira, T.; et al. Tree allometry and improved estimation of carbon stocks and balance in tropical forests. *Oecologia* **2005**, *145*, 87–99.
50. Das, S.; Singh, T.P. Forest Type, Diversity and Biomass Estimation in Tropical Forests of Western Ghat of Maharashtra Using Geospatial Techniques. *Small-Scale For.* **2016**, *15*, 517. doi:10.1007/s11842-016-9337-y.
51. Homeier, J.; Werner, F.A.; Gradstein, S.R.; Breckle, S.-W.; Richter, M. Potential vegetation and floristic composition of Andean forests in South Ecuador, with a focus on the RBSF. In *Gradients in a Tropical Mountain Ecosystem of Ecuador*, 1st ed.; Beck, E., Bendix, J., Kottke, I., Makeschin, F., Mosandl, R., Eds.; *Ecological Studies*; Springer: Berlin/Heidelberg, Germany, 2008; Volume 198, pp. 87–100.
52. Bendix, J.; Beck, E. Spatial aspects of ecosystem research in a biodiversity hot spot of southern Ecuador—An introduction. *Erdkunde* **2009**, *63*, 305–308, doi:10.3112/erdkunde.2009.04.01.
53. Moser, G.; Leuschner, C.; Hertel, D.; Graefe, S.; Soethe, N.; Iost, S. Elevation effects on the carbon budget of tropical mountain forests (S Ecuador): The role of the belowground compartment. *Glob. Chang. Biol.* **2011**, *17*, 2211–2226, doi:10.1111/j.1365-2486.2010.02367.x.
54. Paulick, S.; Dislich, C.; Homeier, J.; Fischer, R.; Huth, A. The carbon fluxes in different successional stages: Modelling the dynamics of tropical montane forests in South Ecuador. *For. Ecosyst.* **2017**, *4*, 5, doi:10.1186/s40663-017-0092-0.
55. Dislich, C.; Huth, A. Modelling the impact of shallow landslides on forest structure in tropical montane forests. *Ecol. Model.* **2012**, *239*, 40–53.
56. Wagemann, J.; Thies, B.; Rollenbeck, R.; Peters, T.; Bendix, J. Regionalization of wind-speed data to analyze tree-line wind conditions in the eastern Andes of southern Ecuador. *Erdkunde* **2015**, *69*, 13–19.
57. Fries, A.; Rollenbeck, R.; Göttlicher, D.; Nauß, T.; Homeier, J.; Peters, T.; Bendix, J. Thermal structure of a megadiverse Andean mountain ecosystem in southern Ecuador and its regionalization. *Erdkunde* **2009**, *63*, 321–335. doi:10.3112/erdkunde.2009.04.03.
58. Fries, A.; Rollenbeck, R.; Nauß, T.; Peters, T.; Bendix, J. Near surface air humidity in a megadiverse Andean mountain ecosystem of southern Ecuador and its regionalization. *Agric. For. Meteorol.* **2012**, *152*, 17–30, doi:10.1016/j.agrformet.2011.08.004.
59. Bendix, J.; Rollenbeck, R.; Richter, M.; Fabian, P.; Emck, P. Climate. In *Gradients in a Tropical Mountain Ecosystem of Ecuador*, 1st ed.; Beck, E., Bendix, J., Kottke, I., Makeschin, F., Mosandl, R., Eds.; *Ecological Studies*; Springer: Berlin/Heidelberg, Germany, 2008; Volume 198, pp. 63–74.
60. Fries, A.; Rollenbeck, R.; Bayer, F.; Gonzalez, V.; Oñate-Valivieso, F.; Peters, T.; Bendix, J. Catchment precipitation processes in the San Francisco valley in southern

- Ecuador: Combined approach using high-resolution radar images and in situ observations. *Meteorol. Atmos. Phys.* **2014**, *126*, 13–29, doi:10.1007/s00703-014-0335-3.
61. Windhorst, D.; Waltz, T.; Timbe, E.; Frede, H.G.; Breuer, L. Impact of elevation and weather patterns on the isotopic composition of precipitation in a tropical montane rainforest. *Hydrol. Earth Syst. Sci.* **2013**, *17*, 409–419.
 62. Parrot Sequoia. Available online: <https://www.parrot.com/business-solutions-us/parrot-professional/parrot-sequoia#parrot-sequoia-> (accessed on 5 October 2017).
 63. AirInov - Parrot Sequoia Calibration target. Available online: <https://www.parrot.com/business-solutions-us/spareparts/business-solutions/parrot-sequoia-calibration-target> (accessed on 5 October 2017).
 64. PRECISIONFLIGHT FREE. Available online: <https://www.precisionhawk.com/precisionflight> (accessed on 5 October 2017).
 65. Pix4D—Measure from Images. Available online: <https://www.pix4d.com/> (accessed on 5 October 2017).
 66. Sayab, M.; Aerden, D.; Paananen, M.; Saarela, P. Virtual Structural Analysis of Jokisivu Open Pit Using ‘Structure-from-Motion’ Unmanned Aerial Vehicles (UAV) Photogrammetry: Implications for Structurally-Controlled Gold Deposits in Southwest Finland. *Remote Sens.* **2018**, *10*, 1296.
 67. Claros, R.; Guevara, A.; Pacas, N. Aplicación de Fotogrametría Aérea en Levantamientos Topográficos mediante el uso de Vehículos Aéreos no Tripulados. Civil Engineer. Universidad de El Salvador, El Salvador. 2016. Available online: <http://ri.ues.edu.sv/14218/1/50108282.pdf> (accessed on 10 April 2019).
 68. Boccardo, P.; Chiabrand, F.; Dutto, F.; Tonolo, F.G.; Lingua, A. UAV Deployment Exercise for Mapping Purposes: Evaluation of Emergency Response Applications. *Sensors* **2015**, *15*, 15717–15737. doi:10.3390/s150715717.
 69. Chave, J.; Réjou-Méchain, M.; Búrquez, A.; Chidumayo, E.; Colgan, M.S.; Delitti, W.B.; Duque, A.; Eid, T.; Fearnside, P.M.; Goodman, R.C. et al. Improved allometric models to estimate the aboveground biomass of tropical trees. *Glob Chang. Biol.* **2014**, *20*, 3177–3190. doi:10.1111/gcb.12629.
 70. Piironen, R.; Heiskanen, J.; Maeda, E.; Viinikka, A.; Pellikka, P. Classification of tree species in a diverse African Agroforestry landscape using imaging spectroscopy and laser scanning. *Remote Sens.* **2017**, *9*, 875, doi:10.3390/rs9090875.
 71. Coomes, D.A.; Dalponte, M.; Jucker, T.; Asner, G.P.; Banin, L.F.; Burslem, D.F.R.P.; Lewis, S.L.; Nilus, R.; Phillips, O.L.; Phua, M.; et al. Area-based vs tree-centric approaches to mapping forest carbon in Southeast Asian forests from airborne laser scanning data. *Remote Sens. Environ.* **2017**, *194*, 77–88, doi:10.1016/j.rse.2017.03.017.

72. Gao, X.; Li, Z.; Yu, H.; Jiang, Z.; Wang, C.; Zhang, Y.; Qi, L.; Shi, L. Modeling of the height–diameter relationship using an allometric equation model: A case study of stands of *Phyllostachys edulis*. *J. For. Res.* **2016**, *27*, 339–347, doi:10.1007/s11676-015-0145-6.
73. Urbazaev, M.; Thiel, C.; Cremer, F.; Dubayah, R.; Migliavacca, M.; Reichstein, M.; Schmullius, C. Estimation of forest aboveground biomass and uncertainties by integration of field measurements, airborne LiDAR, and SAR and optical satellite data in Mexico. *Carbon Balance Manag.* **2018**, *13*, 5.
74. Wallace, L.; Lucieer, A.; Malenovsky, Z.; Turner, D.; Vopěnka, P. Assessment of Forest Structure Using Two UAV Techniques: A Comparison of Airborne Laser Scanning and Structure from Motion (SfM) Point Clouds. *Forests* **2016**, *7*, 62.
75. Burns, J.H.R.; Delparte, D. Comparison of commercial structure-from-motion photogrammetry software used for underwater three-dimensional modeling of coral reef environments. *Int. Arch. Photogramm. Remote Sens.* **2017**, *XLII-2/W3*, 127–131, doi:10.5194/isprs-archives-XLII-2-W3-127-2017.
76. Jiang, S.; Jiang, W. Efficient SfM for Oblique UAV Images: From Match Pair Selection to Geometrical Verification. *Remote Sens.* **2018**, *10*, 1246.
77. Karpina, M.; Jarzabek-Rychard, M.; Tymków, P.; Borkowski, A. UAV-Based Automatic Tree Growth Measurement for Biomass Estimation. *Journal: ISPRS Int. Arch. Photogramm. Remote Sens. Spat. Inf. Sci.* **2016**, *XLI-B8*, 685–688.
78. McGaughey, R.J. *FUSION/LDV: Software for LIDAR Data Analysis and Visualization; version 3.70*; United States Department of Agriculture, Forest Service: Washington, DC, USA, 2018.
79. Gianico, V.; Laforteza, R.; Jhon, R.; Sanesi, G.; Pesola, L.; Chen, J. Estimating Stand Volume and Above-Ground Biomass of Urban Forest Using LiDAR. *Remote Sens.* **2016**, *8*, 339, doi:10.3390/rs8040339.
80. Shiota, H.; Tanaka, K.; Nagashima, K. LiDAR Data Analysis with Fusion/LDV for Individual Tree. *J. Biodivers. Manag. For.* **2017**, *2017*, 6.
81. Homeier, J.; Werner, F.A.; Gawlik, J.; Peters, T.; Diertl, K.H.J.; Richter, M. Plant Diversity and its Relevance for the Provision of Ecosystem Services. In *Ecosystem Services, Biodiversity and Environmental Change in a Tropical Mountain Ecosystem of South Ecuador*, 1st ed.; Bendix, J., Beck, E., Bräuning, A., Makeschin, F., Mosandl, R., Scheu, S., Wilcke, W., Eds.; Springer: Berlin, Germany, 2013; Volume 221, pp. 100–118, ISBN 978-3-642-38136-2.
82. Zhao, P.; Lu, D.; Wang, G.; Wu, C.; Huang, Y.; Yu, S. Examining spectral reflectance saturation in Landsat imagery and corresponding solutions to improve forest aboveground biomass estimation. *Remote Sens.* **2016**, *8*, 469.
83. Hillier, A. *Working with ArcView 10*; University of Pennsylvania: Pennsylvania, PA, USA, 2011.

84. Ollado Latorre, J.; Navarro Jover, J.M. *ArcGIS 10: Prácticas Paso a Paso*; Universitat Politècnica: València, Spain, 2013.
85. Fensholt, R.; Rasmussen, K.; Nielsen, T.T.; Mbow, C. Evaluation of earth observation based long term vegetation trends – Intercomparing NDVI time series trend analysis consistency of Sahel from AVHRR GIMMS, Terra MODIS and SPOT VGT data. *Remote Sens. Environ.* **2009**, *113*, 1886–1898. doi:10.1016/j.rse.2009.04.004.
86. Chuvieco, E. *Teledetección Ambiental: La Observación de la Tierra desde el Espacio*, 3rd ed.; Editorial Ariel: Barcelona, Spain, 2010.
87. Feng, Y.; Lu, D.; Chen, Q.; Keller, M.; Moran, E.; Nara dos-Santos, M.; Bolfe, E.L.; Batistella, M. Examining effective use of data sources and modeling algorithms for improving biomass estimation in a moist tropical forest of the Brazilian Amazon. *Int. J. Digit. Earth* **2017**, doi:10.1080/17538947.2017.1301581.
88. Cabrera, O.; Fries, A.; Hildebrandt, P.; Günter, S.; Mosandl, R. Early Growth Response of Nine Timber Species to Release in a Tropical Mountain Forest of Southern Ecuador. *Forests* **2019**, *10*, 254.
89. Weier, J.; Herring, D. Measuring Vegetation (NDVI & EVI). 2000. Available online: <https://earthobservatory.nasa.gov/features/MeasuringVegetation> (accessed on 20 October 2018).
90. RStudio. Available online: https://www.r-studio.com/downloads/Recovery_Manual.pdf (accessed on 25 October 2018).
91. Mlambo, R.; Woodhouse, I.H.; Gerard, F.; Anderson, K. Structure from Motion (SfM) Photogrammetry with Drone Data: A Low Cost Method for Monitoring Greenhouse Gas Emissions from Forests in Developing Countries. *Forests* **2017**, *8*, 68.
92. Nevalainen, O.; Honkavaara, E.; Tuominen, S.; Viljanen, N.; Hakala, T.; Yu, X.; Hyypä, J.; Saari, H.; Pölonen, I.; Imai, N.N.; et al. Individual Tree Detection and Classification with UAV-Based Photogrammetric Point Clouds and Hyperspectral Imaging. *Remote Sens.* **2017**, *9*, 185.
93. Getzin, S.; Nuske, R.S.; Wiegand, K. Using Unmanned Aerial Vehicles (UAV) to Quantify Spatial Gap Patterns in Forests. *Remote Sens.* **2014**, *6*, 6988–7004.
94. Hsieh, Y.C.; Chan, Y.C.; Hu, J.C. Digital Elevation Model Differencing and Error Estimation from Multiple Sources: A Case Study from the Meiyuan Shan Landslide in Taiwan. *Remote Sens.* **2016**, *8*, 199.
95. Leuschner, C.; Zach, A.; Moser, G.; Homeier, J.; Graefe, S.; Hertel, D.; Wittich, B.; Soethe, N.; Iost, S.; Röderstein, M.; et al. The Carbon Balance of Tropical Mountain Forests Along an Altitudinal Transect. In *Ecosystem Services, Biodiversity and Environmental Change in a Tropical Mountain Ecosystem of South Ecuador*, 1st ed.; Bendix, J., Beck, E., Bräuning, A., Makeschin, F., Mosandl, R., Scheu, S., Wilcke,

- W., Eds.; Springer: Berlin, Germany, 2013; Volume 221, pp. 117–139, ISBN 978-3-642-38136-2.
96. Homeier, J.; Breckle, S.-W.; Günter, S.; Rollenbeck, R.T.; Leuschner, C. Tree Diversity, Forest Structure and Productivity along Altitudinal and Topographical Gradients in a Species-Rich Ecuadorian Montane Rain Forest. *Biotropica* **2010**, *42*, 140–148.
 97. Leuschner, C.; Moser, G. Carbon Allocation and productivity in tropical mountain forest. In *The Tropical Mountain Forest. Patterns and Process in a Biodiversity Hotspot*; Biodiversity and Ecology Series; Gradstein, S.R., Homeier, J., Gansert, D., Eds.; Universitätsverlag Göttingen: Göttingen, Germany, 2008; Volume 2, pp. 109–128.
 98. Dislich, C.; Günter, S.; Homeier, J.; Schröder, B.; Huth, A. Simulating forest dynamics of a tropical montane forest in South Ecuador. *Erdkunde* **2009**, *63*, 347–364.
 99. Gu, Y.; Wylie, B.K.; Howard, D.M.; Phuyal, K.P.; Ji, L. NDVI saturation adjustment: A new approach for improving cropland performance estimates in the Greater Platte River Basin, USA. *Ecol. Indic.* **2013**, *30*, 1–6, doi:10.1016/j.ecolind.2013.01.041.
 100. Bendig, J.; Bolten, A.; Bennertz, S.; Broscheit, J.; Eichfuss, S.; Bareth, G. Estimating Biomass of Barley Using Crop Surface Models (CSMs) Derived from UAV-Based RGB Imaging. *Remote Sens.* **2014**, *6*, 10395–10412.
 101. Teobaldelli, M.; Cona, F.; Saulino, L.; Migliozzi, A.; D’Urso, G.; Langella, G.; Manna, P.; Saracino, A. Detection of diversity and stand parameters in Mediterranean forests using leaf-off discrete return LiDAR data. *Remote Sens. Environ.* **2017**, *192*, 126–138, doi:10.1016/j.rse.2017.02.008.
 102. Fritz, A.; Kattenborn, T.; Koch, B. Uav-Based Photogrammetric Point Clouds—Tree STEM Mapping in Open Stands in Comparison to Terrestrial Laser Scanner Point Clouds. *Isprs - Int. Arch. Photogramm. Remote Sens. Spat. Inf. Sci.* **2013**, *XL-1/W2*, 141–146.
 103. Li, W.; Niu, Z.; Chen, H.; Li, D.; Wu, M.; Zhao, W. Remote estimation of canopy height and aboveground biomass of maize using high-resolution stereo images from a low-cost unmanned aerial vehicle system. *Ecol. Indic.* **2016**, *67*, 637–648, doi:10.1016/j.ecolind.2016.03.036.

5 Summary, Conclusions and Outlook

5.1 Summary and Conclusions

The anthropogenic activities during the last decades has provoked dramatic changes upon landscapes, especially within fragile ecosystems, which have suffered degradation up to the point of collapse (IPCC, 2013). These alterations are principally caused by extensive anthropogenic GHG emissions, which have resulted in general global warming and changes to other natural systems related to climate conditions (IPCC, 2018 and 2019). When considering total GHG emissions, 10% - 20% are caused by deforestation and other land use-changes (Gilbert, 2012; Smith et al., 2014), which is a considerable fraction relative to total global warming.

The high deforestation rates, especially in tropical countries, do not only increase global GHG emission and degrade natural ecosystems (Aguilar et al., 2012), but also affect the ecosystem services, which are essential for the local and regional population (Breuer et al., 2013). In order to mitigate the expected impacts on these ecosystems, conservation and reforestation areas must be determined, because forests store large amounts of C (Clark et al., 2011; Saatchi et al., 2011; Häger and Schendenmann, 2016). Furthermore, increased global forest cover (reforestation) serve as a carbon sequestration and storage strategy, because additional CO₂ is absorbed from the atmosphere and stored in the vegetation, especially in trunks and branches (Cuni-Sanchez et al., 2017).

However, to realize mitigations strategies, such as the identification of conservation and reforestation areas, forest inventories at country and catchment level are necessary. Furthermore, AGB stock of the forest ecosystems must be calculated, to estimate potential GHG emissions in the future and to account for carbon sequestration and storage of reforested areas. Therefore, remote sensing techniques are practical because they allow for the continuous monitoring of larger areas as well as for the specific parts of an ecosystem (Moraes et al., 2013; Galidaki et al., 2017; Wallis et al., 2019). Especially advantageous are these systems in tropical mountain regions due to the difficulties in access, which impedes larger field campaigns (Ferraz et al., 2016). By means of the remote sensed data, changes in forest cover, AGB and C stocks can be determined, as well as the state of the ecosystem (vegetation indexes) and areas for conservation/ reforestation identified (Eastman et al., 2013; Wang et al., 2014).

The aim of the present research was to provide an operational surveillance system, based on remote sensing technologies, to quantify forested cover and AGB stocks at different spatial scales. At country scale, the study analyzed the forest cover changes in Ecuador from 1986 to 2008 by means of historical information from the NOAA-AVHRR sensor; whereas AGB and C stocks were estimated at catchment scale by means of high-resolution LiDAR imagery. However, due to the high costs of LiDAR surveys, UAV data were tested to provide a tool for a continuous forest monitoring, especially for the most vulnerable parts.

With respect to the prepared hypotheses in Chapter 1, it can be concluded:

H1 In order to determine forest cover and deforestation rates at country level the historical satellite images from the NOAA-AVHRR sensor were found to be suitable, in light of their low spatial resolution (1km x 1km). Due to the temporally high image resolution, nearly cloud free annual composites could be generated, despite the high annual cloud frequency observed over Ecuador (up to 90%; Bendix et al., 2004 and 2006), and the forest cover determined using the vegetation index NDVI. The multi-temporal analysis indicated that the forest cover in Ecuador was continuously reduced over the last decades, especially at the coast and the Andean highlands, due to enhanced population pressure (Mosandl et al., 2008). However, the highest forest reduction was determined to be for the eastern cordillera of the Andes and the Amazon Basin, because of the government supported oil and mining industry, besides the illegal timber extraction taking place near the larger river systems (Bonan, 2008; Ochoa et al., 2015).

For the study period a total reduction of areas covered by forest from 48.1% in 1986 to 36.8% in 2008 could be stated, which is confirmed by other investigations (Cabarle et al., 1989, year 1986; MAE, 2011, year 2001; FAO, 2010, year 2008). Deforestation rates in Ecuador increased during the two decades analyzed from -0.9% (period 1986 – 2001) to -1.9% (period 2001 – 2008). Similar values were also reported by FAO (2010) and Tapia et al. (2015), which underline the utility of the applied method.

In summary, by means of annual composites, generated from temporally high but spatially low-resolution satellite images, the total forest cover at country scale can be determined and deforestation rates calculated, as well as the most

vulnerable parts detected. This information is crucial for decision makers for the planning and implementation of conservation or reforestation strategies (MAE, 2014).

H 2 The LiDAR data, specifically the 3D point clouds, permitted the generation of a high-resolution DTM and DSM (0.25m x 0.25m) of the San Francisco catchment, from which a CHM could be deviated. By means of the CHM and the Canopy Maxima tool of the software FUSION (McGaughey, 2018), the dominant trees within the whole watershed could be detected and their individual H determined. Combining the DTM and individual H with the topographic (TPI) and morphometric (MPI) index, the forest structure of this TMF could be depicted, particularly ravine and ridge forest parts (Werner and Homeier, 2015). The complex forest structure is mainly caused by the degree of topographic protection of the site and the climate conditions, which change considerably with altitude (Dislich and Huth, 2012; Homeier et al., 2013; Fries et al., 2014), for which reason bigger trees are generally located in depressions and smaller ones at the ridges or higher elevations (Elfin Forest). Furthermore, the individual H in combination with auxiliary data from field measurements (DBH and mean WD) allowed the calculation of AGB at tree level, applying the allometric equations for tropical wet forests from Chave et al. (2005). By accumulating the individual tree AGB within a hectare (ha), the AGB values of different forest parts could be estimated and the C stocks deduced.

The comparison of the results with field plot measurements in the same area indicated very good correlations ($R^2 > 0.9$), especially for H and DBH (Homeier et al., 2010; Leuschner et al., 2013; Paulick et al., 2017), whereas AGB values occasionally varied (Dislich et al., 2009; Werner and Homeier, 2015). This was due to field plot sizes (20m x 20m) and their distribution, which generally cannot depict the real forest structure in natural forest stands. Therefore, AGB calculations based on field plot measurements often under- or overestimate real AGB amounts (Saatchi et al., 2011; Mauya et al., 2015). The implementation of larger field plots to capture the landscape variability are normally too expensive for developing counties, besides the complexity in tropical high mountain terrain to detect the fast-changing forest structure, due to the difficulties in access and the complex relation between forest structure, topography and climate conditions

(Richter and Moreira-Muñoz, 2005; Kane et al., 2015; Ferraz et al., 2016). Therefore, only LiDAR data can accurately estimate for AGB and C stock in tropical high mountains at catchment scale, although only dominant/codominant trees can be detected, because they represent 70% to 90% of the total AGB of a forest stand (Kotowska et al., 2015; Bastin et al., 2015; Zhang et al., 2017). By means of the detailed information derived from LiDAR data the possible future GHG emissions (deforestation) and the potential of reforested areas for carbon sequestration and storage can be calculated, which support conservation and reforestation programs, such as the REDD+ initiative in Ecuador (MAE, 2015).

H3 Considering the high costs of LiDAR surveys (Brodu and Lague, 2012; Purnamasayangasukasih et al., 2016; Wallis et al., 2019) UAVs showed their potential for continuous forest monitoring of the most vulnerable parts within an ecosystem. UAVs can transport active or passive sensors, which permits the detection of the vegetation cover and the calculation of different vegetation indexes, as well as the estimation of AGB stocks (Swinfield et al., 2019). Besides their portability and flexibility, these platforms are cost-effective, for which reason FAO and other forest monitoring programs (e.g. REDD+), use this technology to detect and quantify areas recently deforested by anthropogenic activities (Berie and Burud, 2018).

However, in dense natural forest stands only RGB data in combination with photogrammetric techniques (SfM; Burns et al., 2017) showed accurate results for AGB estimation, if an auxiliary high-resolution DTM is also available (e.g. from LiDAR data). As the investigation showed, the detection of the terrain by means of RGB imagery is complicated, because this passive sensor cannot penetrate dense canopies (RMSE = 8.95m). The RGB data can detect the vegetation surface, which is why DSM model generation was accurate (RMSE = 3.05m). Therefore, to avoid errors in the final AGB estimation an auxiliary DTM should be used (Karpina et al., 2016). This is confirmed by the study results, which indicated a good correlation between LiDAR-AGB and RGB-AGB ($R^2 = 0.85$), and a similar mean AGB-value of $\sim 148 \text{ Mg ha}^{-1}$ for the study area. Furthermore, forest structure could be detected, because the generated 3D point cloud from the RGB data permitted the detection of individual trees. By means of this information it could be illustrated that bigger trees are generally located

in depressions, whereas smaller trees at the ridges (Werner and Homeier, 2015; Cabrera et al., 2019).

In contrast the multispectral approach to calculate AGB stocks in a natural TMF was less suitable, due to the saturation effect of the multispectral bands over dense natural vegetation (Zhao et al., 2016). Therefore, AGB estimation by means of multispectral data resulted in high overestimations. Also, forest structure could not be detected due to the saturation effect of the sensor. However, the multispectral approach might be useful for crop AGB estimation, if crop height information is available, too, due to the more uniform ground cover and less steep slopes.

In summary, the the more accurate approach for continuous forest monitoring of smaller areas is the RGB approach, which provides reliable AGB values and also detects the forest structure

5.2 Outlook

Hopefully, the presented operational surveillance systems for continuous forest monitoring at different scales will be implemented in Ecuador. With it, the most vulnerable parts can be determined, and conservation/ restoration strategies implemented to reduce the high deforestation rates at country level and to mitigate future GHG emissions, as well as to guarantee water supply for the local and regional population (ecosystem services).

Future investigations should focus on C fluxes between atmosphere and the different ecosystems, to quantify their potential for carbon sequestration. Furthermore, the impacts caused by deforestation respective to local climate conditions and hydrological cycle should be studied, which can give deeper insights into provided ecosystem services and their underlying processes. This information is crucial for decision makers to implement adaptation strategies due to ongoing global changes.

5.3 References

- Aguiar APD, Ometto JP, Nobre C, Lapola DM, Almeida C, Vieira IC, Soares JV, Alvala R, Saatchi S, Valeriano D, Castilla-Rubio JC (2012): Modeling the spatial and temporal heterogeneity of deforestation-driven carbon emissions: the INPE-EM framework applied to the Brazilian Amazon. *Global Change Biology* **18**: 3346–3366.
- Bastin J-F, Barbier N, Réjou-Méchain M, Fayolle A, Gourlet-Fleury S, Maniatis D, de Haulleville T, Baya F, Beeckman H, Beina D, P. Couteron P, Chuyong G, Dauby G, Doucet J-L, Droissart V, Dufrêne M, Ewango C, Gillet JF, Gonmadje CH, Hart T, Kavali T, Kenfack D, Libalah M, Malhi Y, Makana J-R, Pélissier R, Ploton P, Serckx A, Sonké B, Stevart T, Thomas DW, De Cannière C, Bogaert J (2015): Seeing Central African forests through their largest trees. *Sci. Rep.* **5**: 13156.
- Bendix J, Rollenbeck R, Palacios E (2004): Cloud detection in the Tropics - a suitable tool for climate-ecological studies in the high mountains of Ecuador. In: *International Journal of Remote Sensing* **25**: 4521–4540.
- Bendix J, Rollenbeck R, Göttlicher D, Cermak J (2006): Cloud occurrence and cloud properties in Ecuador. *Inter-Research Climate Research* **30**: 133–147.
- Berie HT, Burud I (2018): Application of unmanned aerial vehicles in earth resources monitoring: focus on evaluating potentials for forest monitoring in Ethiopia, *European Journal of Remote Sensing*, **51**:1, 326-335.
- Bonan G.B (2008): Forests and climate change: Forcings, feedbacks, and the climate benefits of forests. *Science* **320**: 1444–1449.
- Breuer L, Windhorst D, Fries A, Wilcke W (2013): Supporting, regulation, and provisioning hydrological services. In: Bendix J, Beck E, Bräuning A, Makeschin F, Mosandl R, Scheu S, Wilcke, W. (eds.): *Ecosystem services, biodiversity and environmental change in a tropical mountain ecosystem of south Ecuador*. Berlin, Heidelberg: 107–116.
- Brodu N, Lague D (2012): 3D terrestrial lidar data classification of complex natural scenes using a multi-scale dimensionality criterion: Applications in geomorphology, *ISPRS Journal of Photogrammetry and Remote Sensing* **68**: 121-134.
- Burns JHR, Delparte D (2017): Comparison of commercial structure-from-motion photogrammetry software used for underwater three-dimensional modeling of coral reef environments, *Int. Arch. Photogramm. Remote Sens.* 2017. *Spatial Inf. Sci.*, XLII-2/W3: 127-131.

- Cabarle BJ, Crespi M, Dodson CH, Luzuriaga C, Rose D, Shores JN (1989): An assessment of biological diversity and tropical forests for Ecuador. USAID, Quito.
- Cabrera O, Fries A, Hildebrandt P, Günter S, Mosandl R (2019): Early Growth Response of Nine Timber Species to Release in a Tropical Mountain Forest of Southern Ecuador. *Forests* **10**: 254.
- Cuni-Sanchez A, Pfeifer M, Marchant R, Calders K, Sørensen CL, Pompeu PV, Lewis SL, Burgess ND (2017): New insights on above ground biomass and forest attributes in tropical montane forests. *For. Ecol. Manag.* **399**: 235–246.
- Chave J, Andalo C, Brown S, Cairns MA, Chambers JQ, Eamus D, Fölster H.; Fromard, F, Higuchi N, Kira T, Lescure JP, Nelson BW, Ogawa H, Puig H, Riéra B, Yamakura T (2005): Tree allometry and improved estimation of carbon stocks and balance in tropical forests. *Oecologia* **145**: 87–99.
- Clark ML, Roberts DA, Ewel JJ, Clark, DB (2011): Estimation of tropical rain forest aboveground biomass with small-footprint lidar and hyperspectral sensors. *Remote Sens. Environ* **115**: 2931–2942.
- Dislich C, Günter S, Homeier J, Schröder B, Huth A. (2009): Simulating forest dynamics of a tropical montane forest in South Ecuador. *Erdkunde* **63**: 347–364
- Dislich C, Huth A (2012): Modelling the impact of shallow landslides on forest structure in tropical montane forests. *Ecol. Model.* **239**: 40–53.
- Eastman JR, Sangermano F, Machado EA, Rogan J, Anyamba A (2013): Global trends in seasonality of Normalized Difference Vegetation Index (NDVI), 1982–2011. *Remote Sensing* **5**: 4799–4818.
- FAO (2010): (Food and Agriculture Organization of the United Nations) (2010b): Evaluación de los recursos forestales mundiales 2010 – Informe Nacional Ecuador. Roma. [<http://www.fao.org/3/a-az203s.pdf>; accessed: March 2016]
- Ferraz A, Saatchi S, Mallet C, Jacquemoud S, Goncalves G, Silva AA, Soares P, Tomé M, Pereira L (2016): Airbone Lidar Estimation of Aboveground Forest Biomass in the Absence of Field Inventory. *Remote Sens.* **8**: 653.
- Fries A, Rollenbeck R, Bayer F, Gonzalez V, Oñate-Valivieso F, Peters T, Bendix J (2014): Catchment precipitation processes in the San Francisco valley in southern Ecuador: Combined approach using high-resolution radar images and in situ observations. *Meteorol. Atmos. Phys.* **126**: 13–29.
- Galidaki G, Zianis D, Gitas I, Radoglou K, Karathanassi V, Tsakiri-Strati M, Woodhouse I, Mallinis G (2017): Vegetation biomass estimation with remote

- sensing: focus on forest and other wooded land over the Mediterranean ecosystem, *International Journal of Remote Sensing*, **38**(7): 1940-1966
- Gilbert N (2012): One third of our greenhouse gas emissions come from agriculture. *Nature News & Comment*. 11708.
- Häger A, Schwendenmann L (2016): Forest Carbon Sequestration and Global Change. In *The Paradigm of Forests and the Survival of the Fittest*; Molina-Murillo, S.A., Rojas, C., Eds.; CRC Press: Boca Raton, FL, USA; London, UK; New York, NY, USA: 39–86.
- Homeier J, Breckle S-W, Günter S, Rollenbeck RT, Leuschner C (2010): Tree Diversity, Forest Structure and Productivity along Altitudinal and Topographical Gradients in a Species-Rich Ecuadorian Montane Rain Forest. *Biotropica* **42**: 140–148.
- Homeier J, Werner FA, Gawlik J, Peters T, Diertl KHJ, Richter M (2013): Plant Diversity and its Relevance for the Provision of Ecosystem Services. In *Ecosystem Services, Biodiversity and Environmental Change in a Tropical Mountain Ecosystem of South Ecuador*, Ecological Studies; Bendix, J., Beck, E., Bräuning, A., Makeschin, F., Mosandl, R., Scheu, S., Wilcke, W., Eds.; Springer: Berlin, Germany, 2013; Volume **221**: 100–118.
- IPCC (2013): (Intergovernmental Panel on Climate Change) Working Group I Contribution to the IPCC fifth assessment report climate change 2013: The Physical Science Basics. IPCC, Stockholm.
- IPCC (2018): GRUPO INTERGUBERNAMENTAL DE EXPERTOS SOBRE EL CAMBIO CLIMÁTICO. Comunicado de prensa del IPCC. Gêneve, Suiza. [https://www.ipcc.ch/site/assets/uploads/2018/11/pr_181008_P48_spm_es.pdf; accessed July 2019]
- IPCC, 2019: Summary for Policymakers. In: IPCC Special Report on the Ocean and Cryosphere in a Changing Climate [H.O. Pörtner, D.C. Roberts, V. Masson-Delmotte, P. Zhai, M. Tignor, E. Poloczanska, K. Mintenbeck, M. Nicolai, A. Okem, J. Petzold, B. Rama, N. Weyer (eds.)]. In press.
- Kane V.R, Lutz JA, Cansler CA, Povak NA, Churchill DJ, Smith DF, Kane JT, North, P (2015): Water balance and topography predict fire and forest structure patterns. *For. Ecol. Manag.* **338**: 1–13.
- Karpina M, Jarzabek-Rychard M, Tymków P, Borkowski A (2016): UAV-Based Automatic Tree Growth Measurement for Biomass Estimation. *Journal: ISPRS Int. Arch. Photogramm. Remote Sens. Spat. Inf. Sci.* **2016(XLI-B8)**: 685–688.

- Kotowska MM, Leuschner C, Triadiati T, Meriem S, Hertel D (2015): Quantifying above- and belowground biomass carbon loss with forest conversion in tropical lowlands of Sumatra (Indonesia). *Glob. Chang. Biol.* **21**: 3620–3634.
- Leuschner C, Zach A, Moser G, Homeier J, Graefe S, Hertel D, Wittich B, Soethe N, Iost S, Röderstein M, Horna V, Wolf K (2013): The Carbon Balance of Tropical Mountain Forests Along an Altitudinal Transect. In: *Ecosystem Services, Biodiversity and Environmental Change in a Tropical Mountain Ecosystem of South Ecuador*, Ecological Studies; Bendix J, Beck E, Bräuning A, Makeschin F, Mosandl R, Scheu S, Wilcke W, Eds.; Springer: Berlin, Germany, **221**: 117–139.
- MAE (2011): (Ministerio del Ambiente | Ecuador) Estimación de la Tasa de Deforestación del Ecuador Continental. Quito. [<http://simce.ambiente.gob.ec/sites/default/files/documentos/geovanna/Estimaci%C3%B3n%20de%20la%20Tasa%20de%20Deforestaci%C3%B3n%20del%20Ecuador%20Continental.pdf>; accessed June 2015]
- MAE (2014): (Ministerio del Ambiente | Ecuador) - Plan nacional de Restauración Forestal 2014 – 2017. Quito. [<http://sociobosque.ambiente.gob.ec/files/images/articulos/archivos/amrPlanRF.pdf>; accessed June 2015]
- MAE (2015): (Ministerio del Ambiente | Ecuador) Cambio climático una estrategia transversal de desarrollo. [<http://www.ambiente.gob.ec/cambio-climatico-una-estrategia-transversal-de-desarrollo/>; accessed June 2015]
- Mauya EW, Hansen EH, Gobakken T, Bollandsas OM, Malimbwi RE, Naesset E (2015): Effects of field plot size on prediction accuracy of aboveground biomass in airborne laser scanning-assisted inventories in tropical rain forest of Tanzania. *Carbon Balance Manag.* **10**: 10.
- McGaughey RJ (2018): FUSION/LDV: Software for LIDAR Data Analysis and Visualization, version 3.70; United States Department of Agriculture, Forest Service: Washington, DC, USA.
- Moraes EC, Franchito S, Rao B (2013): Amazonian Deforestation: Impact of global warming on the energy balance and climate. *Journal of Applied Meteorology and Climatology* **52**: 521–530.
- Mosandl R, Günter S, Stimm B, Weber M (2008): Ecuador suffers the highest deforestation rate in South America. In: Beck E, Bendix J, Kottke I, Makeschin F, Mosandl R. (eds.): *Gradients in a tropical mountain ecosystem of Ecuador*. Ecological Studies **198**, Springer-Verlag, Berlin, Heidelberg, Germany: 37-40.

- Ochoa-Cueva P, Fries A, Montesinos P, Rodríguez-Díaz JA, Boll J (2015): Spatial Estimation of Soil Erosion Risk by Land-cover Change in the Andes of Southern Ecuador. *L. Degrad. Dev.* **26**: 565–573.
- Paulick S, Dislich C, Homeier J, Fischer R, Huth A (2017): The carbon fluxes in different successional stages: Modelling the dynamics of tropical montane forests in South Ecuador. *For. Ecosyst.* **4**: 5.
- Purnamasayangasukasih RP, Norizah K, Ismail AAM, Shamsudin I (2016): A review of uses of satellite imagery in monitoring mangrove forests. *IOP Conference Series: Earth and Environmental Science* **37**: 012034.
- Richter M, Moreira-Muñoz A (2005): Climatic heterogeneity and vegetation diversity in southern Ecuador investigated by phytoindication. *Rev. Peru. Boil.* **12**: 217–238.
- Saatchi SS, Harris NL, Brown S, Lefsky M, Mitchard ETA, Salas W, Zutta BR, Buermann W, Lewis SL, Hagen S, Petrova S, White L, Morel, A (2011): Benchmark map of forest carbon stocks in tropical regions across three continents. *Proceedings of the National Academy of Science of the United States of America* **108**: 9899–9904.
- Smith P, Clark H, Dong H, Elsiddig EA, Haberl H, Harper R, House J, Jafari M, et al. (2014). Chapter 11 - Agriculture, forestry and other land use (AFOLU). In: *Climate Change 2014: Mitigation of Climate Change*. IPCC Working Group III Contribution to AR5. Cambridge University Press
- Swinfield T, Lindsell JA, Williams JV, Harrison RD, Habibi A, Gemita E, Schönlieb CB, Coomes DA (2019): Accurate Measurement of Tropical Forest Canopy Heights and Aboveground Carbon Using Structure From Motion. *Remote Sens.* **11**: 928.
- Tapia-Armijos MF, Homeier J, Espinosa CI, Leuschner C, de la Cruz M (2015): Deforestation and forest fragmentation in South Ecuador since the 1970s – losing a hotspot of biodiversity. *PLOS ONE* **10**(9): e0133701.
- Wang L, Xiao P, Feng X, Li H, Zhang W, Lin J (2014): Effective compositing method to produce cloud-free AVHRR image. *IEEE Geoscience and Remote Sensing Letters* **11**: 328–332.
- Wallis, C.I.; Homeier, J.; Peña, J.; Brandl, R.; Farwig, N.; Bendix, J. (2019): Modeling tropical montane forest biomass, productivity and canopy traits with multispectral remote sensing data. *Remote Sens. Environ.* **225**: 77–92.
- Werner FA, Homeier, J (2015): Is tropical montane forest heterogeneity promoted by a resource-driven feedback cycle? Evidence from nutrient relations, herbivory and litter decomposition along a topographical gradient. *Funct. Ecol.* **29**: 430–440.

- Zhang Z, Cao L, She G (2017): Estimating forest structural parameters using canopy metrics derived from airborne LiDAR data in subtropical forests. *Remote Sens.* **9**: 940.
- Zhao P, Lu D, Wang G, Wu C, Huang Y, Yu S (2016): Examining spectral reflectance saturation in Landsat imagery and corresponding solutions to improve forest aboveground biomass estimation. *Remote Sens.* **8**: 469.

Abstract

Global forest cover has suffered a dramatic reduction during recent decades, especially in tropical regions, which is mainly due to human activities caused by enhanced population pressures. Nevertheless, forest ecosystems, especially tropical forests, play an important role in the carbon cycle functioning as carbon stocks and sinks, which is why conservation strategies are of utmost importance respective to ongoing global warming.

In South America the highest deforestation rates are observed in Ecuador, but an operational surveillance system for continuous forest monitoring, along with the determination of deforestation rates and the estimation of actual carbon stocks is still missing. Therefore, the present investigation provides a functional tool based on remote sensing data to monitor forest stands at local, regional and national scales. To evaluate forest cover and deforestation rates at country level satellite data was used, whereas LiDAR data was utilized to accurately estimate the Above Ground Biomass (AGB; carbon stocks) at catchment level. Furthermore, to provide a cost-effective tool for continuous forest monitoring of the most vulnerable parts, an Unmanned Aerial Vehicle (UAV) was deployed and equipped with various sensors (RGB and multispectral camera).

The results showed that in Ecuador total forest cover was reduced by about 24% during the last three decades. Moreover, deforestation rates have increased with the beginning of the new century, especially in the Andean Highland and the Amazon Basin, due to enhanced population pressures and the government supported oil and mining industries, besides illegal timber extractions. The AGB stock estimations at catchment level indicated that most of the carbon is stored in natural ecosystems (forest and páramo; AGB ~98%), whereas areas affected by anthropogenic land use changes (mostly pastureland) lost nearly all their storage capacities (AGB ~2%). Furthermore, the LiDAR data permitted the detection of the forest structure, and therefore the identification of the most vulnerable parts. To monitor these areas, it could be shown that UAVs are useful, particularly when equipped with an RGB camera (AGB correlation: $R^2 > 0.9$), because multispectral images suffer saturation of the spectral bands over dense natural forest stands, which results in high overestimations.

In summary, the developed operational surveillance systems respective to forest cover at different spatial scales can be implemented in Ecuador to promote conservation/ restoration strategies and to reduce the high deforestation rates. This may also mitigate future greenhouse gas emissions and guarantee functional ecosystem services for local and regional populations.

Zusammenfassung

Über die letzten Jahrzehnte hat der weltweite Waldbestand eine dramatische Reduzierung erfahren, besonders in der tropischen Zone, was hauptsächlich durch menschliche Eingriffe aufgrund des gestiegenen Bevölkerungswachstums hervorgerufen wurde. Nichtsdestotrotz nehmen Waldbestände, insbesondere tropische Wälder, eine besondere Rolle im Kohlenstoffkreislauf ein da sie Kohlenstoff aufnehmen und speichern, weshalb die Erhaltung der Bestände besonders wichtig ist hinsichtlich der fortschreitenden globalen Erwärmung.

Die höchsten Entwaldungsraten in Südamerika sind bestätigt für Ecuador, wo ein Überwachungssystem bezüglich des Waldbestands, Entwaldungsraten und der Kohlenstoffspeicherung immer noch fehlt. Diesbezüglich stellt die vorliegende Studie ein funktionales Werkzeug bereit, basierend auf Fernerkundungsdaten, um die Waldbestände auf lokaler, regionaler und nationaler Ebene zu überwachen. Der Waldbestand auf nationaler Ebene sowie die entsprechenden Entwaldungsraten wurden anhand von Satellitendaten bestimmt, wohingegen die oberirdische Kohlenstoffspeicherung (Above Ground Biomass, AGB) für komplette Einzugsgebiete anhand von LiDAR-Daten zuverlässig geschätzt wurde. Des Weiteren, um ein kostengünstiges Werkzeug für die Überwachung der am stärksten gefährdeten Bereiche bereitzustellen, wurde eine Drohne (Unmanned Aerial Vehicle, UAV) verwendet, die mit verschiedenen Sensoren ausgerüstet wurde (Kamera RGB und Multispektral).

Die Ergebnisse zeigten, dass in Ecuador die erhaltenen Waldbestände über die letzten drei Jahrzehnte um ungefähr 24% reduziert wurden. Zudem ist die Entwaldungsrate seit dem Beginn des neuen Jahrhunderts gestiegen, besonders im Andenhochland und im Amazonasbecken aufgrund des erhöhten Bevölkerungswachstums und der staatlich geförderten Erdöl- und Bergwerk-Industrie; eingeschlossen ist auch der illegale Holzeinschlag. Die Schätzung der Kohlenstoffspeicherung auf Einzugsgebietsebene ergab, dass der meiste Kohlenstoff in natürlichen Ökosystemen gespeichert wird (Wald und Páramo; AGB ~98%), wohingegen Bereiche die von menschlichen Nutzungsänderungen gekennzeichnet sind (mehrheitlich Weideland) fast ihre gesamte Speicherkapazität verloren haben (AGB ~2%). Zudem ermöglichte die LiDAR-Information die Erkennung der Waldstruktur, was gleichzeitig die Ermittlung der am stärksten gefährdeten Bereiche einschloss. Um diese Bereiche zu überwachen konnten Drohnen als zweckmäßiges Werkzeug definiert werden, besonders wenn sie mit einer RGB-Kamera ausgerüstet sind (AGB-Übereinstimmung: $R^2 > 0.9$), da Multispektral-Bilder über dichten natürlichen Waldbeständen eine Übersättigung der einzelnen Spektralbandfilter erfahren, was zu einer Überschätzung der wirklichen Werte führt.

Zusammenfassend ist zu sagen, dass das entwickelte Überwachungssystem des Waldbestands auf unterschiedlicher räumlicher Skala in Ecuador umgesetzt werden kann um damit Erhaltungs- / Restaurierungsstrategien zu fördern und die Entwaldungsrate zu reduzieren. Dies schließt die Reduzierung künftiger Emissionen von Treibhausgasen mit ein und gewährleistet auch die zweckmäßige Bereitstellung der Dienstleistungen der Ökosysteme für die lokale und regionale Bevölkerung.

Erklärung

Ich erkläre ehrenwörtlich, dass ich die dem Fachbereich Geographie der Philipps-Universität Marburg zur Promotionsprüfung eingereichte kumulative Dissertation mit dem Titel „***Vegetation Dynamics in Ecuador***“ unter Leitung von Prof. Dr. Jörg Bendix und Prof. Dr. Andreas Fries ohne sonstige Hilfe selbst durchgeführt und bei der Abfassung der Arbeit keine anderen als die in der Arbeit aufgeführten Hilfsmittel benutzt habe.

Die Dissertation wurde in der jetzigen oder einer ähnlichen Form noch bei keiner anderen Hochschule eingereicht und hat noch keinen sonstigen Prüfungszwecken gedient.

Marburg a. d. Lahn, den 10.01.2020



Víctor Hugo González Jaramillo

CURRICULUM VITAE

PERSONAL INFORMATION

Name: Víctor Hugo González Jaramillo
Date and place of birth: 26.09.1980 in Guayaquil
Marital status: Married, 4 kids
Nationality: Ecuadorian
Address: Sangay y Santa Marianita de Jesús, Loja

FAMILY

Parents Maruja Elvia Jaramillo Encalada, Teacher
Ruperto Antonio González Godoy, Lawyer

PROFESSIONAL EXPERIENCE

2005 – 2020 Lecturer and Researcher, Technical University of Loja (Universidad Técnica Particular de Loja, UTPL)

TERTIARY EDUCATION

1998 – 2005 Universidad Técnica Particular de Loja, Ingeniería en sistemas informáticos y computación. Título de investigación: Desarrollo de un Sitio Web de administración y visualización de proyectos SIG

SCHOOL EDUCATION

1994 – 1998 Unidad Educativa Experimental Bernardo Valdivieso - Loja, Bachiller en Físico Matemáticas
1992 – 1994 Colegio Eloy Alfaro – Cariamanga
1988 – 1992 Escuela San José - Cariamanga
1986 – 1988 Escuela Cuarto Centenario - Loja

OTHER PUBLICATIONS

Fries, A.; Rollenbeck, R.; Bayer, F.; **Gonzalez, V.**; Onate-Valivieso, F.; Peters, T.; Bendix, J. (2014) Catchment precipitation processes in the San Francisco valley in southern Ecuador: combined approach using high-resolution radar images and in situ observations. *Meteorol. Atmos. Phys.* 126:13–29. doi:10.1007/s00703-014-0335-3

Bendix, J.; Fries, A.; Zarate, J.; Trachte, K.; Rollenbeck, R.; Pucha-Cofrep, F.; Paladines, R.; Palacios, I.; Orellana, J.; Onate-Valdivieso, F.; Naranjo, C.; Mendoza, L.; Mejia, D.; Gualpa, M.; Gordillo, F.; **Gonzalez-Jaramillo, V.**; Dobbermann, M.; Celleri, R.; Carrillo, C.; Araque, A., Achilles, S. (2017). Bull. Am. Meteorol. Soc., RadarNet-Sur first weather radar network in Tropical high mountains. doi:10.1175/BAMS-D-15-00178.1

Oñate-Valdivieso, F.; Fries, A.; Mendoza, K.; **Gonzalez-Jaramillo, V.**; Pucha-Cofrep, F.; Rollenbeck, R.; Bendix, J. (2018). Temporal and spatial analysis of precipitation patterns in an Andean region of southern Ecuador using LAWR weather radar. *Meteorol. Atmos. Phys.* 130: 473. <https://doi.org/10.1007/s00703-017-0535-8>